

**Multivariate Analysis of Synthesis Process  
and Material Structure for Carbons  
containing Nitrogen using Solution Plasma**

**Niu Jiangqi**

**Multivariate Analysis of Synthesis Process  
and Material Structure for Carbons  
containing Nitrogen using Solution Plasma**

A Doctoral Dissertation by

**Niu Jiangqi**

**2023**

**Graduate School of Engineering,  
Department of Chemical Systems Engineering,  
Nagoya University**

---

# *Table of Content*

<b>Abstract</b> .....	1
-----------------------	---

## **Chapter 1: General Introduction**

1.1 Social requirement.....	5
1.2 Carbon materials.....	5
1.3 Solution plasma process.....	8
1.4 Object and outline of the thesis.....	15
References.....	19

## **Chapter 2: Excited Chemical Species Produced by Solution Plasma in Cyclic Organic Compounds and the Structural Correlation with the Raw Molecules**

2.1 Introduction.....	26
2.2 Experimental Procedures.....	28
2.3 Results and Discussion.....	31
2.4 Conclusion.....	43
References.....	43

## **Chapter 3: Chemical Intermediates Produced by Solution Plasma in Cyclic Organic Compounds and the Structural Correlation with the Raw Molecules**

3.1 Introduction.....	50
3.2 Experimental procedures.....	52
3.3 Results and Discussion.....	53
3.4 Conclusion.....	67
References.....	68

---

**Chapter 4: Plasma Potential Induced by Solution Plasma in Cyclic Organic Compounds and the Structural Correlation with the Raw Molecules**

4.1 Introduction.....	72
4.2 Experimental Procedures.....	75
4.3 Results and Discussion.....	77
4.4 Conclusion.....	90
References.....	90

**Chapter 5: Graphitic N-doped Graphene via Solution Plasma with a Single Dielectric Barrier**

5.1 Introduction.....	95
5.2 Experimental Procedures.....	97
5.3 Results and Discussion.....	99
5.4 Conclusion.....	116
References.....	117

**Chapter 6: Summary.....125**

**Achievement.....128**

---

## *Acknowledgments*

It is my genuine pleasure to express my deep gratitude to Professor Nagahiro Saito (Department of Chemical Systems Engineering, Graduate School of Engineering, Nagoya University) for his professional guidance and encouragement for this research. It will be my lifelong privilege to conduct research activities at Saito Laboratory. I am sure these experiences will be a great treasure in my future life.

I would like to extend my heartfelt thanks to my respected Professor Maria Antoaneta Bratescu (Retired, Department of Chemical Systems Engineering, Graduate School of Engineering, Nagoya University) for her excellent advice when I consulted her about my research. Moreover, I am also thankful to Associate Professor Yasuyuki Sawada (Department of Chemical Systems Engineering, Graduate School of Engineering, Nagoya University) for his efforts in managing the laboratory so that I could conduct my research here without any worries.

I am incredibly grateful to acknowledge the support and inspiration that I received from Assistant Professor Chayanaphat Chokradjaroen (Department of Chemical Systems Engineering, Graduate School of Engineering, Nagoya University), who gave me detailed guidance in many aspects, including how to conduct my research, write papers, present them at conferences, and many other detailed instructions. She is an excellent example to follow in scientific research and thinking.

I sincerely appreciate Eriko Kondo, the laboratory secretary, for her continuous support throughout my study. It was a great comfort and relief that she was willing to provide management activities while I completed my Ph.D. I value the assistance of Angeline Galang Umbina for her language proficiency. Furthermore, I sincerely appreciate the constant support of all the members of Saito Laboratory for their advice and cooperation from the time of my Ph.D. career.

---

---

My completion of this could not have been accomplished without the support of the China Scholarship Council (CSC) for financial support for my study in Japan through No. 201909110064.

Finally, I am deeply thankful to my family for their love, care, and sacrifices in educating and preparing me for my future.

---

---

# *Abstract*

Nitrogen doped (N-doped) carbon materials have been widely studied and present their potential use for various energy conversion applications. For the synthesis of N-doped carbon materials, conventional methods with high temperatures, such as thermal annealing and solvothermal methods, are mainly used. The high temperature can significantly promote the reaction by providing large energy to starting organic molecules, leading to the activation of starting organic molecules to undergo the reaction. Nevertheless, the high-temperature process usually causes the evaporation of nitrogen, a lightweight element, resulting in a small amount of nitrogen contained in the carbons. To overcome this problem, low-temperature processes are necessary. However, for the conventional methods, when the temperature is lowered, the reaction becomes much slower because only a small number of activated species can go through the reaction. Recently, solution plasma (SP), a non-equilibrium plasma, have developed and drawn much attention due to its ability to form numerous activated species and promote reactions at low temperature. SP was found to be an effective low-temperature process for the synthesis of N-doped carbons with relatively high doping concentrations. Since SP involves a multidisciplinary of physics, chemistry, and materials science, there have been several unsolved questions. The intensive investigation of SP should lead to a solution and clear understanding, which can bring advantages to further improvement. In this research work, a correlation between the process parameters of SP and the structural parameters of carbon products was discovered by using multivariate analysis. Moreover, the improved SP method was also proposed to synthesize the N-doped carbon with significantly high doping concentration and a well-structured planar framework.

**In Chapter 1**, the general introduction, including the information on SP and their applications in material synthesis, mainly carbon synthesis, was first provided. Moreover, the information on critical process parameters (*i.e.*, active chemical species from plasma phase,

---

intermediate species from liquid phase, and electric potential from plasma phase to liquid phase) and the structural parameters of carbons (*i.e.*, N content, defect index, and crystallinity) was explained. Finally, the objective and concept design of this research work was described. The selection of fifty-three organic molecules with  $\sigma$ - and  $\pi$ -bonded five- and six-member ring and containing nitrogen components was proposed as the investigated raw materials.

**In Chapter 2**, the correlation between patterns of optical emission spectroscopy (OES) with different dominations of activated chemical species in SP reaction field and structural parameters of carbon products was discovered. Four patterns with  $H^*$ ,  $C_2^*$ ,  $CN^*$ , and  $C_2^*/CN^*$  dominations were categorized.  $H^*$  and  $C_2^*$  were important species for the formation of amorphous carbon and graphite, respectively. Nevertheless,  $CN^*$  was important species for the synthesis of N-doped carbon with high doping concentration.

**In Chapter 3**, the correlation between the intermediate species in SP reaction field and the structural parameters of carbon products was discovered. The  $\sigma$ -bonded organic molecules, including five- or six-member ring molecules, dominantly formed intermediates with linear structures. Both  $\pi$ -bonded five- and six-member ring organic molecules mainly maintained ring structure during SP. The linear intermediates were found to produce carbon with lower nitrogen content but higher crystallinity. Oppositely, the intermediates with ring structure could produce carbon with relatively higher nitrogen content. Accordingly, the synthesis pathway of N-doped carbons could be altered depending on the organic molecules as the raw material.

**In Chapter 4**, the correlation between the electric potential in SP reaction field and the structural parameters of carbon products was investigated. The electric potential at different phases (*i.e.*, plasma, interface, and gas phases) was evaluated by an electrostatic probe technique. As a result, the reaction field with the high electric potential in the plasma phase could result in the formation of graphite-like carbon. However, there was an unclear correlation between the electric potential and nitrogen content in the carbon products.



---

**In Chapter 5**, according to the multivariate analysis of critical process and structural parameters from the above chapters, the modified SP system was proposed and successfully produced graphitic N-doped graphene with a high nitrogen content of 18.79 at.%. The proposed system could reduce the excessive current, resulting in stabilizing the glow plasma and maintaining the overall temperature to be at room temperature. It successfully preserved nitrogen atoms in the organic molecules from evaporation during the synthesis process and promoted the formation of a graphitic carbon framework.

**In Chapter 6**, the correlations of all critical processes and structural parameters in the synthesis of N-doped carbons using SP by multivariate analysis were concluded. The multi-correlation could reveal the connections between the chemical structure of raw materials, activated chemical species, intermediates, electric potentials during SP, and chemical and physical structures of the obtained carbon products. The systematic multi-correlation proved that it could provide direction for designing and modifying SP to achieve the synthesis of graphitic N-doped graphene with significantly high nitrogen content. Moreover, other possible directions for carbon-based material synthesis by SP were proposed in this thesis to guide process designs for chemists, materials scientists, and engineers who are dedicated to the research of carbon-based materials.

# *Chapter 1*

## *General Introduction*

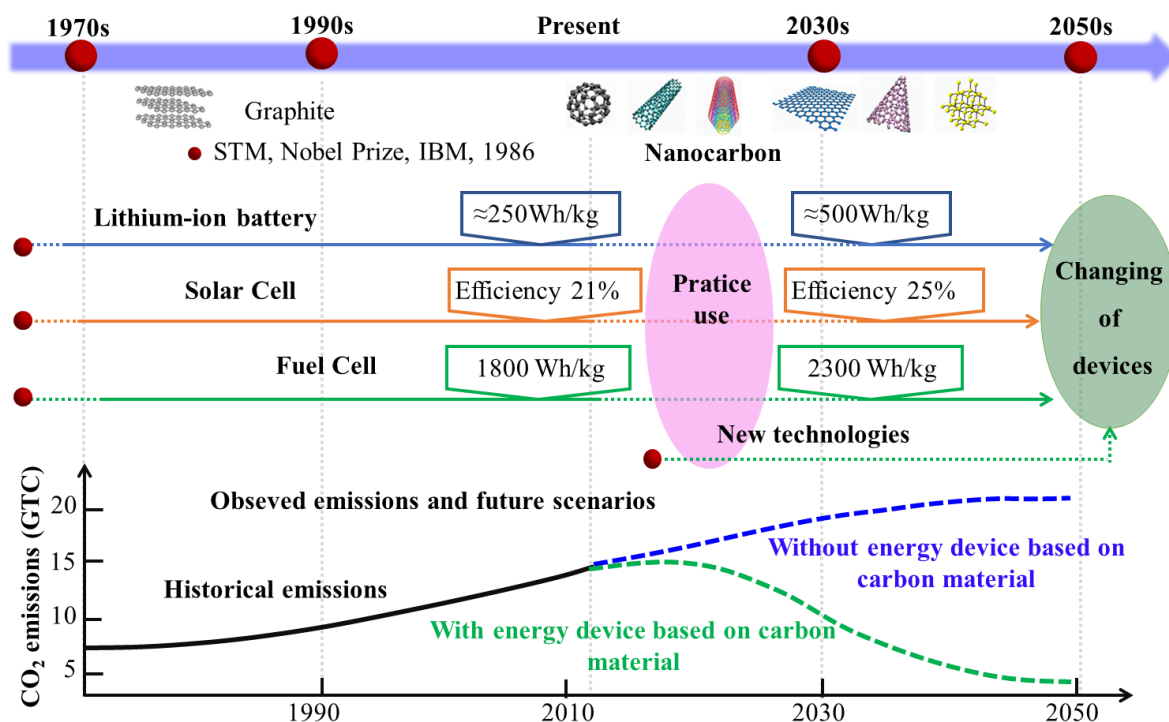
# ***Chapter 1 - General Introduction***

## **1.1 Social requirement**

Global warming has become a serious issue in our society [1,2]. The main sources of pollution are carbon dioxide, methane, and chlorofluorocarbons which account for 56%, 18%, and 13% of total exhaust gases, respectively. More than 50% of carbon dioxide, the main component of greenhouse gas emissions, comes from electricity production, industries, and transportation which mainly relate to energy applications and are necessary for humans [3-5]. Recently, the sustainable development goals (SDGs) were announced and have drawn the attention of many countries aiming to obtain a sustainable society. Several countries, including Japan, are motivated to take action for a carbon zeroization society by increasing energy efficiency, utilizing renewable energy, and developing new technologies for energy devices [6-9].

## **1.2 Carbon materials**

Since 1970, graphite has been developed and used in energy devices (*e.g.*, lithium-ion batteries) [10,11]. Taking advantage of the scanning tunneling microscope (STM) developed by Gerd Binnig and Heinrich Rohrer (Nobel Prize Winner in 1986), the era of nano-scaled materials was started [12], as shown in **Figure 1.1**. Thus, several nanocarbon materials have been proposed, such as graphene, carbon nanotube, fullerenes, etc. These nanocarbon materials have been applied to several energy devices, for example, lithium-ion batteries, solar cells, and fuel cells [13-15]. However, the development of the nanocarbon materials is still intensively conducted to accomplish new energy technologies that can prevent the carbon dioxide emission, leading to the sustainable society.

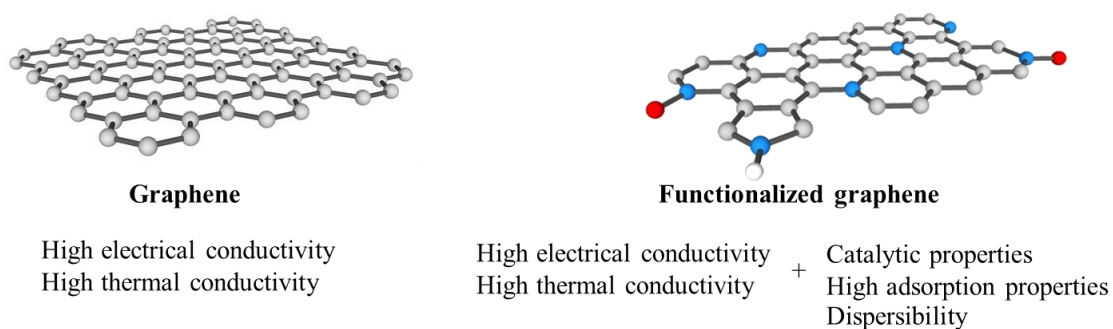


**Figure 1.1** The development process of energy devices based on carbon materials and the impact on carbon dioxide emissions in the future.

### 1.2.1 Nitrogen-doped graphene

Graphene is a two-dimensional planar structured nanomaterial with a hexagonal arrangement of carbon atoms with  $sp^2$  hybridization. Its excellent properties, such as good electrical and mechanical properties, have attracted much attention. Furthermore, heteroatom doping has been proposed to modulate the inherent chemical state and electronic structure of graphenes, such as the spin density of carbon atoms and the charge distribution on the surface [16-20]. The "activation region" on the surface of graphene, which provides reaction sites for catalytic reactions, can be significantly enhanced by adjusting the number of heteroatom dopants. However, the heteroatom doping of carbon materials has remained at a low level of investigation [21-25]. Compared with the carbon atom, the nitrogen atom has similar atomic scales, thus, doping nitrogen is theoretically possible and should be easy to be conducted. By doping nitrogen atoms, it is possible to further endow graphene with catalytic properties, high gas adsorption properties, and good dispersion based on its high electrical and thermal

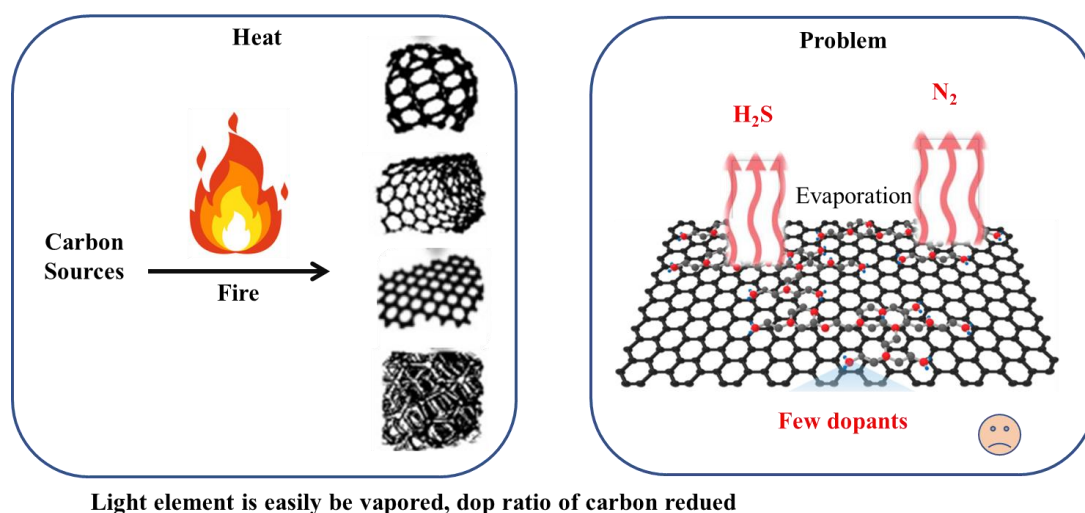
conductivity [26-28], as shown in **Figure 1.2**. Meanwhile, the surface energy and reactivity of carbon frameworks could be effectively improved for nitrogen-doped carbon with a low-defect planar structure. It is a promising tool for energy conversion applications [14,16,17,20,29-33].



**Figure 1.2** The properties of the functionalized graphene compared with graphene.

### 1.2.2 Synthesis of nitrogen-doped graphene

In the conventional thermal process, higher temperatures are unavoidably used to obtain morphologically diverse carbon products, which makes it easier for the light atoms represented by N atoms to undergo vaporization and evaporation processes [34], as shown in **Figure 1.3** and **Table 1.1**. Thus, it eventually results in a lower doping rate. This is a common problem faced in the field of nitrogen-doped graphene research at present.



**Figure 1.3** Schematic of difficulty doping heteroatom into carbon framework for energy application used in the conventional thermal process.

**Table 1.1** Current techniques for the synthesis of nitrogen doped graphene

Technique	Precursor	Energy	Time (min)	N (at%)	Ref.
CVD	Pyridine	1000 °C	20	2.63	[6]
	Chitosan	1000 °C	60	4.2	[7]
	N-doped C dots	1000 °C	30	9.2	[8]
Arc discharge	Graphene oxide and solid nitrogen	150 A	/	3.5	[9]
	CH <sub>4</sub> /N <sub>2</sub> /Ar	100 A	20	4.2	[10]
	H <sub>2</sub> /N <sub>2</sub> /Ar	200 A	20	4.6	[11]
Thermal annealing	Graphite/N <sub>2</sub> /O <sub>2</sub>	800 °C	120	12.9	[12]
	Graphite/poly	900 °C	30	3.3	[13]
Solvothermal	Ethylenediamine	140 °C	>60	11.63	[14]
Solution plasma by pin-to-pin	DMF		60	3.93	[15]
	2-cyanopyridine	Room temperature	30	1.16	[16]
	Acrylonitrile		20	8.58	[17]
	Aniline		6	1.24	[18]

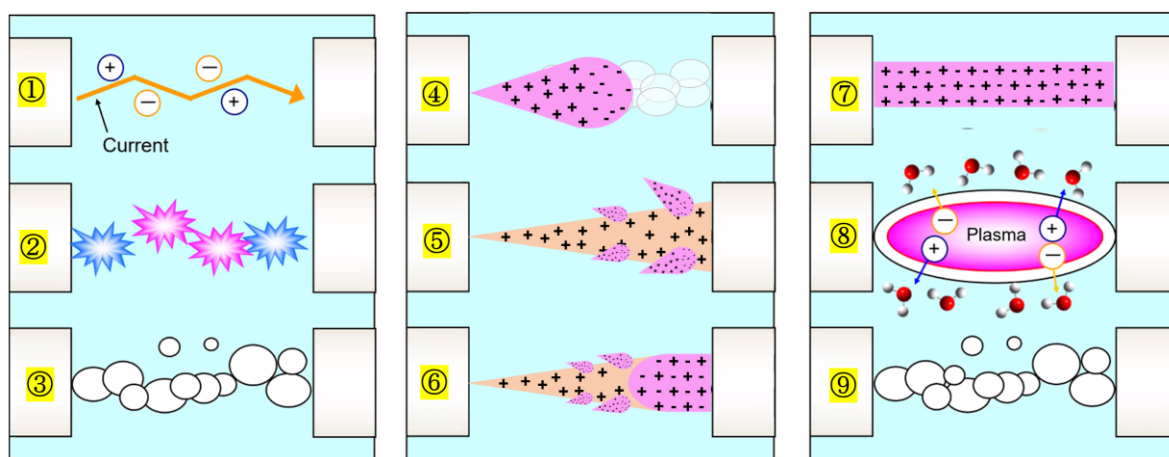
### 1.3 Solution plasma process

Solution plasma as a non-thermal equilibrium technique has recently gained much attention from research scholars. The formation process of solution plasma based on the pin-to-pin electrode geometry is shown in **Figure 1.4**.

Step 1, when the voltage is applied to the electrode, the breakdown of dielectric *i.e.*, the liquid, will occur, and it will generate the radicals and ions, including OH<sup>\*</sup>, H<sup>\*</sup>, OH<sup>-</sup>, H<sup>+</sup> and so on. Step 2-3, the recombination of radicals by “Cage Effect” with solvent molecules will follow and induce the gas production.

Step 4, when the applied voltage is up to the breakdown value, the initial electron avalanche will generate formed bubbles, and the seed electrons are coming from the metal electrode surface. Step 5, when the electron avalanche reaches the other side of the electrode, the electrons will quickly flow into the metal surface, and only the ions will be left. Numerous ions will cause distortion of the electric field, which further induces the photoionization process and form the secondary electron avalanche. Step 6, the electron provided by the secondary avalanche will be absorbed into the initial avalanche and generate negative or positive ions, called positive streamers.

Step 7, when the positive streamer develops to another electrode, the plasma channel is formed. Step 8, the deactivation of radicals and ions by collision with solvent molecules, called the trapping effect will occur, and the existence of charged particles at the gas-liquid interface will also show up with the voltage increase. Step 9, due to the power sources being pulsed, the discharge will instantly extinguish when the loss of energy support from power source. In this case, the density and energy of ions can be inhibited. It is also the basic reason solution plasma can work at a low-temperature state. When the next pulse is provided again, the bubbles will also be formed, as shown in step 3.



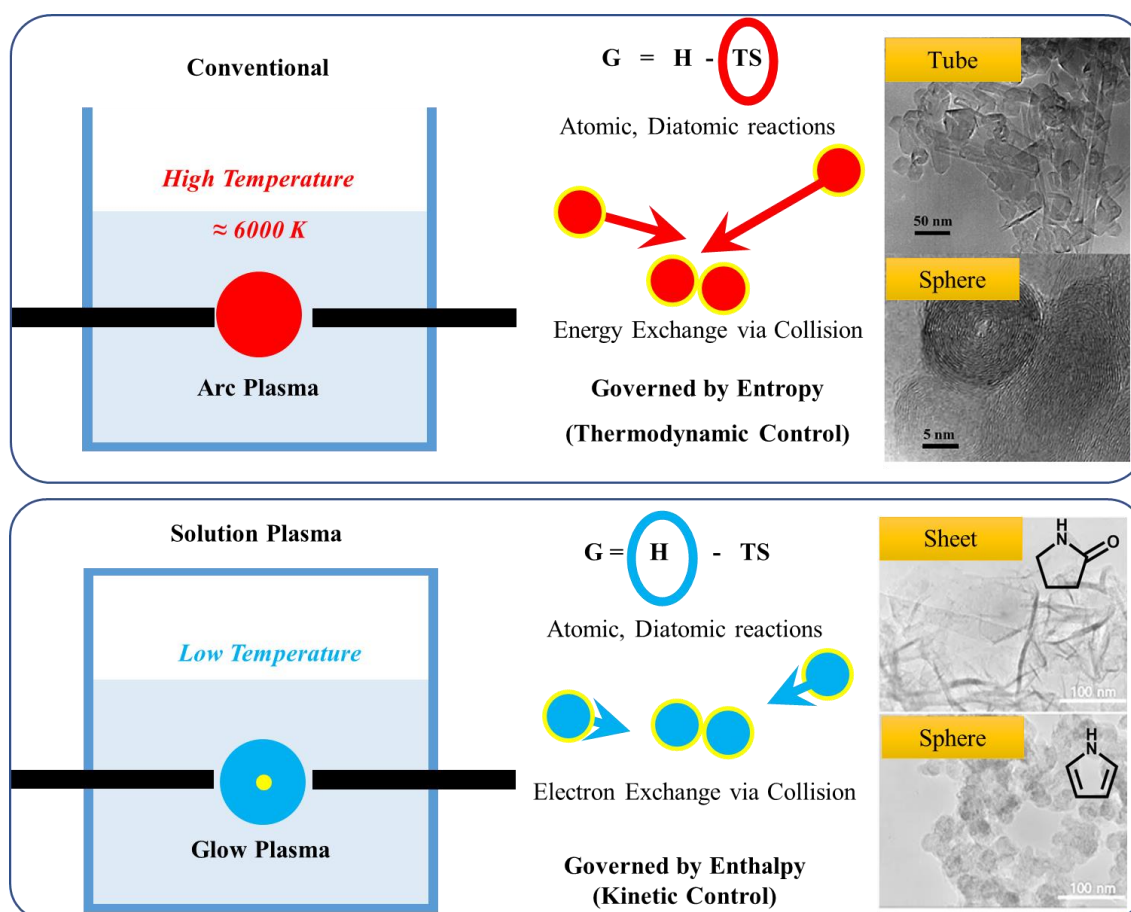
**Figure 1.4** The formation process of solution plasma.

### 1.3.1 Solution plasma process for nitrogen-doped graphene

Conventional thermal plasmas, such as arc plasmas, have reaction field temperatures of up to 6000 K [35], as shown in **Figure 1.5**. The chemical reaction processes are controlled by

thermodynamics at the molecular-atomic level. In other words, the reaction process is concerned with collision-induced energy exchange, *i.e.*, the entropy-governed reaction process.

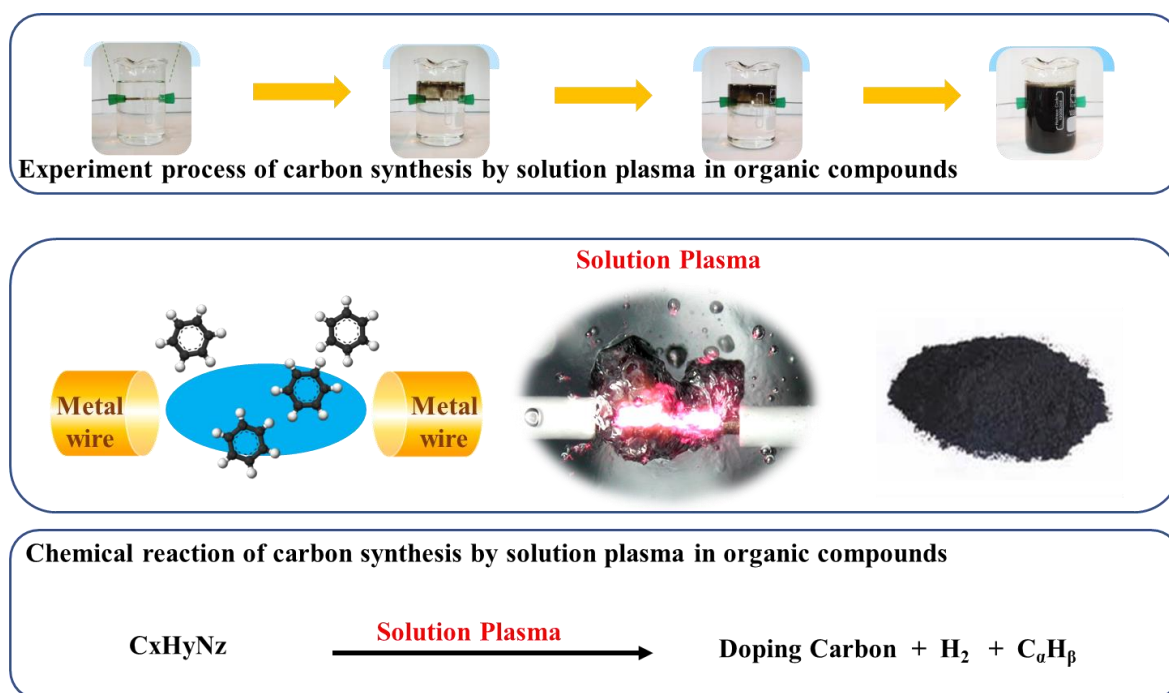
The utilization of thermal plasma allows the modulation of the shape of carbon materials, such as tube- or sphere-shaped products, which are more common in previous reports [35]. Solution plasma is a glow discharge mode. In the plasma reaction field, the electrons have high reactivity, and their temperature reaches 5000 K in general. However, the heavy particle temperature remains basically at room temperature. Their chemical reactions also occur at the molecular-atomic level, but the reaction process is controlled by kinetics [36]. The reaction process is concerned with the collision-induced electron exchange, *i.e.*, the enthalpy-governed reaction process. The same modulation of the carbon products in terms of shape changes, such as sheet- or sphere-shaped products, could be obtained using solution plasma [37].



**Figure 1.5** The difference between solution plasma and conventional thermal plasma process for the synthesis of carbon material.



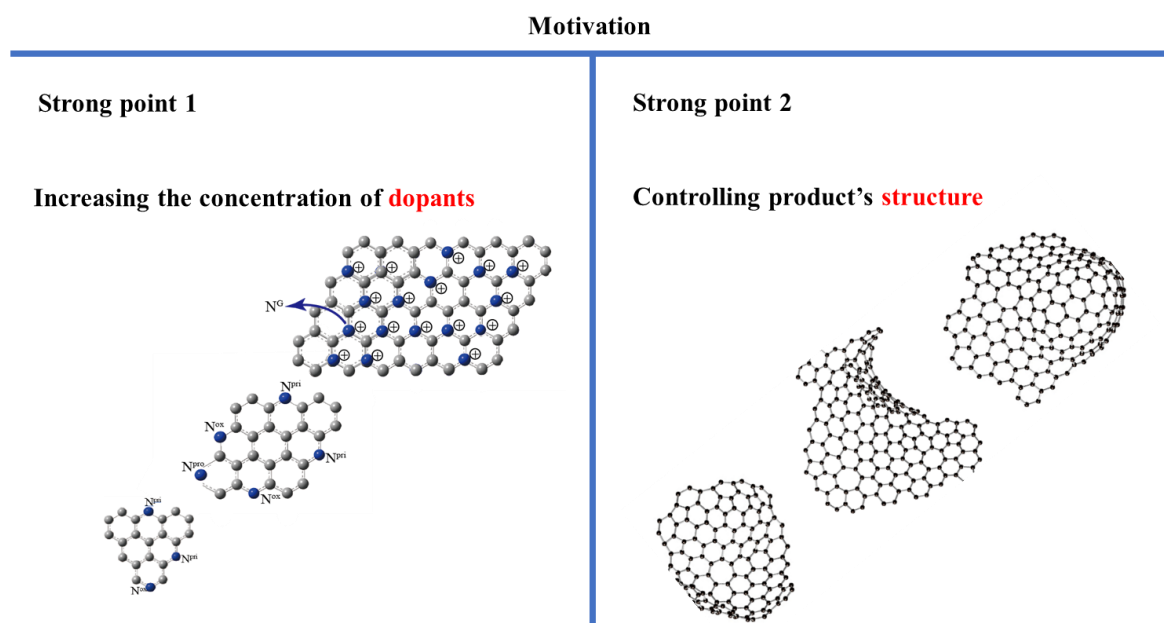
Combined analysis, the conventional arc discharge plasma can achieve the synthesis of tuned carbon product morphology. However, the higher reaction field temperature is not suitable for the synthesis of N-doped graphene materials. In other words, the process of thermodynamic control is not suitable for synthesized N-doped carbon material. As a contrast, the solution plasma process with higher reaction selectivity in the low-temperature field can provide a kinetic control reaction. The experiment process showed that the black component, which means the carbon, is gradually generated in several minutes of solution plasma discharge in **Figure 1.6**. The nitrogen atom in the raw materials will also join the reaction of carbon formation. Finally, the carbon black powder with relatively high nitrogen content can be easily produced, as shown in the chemical reaction.



**Figure 1.6** Experiment process, schematic diagram, and the chemical reaction of carbon materials synthesis by solution plasma in organic compounds.

The low plasma bulk temperature ensures that solution plasma has two strong points increasing the dopants concentration and controlling the structure of the carbon product. 2019, Chae *et al.* reported for the first time the synthesis of N-doped graphene with up to 13.4 at% heteroatom content by solution plasma technique in an ionic liquid organic solution by discharge [38]. Another highlight

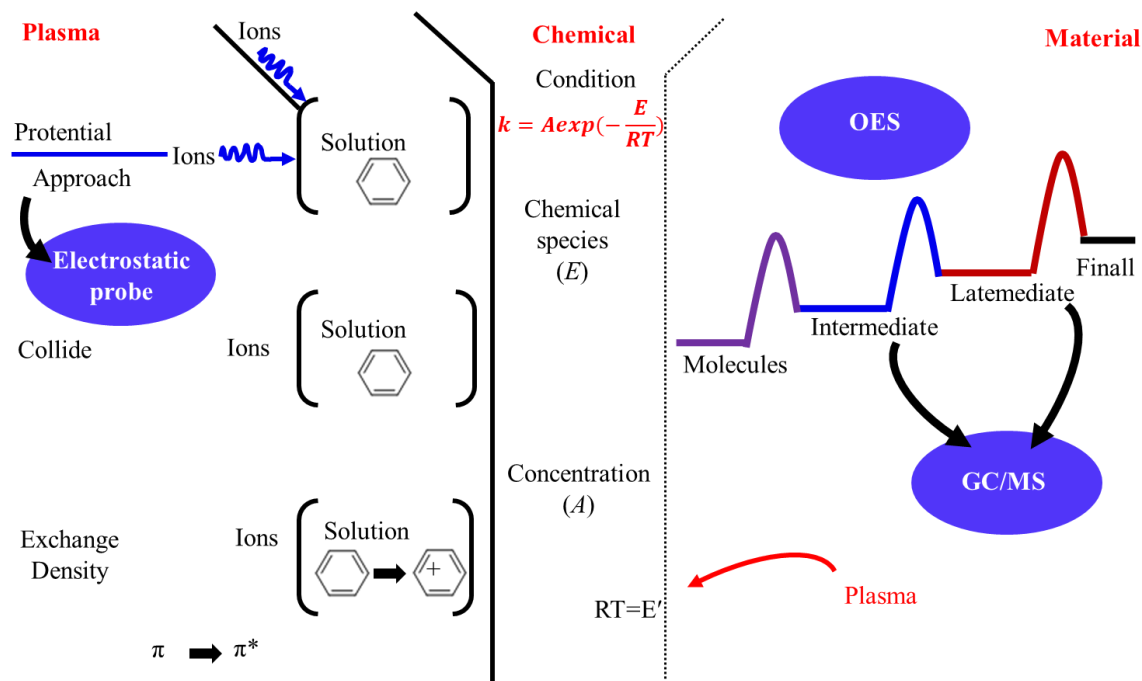
of this study is that the bonding type of N atoms is mainly graphitic, which means that the lone pair of electrons of N atoms maintain the planar character of the graphene framework by participating in  $\pi$ -bond conjugation of aromatic rings. The material also has high electrical conductivity precisely because doping enhances the electron density at the surface of the material. After this, Kim *et al.*, explored the chemical reaction pathway for the generation of N-doped carbon materials in a plasma reaction field using pyridine as the material [39-41]. Phu *et al.* synthesized novel catalysts with a core-shell structure of N-doped graphene material wrapped with metal nanoparticles using dimethylformamide (DMF) as the raw material [40,41]. The common feature of these studies is that the kinetic modulation of the chemistry by the low-temperature reaction field of the plasma is fully exploited, *i.e.*, the proportion of heteroatom doping is guaranteed while ensuring sufficient crystallinity of graphene. This provides sufficient assurance for the application of N-doped graphene in energy devices. It is also the motivation for this study, as shown in **Figure 1.7**.



**Figure 1.7** The motivation of this research includes increasing the dopants concentration and, at the same time, controlling the structure of the products.

### 1.3.2 Process information of solution plasma and the motivation from the current problem

Typical plasma technology involves a complex multidisciplinary intersection of physics, chemistry, and materials science. Numerous parameters include equipment-dependent parameters (*e.g.*, voltage, frequency of the power supply) and physical property parameters (*e.g.*, reactive species, electron density and so on) with complex relationships. These parameters directly affect the properties of the plasma reaction field and form a wide variety of process information, as shown in **Figure 1.8**. Plasma is generally understood as a bottom-up carbon synthesis technique where raw materials are decomposed into radicals, ions, and other carbon-containing molecular elements ( $C_2$  and CN as the basic fragments). In the action of high-energy electrons or ions driven by electric potential (can be detected by Langmuir probe), followed by polymerization (form the intermediates. Late mediates which can be detected by gas-chromatography–mass spectrometry (GC/MS)), aromatization, carbonization, and graphitization processes to form carbon with different characteristics [42-48]. The percentage of molecular elements, including radicals  $C_2^*$  and  $CN^*$ , in the initiation phase plays an important role in determining the properties of carbon, and it can be detected by optical emission spectroscopy (OES). In the reaction field of solution plasma, various process information in the discharge of organic compounds directly influences the structural parameters and performance of the final carbon products.



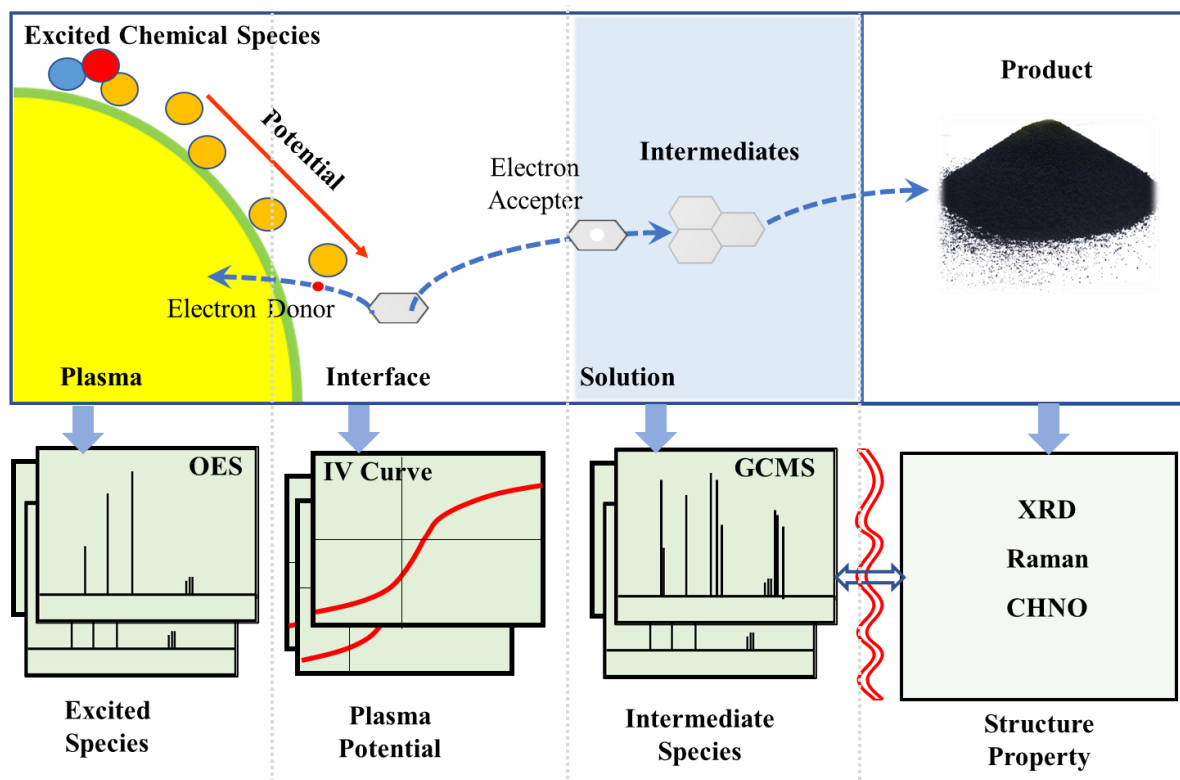
**Figure 1.8** Solution plasma process information of carbon generation in organic compounds, including plasma potential, active chemical species, and the chemical intermediate species.

Accordingly, there is no effective condition that can reasonably address how to regulate the plasma in a way that is guided by the desired high N-containing carbon materials. In 2015, Lee *et al.* tried to influence the synthesis of carbon products by regulating the discharge electrode spacing [49]. In 2017, Hyun *et al.* found that N-methyl-2-pyrrolidone (NMP) facilitated the formation of carbon products with higher crystallinity by changing the type of raw materials [37]. 2018, Li *et al.* investigated the synthesis of carbon products with different N-bonding types, including pyridinic-N, amino-N, and graphitic-N bonding, by solution plasma. [50]. They found that amino-N catalysts have higher electrochemical properties, *i.e.*, higher current density. The above studies can be found that scholars in this research field tried to find the most suitable experimental process design to obtain good N-doped graphene products. In other words, the main problem in this research field at present is the lack of process design for the solution plasma reaction field, which directly determines the desired final carbon product. In the current study, this process design addresses the issues regarding the N

content of carbon products, the N bonding configurations, and the crystallinity of the framework. The reaction process is also rationally regulated to maximize the desired reaction percentage.

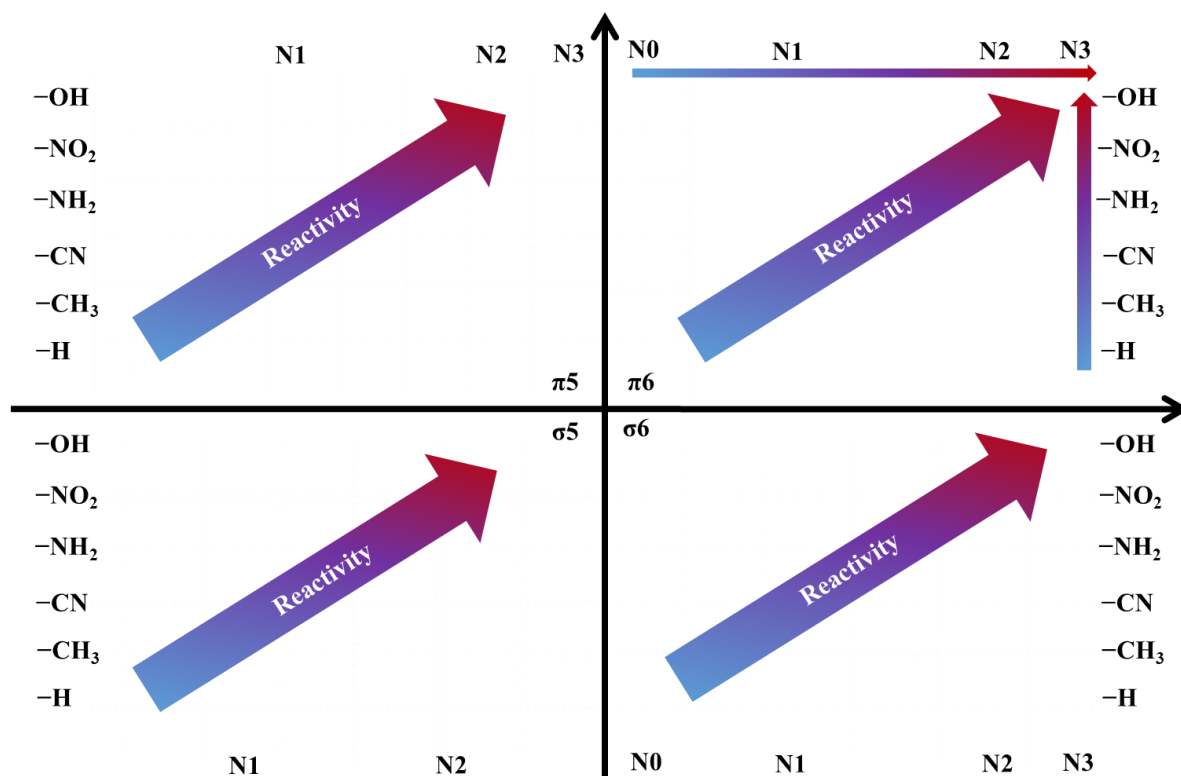
#### 1.4. Object and outline of the thesis

With this inspiration, utilizing the multivariate analysis to explore the correlation between the critical process in solution plasma and structural parameters of the synthesized high nitrogen-containing carbons was proposed, as shown in **Figure 1.9**. In detail, process information is widely acquired. It includes information about excited state chemicals from the plasma phase utilizing OES, information about intermediates from the liquid phase utilizing GC/MS, and information about the floating potential from the interfacial position utilizing the probe method. The above information obtained about the reaction field is also correlated with the structural parameters of the carbon product, including crystallinity information obtained by X-ray Diffraction (XRD), defect information obtained by Raman, and N content information obtained by the Elemental Analyzer. Finally, the synthesis path of carbon products with high N content based on the solution plasma reaction field is proposed, *i.e.*, the process design scheme. This will provide a roadmap for chemists, material scientists, and engineers who use solution plasma to complete the process.



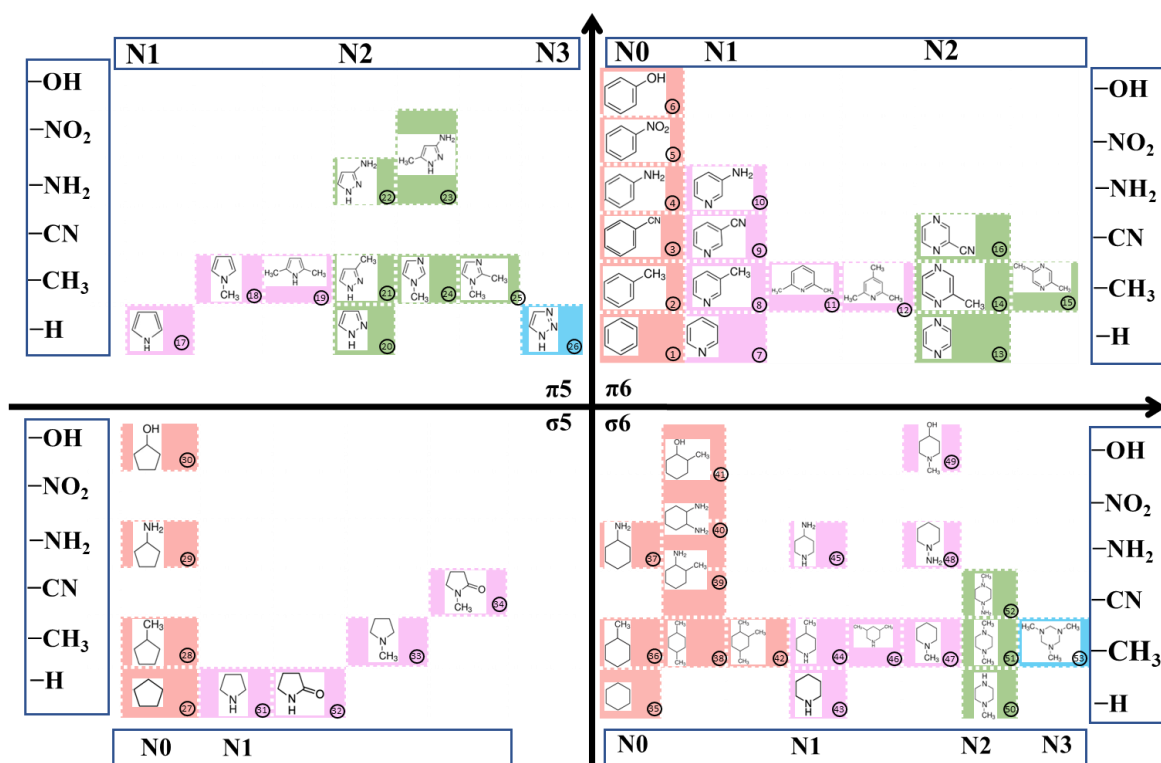
**Figure 1.9** The objective of this research includes exploring the excited species by OES from plasma phase, exploring the intermediates by GC/MS from the solution phase and exploring the potential information from the interface, and correlating the information of the plasma reaction field with the structural parameters of carbon products.

To ensure the rigor of the work, cyclic molecules with different reactivities were selected as raw materials from a systematic classification of precursors. The strategy of confirming raw materials of cyclic organic compounds is shown in **Figure 1.10**. Generally, molecules with 6-member ring structure have higher reactivity than molecules with 5-member ring structure, and  $\pi$ -bonding configuration has higher reactivity than  $\sigma$ -bonding configuration [37]. By this strategy, the primary categories of the compounds which including  $\sigma 5$ -,  $\pi 5$ -,  $\sigma 6$ -,  $\pi 6$ - were confirmed. In the secondary categories, the reactivity of compounds was increased with the increase of the number of heteroatoms in cyclic molecules. Due to the function group is strongly donate or withdraw electrons to the ring structure, the difference in electronegativity of elements adjacent to the carbon of ring structure is the criterion for determining the magnitude of reactivity of molecules with different function groups.



**Figure 1.10** The strategy of selecting the raw materials for the reaction field of solution plasma based on the general categorization of reactivity of organic compounds.

In conclusion, fifty-three organic compounds for solution plasma were identified by following the above strategy of categorizing and analyzing the reactivity. The relative thermodynamic and electrical properties of each compound are shown in **Appendix 1**. The confirmed raw materials of cyclic organic compounds are shown in **Figure 1.11**.



**Figure 1.11** The finally confirmed 53 raw materials with different functional groups and nitrogen numbers in the ring structure.

**In Chapter 2**, the correlation between patterns of optical emission spectroscopy with different dominations of active chemical species and carbon products with structural parameters in SP reaction field was explored. The two different power sources were applied to discharge in the categorized 53 raw materials, and the high-resolution optical spectrometer was used to get the spectrum of the plasma. How the dominated radicals affected the carbon products especially in the aspect of crystallinity and nitrogen content, was investigated. Finally, the properties of carbon products, including resistivity and hydrophobicity, were also explored to find the critical relation to guide the application of carbons to energy devices.

**In Chapter 3**, the correlation between the intermediate species and the carbon products with structural parameters in SP reaction field was explored. The gas chromatography with mass spectrometry (GC/MS) was applied to detect the intermediate molecules from the discharge of 53 raw



materials. The intermediates were categorized into groups according to the structures and nitrogen bonding components. The reaction routes based on different intermediates of carbon formation in the SP reaction field were finally proposed.

**In Chapter 4**, the correlation between the electric potential obtained from an electrostatic probe of different phases in SP and the carbon products with structural parameters was explored. The probe measurement systems were established based on the principle of Langmuir probe. By sweeping the position of probe, the potential of different phase, including plasma phase, gas phase and liquid phase were measured, followed by categorization. Finally, the kinetics process of the reaction in solution plasma for the formation of nitrogen-containing carbon products was proposed.

**In Chapter 5**, the optimal designing of a critical process in the synthesis of high nitrogen-containing carbons using SP by combining the conclusion of the multivariate analysis of the above chapters was proposed. A novel electrode geometry was proposed based on the dielectric barrier discharge, and the morphological, optical, and electric properties of plasma were also diagnosed. The nitrogen content and the bonding configuration of the carbon products were investigated to finally confirm the validity of multivariate analysis results.

**In Chapter 6**, the conclusion of this doctoral thesis was summarized.

## References

1. Qudrat-Ullah, H. A review and analysis of renewable energy policies and co2 emissions of pakistan. *Energy* **2022**, 238.
2. Hoang, A.T.; Foley, A.M.; Nižetić, S.; Huang, Z.; Ong, H.C.; Ölçer, A.I.; Pham, V.V.; Nguyen, X.P. Energy-related approach for reduction of co2 emissions: A critical strategy on the port-to-ship pathway. *Journal of Cleaner Production* **2022**, 355.
3. Olabi, A.G.; Abdelkareem, M.A. Renewable energy and climate change. *Renewable and Sustainable Energy Reviews* **2022**, 158.
4. Valdiserri, P.; Ballerini, V.; Rossi di Schio, E. Interpolating functions for co2 emission factors in

- dynamic simulations: The special case of a heat pump. *Sustainable Energy Technologies and Assessments* **2022**, 53.
5. Das, B.K.; Hassan, R.; Islam, M.S.; Rezaei, M. Influence of energy management strategies and storage devices on the techno-enviro-economic optimization of hybrid energy systems: A case study in western australia. *Journal of Energy Storage* **2022**, 51.
  6. Hannan, M.A.; Al-Shetwi, A.Q.; Begum, R.A.; Jern Ker, P.; Rahman, S.A.; Mansor, M.; Mia, M.S.; Muttaqi, K.M.; Dong, Z.Y. Impact assessment of battery energy storage systems towards achieving sustainable development goals. *Journal of Energy Storage* **2021**, 42.
  7. Lipu, M.S.H.; Mamun, A.A.; Ansari, S.; Miah, M.S.; Hasan, K.; Meraj, S.T.; Abdolrasol, M.G.M.; Rahman, T.; Maruf, M.H.; Sarker, M.R., *et al.* Battery management, key technologies, methods, issues, and future trends of electric vehicles: A pathway toward achieving sustainable development goals. *Batteries* **2022**, 8.
  8. da Silva Lima, L.; Cocquyt, L.; Mancini, L.; Cadena, E.; Dewulf, J. The role of raw materials to achieve the sustainable development goals: Tracing the risks and positive contributions of cobalt along the lithium-ion battery supply chain. *Journal of Industrial Ecology* **2022**.
  9. Salameh, T.; Kumar, P.P.; Olabi, A.G.; Obaideen, K.; Sayed, E.T.; Maghrabie, H.M.; Abdelkareem, M.A. Best battery storage technologies of solar photovoltaic systems for desalination plant using the results of multi optimization algorithms and sustainable development goals. *Journal of Energy Storage* **2022**, 55.
  10. Lebrouhi, B.E.; Baghi, S.; Lamrani, B.; Schall, E.; Kousksou, T. Critical materials for electrical energy storage: Li-ion batteries. *Journal of Energy Storage* **2022**, 55.
  11. Suzdaltsev, A. Silicon electrodeposition for microelectronics and distributed energy: A mini-review. *Electrochem* **2022**, 3, 760-768.
  12. Lee, C.-K. The field of applied mechanics: Historical outlook from past to present and its implications for future applications. *Journal of Mechanics* **2022**, 38, 586-597.
  13. Wang, Z.; Wang, Y.; Wang, J.; Song, Y.; Robson, M.J.; Seong, A.; Yang, M.; Zhang, Z.; Belotti,

- A.; Liu, J., *et al.* Rational design of perovskite ferrites as high-performance proton-conducting fuel cell cathodes. *Nature Catalysis* **2022**.
14. Wu, Z.; Yu, Y.; Zhang, G.; Zhang, Y.; Guo, R.; Li, L.; Zhao, Y.; Wang, Z.; Shen, Y.; Shao, G. In situ monitored (n, o)-doping of flexible vertical graphene films with high-flux plasma enhanced chemical vapor deposition for remarkable metal-free redox catalysis essential to alkaline zinc-air batteries. *Adv Sci (Weinh)* **2022**, *9*, e2200614.
15. Yan, G.; Kim, G.; Yuan, R.; Hoenig, E.; Shi, F.; Chen, W.; Han, Y.; Chen, Q.; Zuo, J.M.; Chen, W., *et al.* The role of solid solutions in iron phosphate-based electrodes for selective electrochemical lithium extraction. *Nat Commun* **2022**, *13*, 4579.
16. Wheeler, S.E.; Bloom, J.W. Anion- $\pi$  interactions and positive electrostatic potentials of n-heterocycles arise from the positions of the nuclei, not changes in the  $\pi$ -electron distribution. *Chem Commun (Camb)* **2014**, *50*, 11118-11121.
17. Su, D.; Cortie, M.; Wang, G. Fabrication of n-doped graphene-carbon nanotube hybrids from prussian blue for lithium-sulfur batteries. *Advanced Energy Materials* **2016**, *7*.
18. Xing, Z.; Ju, Z.; Zhao, Y.; Wan, J.; Zhu, Y.; Qiang, Y.; Qian, Y. One-pot hydrothermal synthesis of nitrogen-doped graphene as high-performance anode materials for lithium ion batteries. *Sci Rep* **2016**, *6*, 26146.
19. Wang, K.; Xu, M.; Gu, Y.; Gu, Z.; Liu, J.; Fan, Q.H. Low-temperature plasma exfoliated n-doped graphene for symmetrical electrode supercapacitors. *Nano Energy* **2017**, *31*, 486-494.
20. Souqui, L.; Palisaitis, J.; Högberg, H.; Pedersen, H. Plasma cvd of b-c-n thin films using triethylboron in argon-nitrogen plasma. *Journal of Materials Chemistry C* **2020**, *8*, 4112-4123.
21. Soares, J.A.N.T.; Kim, H.; Glass, G.; Desjardins, P.; Greene, J.E. Arsenic-doped si(001) gas-source molecular-beam epitaxy: Growth kinetics and transport properties. *Applied Physics Letters* **1999**, *74*, 1290-1292.
22. Lim, D.; Downer, M.C.; Ekerdt, J.G. Second-harmonic spectroscopy of bulk boron-doped si(001). *Applied Physics Letters* **2000**, *77*, 181-183.

23. Arora, R.; Rozen, J.; Fleetwood, D.M.; Galloway, K.F.; Zhang, C.X.; Han, J.; Dimitrijević, S.; Kong, F.; Feldman, L.C.; Pantelides, S.T., *et al.* Charge trapping properties of 3c- and 4h-sic mos capacitors with nitrided gate oxides. *IEEE Transactions on Nuclear Science* **2009**, *56*, 3185-3191.
24. Inagaki, M.; Toyoda, M.; Soneda, Y.; Morishita, T. Nitrogen-doped carbon materials. *Carbon* **2018**, *132*, 104-140.
25. Kaur, M.; Kaur, M.; Sharma, V.K. Nitrogen-doped graphene and graphene quantum dots: A review on synthesis and applications in energy, sensors and environment. *Adv Colloid Interface Sci* **2018**, *259*, 44-64.
26. Wang, H.; Maiyalagan, T.; Wang, X. Review on recent progress in nitrogen-doped graphene: Synthesis, characterization, and its potential applications. *ACS Catalysis* **2012**, *2*, 781-794.
27. Sharma, P.P.; Wu, J.; Yadav, R.M.; Liu, M.; Wright, C.J.; Tiwary, C.S.; Yakobson, B.I.; Lou, J.; Ajayan, P.M.; Zhou, X.D. Nitrogen-doped carbon nanotube arrays for high-efficiency electrochemical reduction of CO<sub>2</sub>: On the understanding of defects, defect density, and selectivity. *Angew Chem Int Ed Engl* **2015**, *54*, 13701-13705.
28. Yadav, R.; Dixit, C.K. Synthesis, characterization and prospective applications of nitrogen-doped graphene: A short review. *Journal of Science: Advanced Materials and Devices* **2017**, *2*, 141-149.
29. Zhang, G.; Zhu, J.; Zeng, W.; Hou, S.; Gong, F.; Li, F.; Li, C.C.; Duan, H. Tin quantum dots embedded in nitrogen-doped carbon nanofibers as excellent anode for lithium-ion batteries. *Nano Energy* **2014**, *9*, 61-70.
30. Zitolo, A.; Goellner, V.; Armel, V.; Sougrati, M.T.; Mineva, T.; Stievano, L.; Fonda, E.; Jaouen, F. Identification of catalytic sites for oxygen reduction in iron- and nitrogen-doped graphene materials. *Nat Mater* **2015**, *14*, 937-942.
31. Mishra, S.; Nguyen, H.; Adusei, P.K.; Hsieh, Y.-Y.; Shanov, V. Plasma enhanced synthesis of nitrogen-doped vertically aligned carbon nanofibers on 3d graphene. *Surface and Interface Analysis* **2019**, *51*, 290-297.
32. Guo, Y.; Zhang, S.; Zhang, R.; Wang, D.; Zhu, D.; Wang, X.; Xiao, D.; Li, N.; Zhao, Y.; Huang,

- Z., *et al.* Electrochemical nitrate production via nitrogen oxidation with atomically dispersed Fe on n-doped carbon nanosheets. *ACS Nano* **2021**.
33. Deokar, G.; Jin, J.; Schwingenschlögl, U.; Costa, P.M.F.J. Chemical vapor deposition-grown nitrogen-doped graphene's synthesis, characterization and applications. *npj 2D Materials and Applications* **2022**, *6*.
34. Allahbakhsh, A. Nitrogen-doped graphene quantum dots hydrogels for highly efficient solar steam generation. *Desalination* **2021**, *517*.
35. Charinpanitkul, T.; Sano, N.; Muthakarn, P.; Tanthapanichakoon, W. Enhancing effect of monoolein surfactant on carbon nanoparticle synthesis by arc discharge in liquid. *Materials Research Bulletin* **2009**, *44*, 324-327.
36. Takai, O. Solution plasma processing (spp). *Pure and Applied Chemistry* **2008**, *80*, 2003-2011.
37. Hyun, K.; Saito, N. The solution plasma process for heteroatom-carbon nanosheets: The role of precursors. *Sci Rep* **2017**, *7*, 3825.
38. Chae, S.; Panomsuwan, G.; Bratescu, M.A.; Teshima, K.; Saito, N. P-type doping of graphene with cationic nitrogen. *ACS Applied Nano Materials* **2019**, *2*, 1350-1355.
39. Kim, K.; Hashimi, K.; Bratescu, M.A.; Saito, N. The initial reactions from pyridine to hetero-carbon nanomaterials through solution plasma. *Nanoscience and Nanotechnology Letters* **2018**, *10*, 814-819.
40. Phan, P.Q.; Naraprawatphong, R.; Pornaroontham, P.; Park, J.; Chokradjaroen, C.; Saito, N. N-doped few-layer graphene encapsulated Pt-based bimetallic nanoparticles via solution plasma as an efficient oxygen catalyst for the oxygen reduction reaction. *Materials Advances* **2021**, *2*, 322-335.
41. Pootawang, P.; Saito, N.; Lee, S.Y. Discharge time dependence of a solution plasma process for colloidal copper nanoparticle synthesis and particle characteristics. *Nanotechnology* **2013**, *24*, 055604.
42. Dong, M.; Chan, G.C.Y.; Mao, X.; Gonzalez, J.J.; Lu, J.; Russo, R.E. Elucidation of c2 and cn

- formation mechanisms in laser-induced plasmas through correlation analysis of carbon isotopic ratio. *Spectrochimica Acta Part B: Atomic Spectroscopy* **2014**, *100*, 62-69.
43. Goebel, J.H.; Bregman, J.D.; Cooper, D.M.; Goorvitch, D.; Langhoff, S.R.; Witteborn, F.C. The  $C_2$ ,  $C_2$ , and  $CN$  electronic absorption bands in the carbon star HD 19557. *The Astrophysical Journal* **1983**, *270*.
44. Miyamoto, K.; Narita, S.; Masumoto, Y.; Hashishin, T.; Osawa, T.; Kimura, M.; Ochiai, M.; Uchiyama, M. Room-temperature chemical synthesis of  $C_2$ . *Nat Commun* **2020**, *11*, 2134.
45. Li, J.; Xiong, Z.; Zeng, K.; Zhong, D.; Zhang, X.; Chen, W.; Nzihou, A.; Flamant, G.; Yang, H.; Chen, H. Characteristics and evolution of nitrogen in the heavy components of algae pyrolysis bio-oil. *Environ Sci Technol* **2021**, *55*, 6373-6385.
46. Weber, M.; Wolf, J.C.; Haisch, C. Gas chromatography-atmospheric pressure inlet-mass spectrometer utilizing plasma-based soft ionization for the analysis of saturated, aliphatic hydrocarbons. *J Am Soc Mass Spectrom* **2021**, *32*, 1707-1715.
47. Wang, X.; Pilewskie, J.; Hsu, H.W.; Horányi, M. Plasma potential in the sheaths of electron-emitting surfaces in space. *Geophysical Research Letters* **2016**, *43*, 525-531.
48. Zmarzły, D.; Frącz, P. Measurement of dielectric liquid electrification in the shuttle system with two parallel electrodes. *Energies* **2021**, *14*.
49. Lee, H.; Ueno, T.; Saito, N. The effect of electrode gap distance on the synthesis of carbon materials by using solution plasma process. *Jom* **2015**, *67*, 2550-2556.
50. Li, O.L.; Wada, Y.; Kaneko, A.; Lee, H.; Ishizaki, T. Oxygen reduction reaction activity of thermally tailored nitrogen-doped carbon electrocatalysts prepared through plasma synthesis. *ChemElectroChem* **2018**, *5*, 1995-2001.

## ***Chapter 2***

***Excited Chemical Species Produced by  
Solution Plasma in Cyclic Organic Compounds  
and the Structural Correlation  
with the Raw Molecules***

## ***Chapter 2 - Excited Chemical Species Produced by Solution Plasma in Cyclic Organic Compounds and the Structural Correlation with the Raw Molecules***

### **2.1 Introduction**

Plasma is generally known as a bottom-up synthesis of heteroatom-doped carbon materials, in which raw materials are decomposed into radicals, ions, and other carbon fragments, such as  $C_2^*$  and  $CN^*$ , by the collision of high-energy electrons [1-5]. After the decomposition, polymerization, carbonization, and graphitization processes are followed, respectively, to form carbon particles with different characteristics [6]. General perspective to understand, the number of decomposed fragments, *i.e.*,  $C_2^*$  and  $CN^*$ , plays an important role in determining the properties of carbon [3,7-15].

In the SP process, the decomposition of raw materials or organic molecules with heteroatoms to form the fragments [16], *i.e.*,  $C_2^*$  and  $CN^*$ , occurs at the plasma phase. The decomposed fragments are further polymerized at the plasma-liquid interface, which has a much lower temperature [17-29]. The low temperature is one of a key to preventing the vaporization of light elements (*e.g.*, N atom) and improving the heteroatom doping ratio in the carbon [30-33].

In the reaction field of SP, atoms and molecules are excited to different levels under conditions of inelastic collisions of free electrons [20,34-38]. The shelf-time of the excited species is usually short on the order of nanoseconds and can only be relaxed by means of photon radiation. Different atoms or molecules radiate in a specific wavelength range, which corresponds to the potential energy difference between the upper excited state and the lower layer [39-41]. These radiations can be analyzed using a high-resolution optical emission spectrometer and are presented as a peak profile [41]. It provides



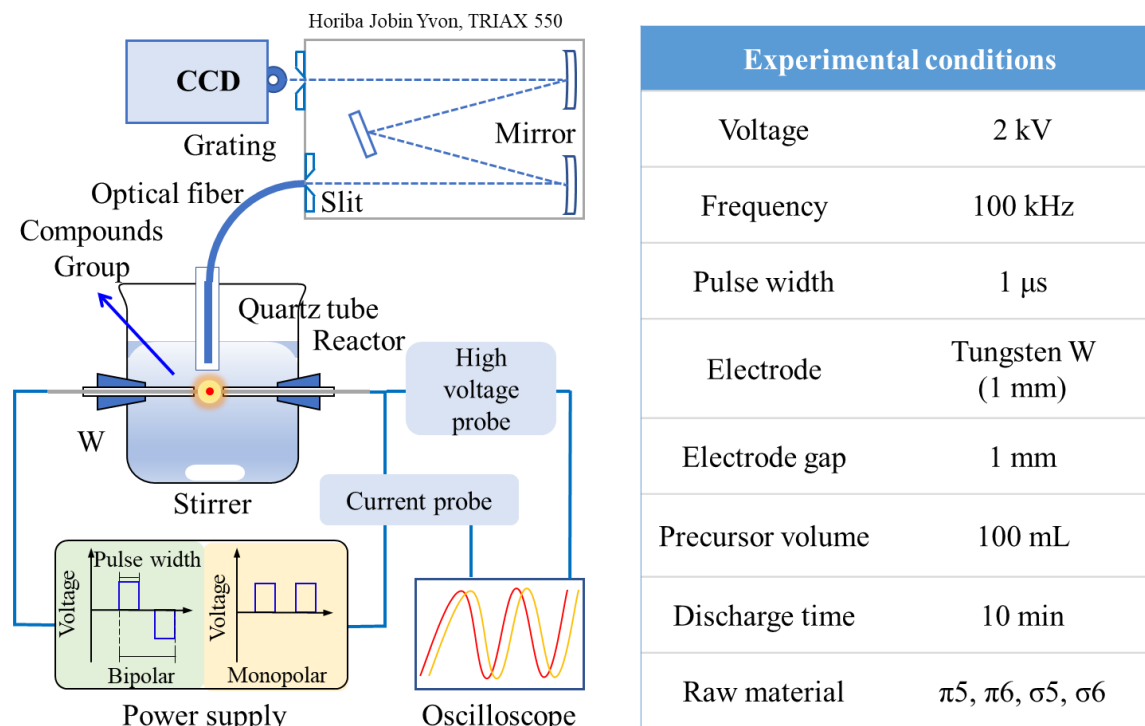
information about the emitted species in the reaction field, which are the fundamental sources of particles that form carbon particles. Our group has been intensively investigating the synthesis of carbon using SP. Morishita, T. *et al* [22] employed OES to measure the radical composition of SP formed in cyclic molecules as well as in chain molecule raw materials. The typical feature is a large amount of  $C_2^*$  radicals; similar characteristic spectra are also shown in Chae, S. *et al* [17-19] and Maria, A. *et al* [42]. These studies showed that SP could be used to synthesize several carbon materials with different structural features, such as core-shell structures of nitrogen-doped carbon-coated metals, nitrogen-doped carbon quantum dots and so on. However, this research still faced the limitation in doping heteroatoms into carbon framework.

Therefore, it is challenging to deeply investigate the relationship of radicals, ions, and decomposed fragments with the structure and properties of carbon products synthesized by SP which can lead to the improvement of SP and overcome the limitation in doping heteroatoms into carbon framework. Based on this motivation, in this study, a systematic study was conducted. A correlation between the peak profiles obtained by OES in the plasma and the structural parameters of carbon products was expected, based on the hypothesis that the excited chemical species at plasma-liquid interfaces can induce the kinetically-controlled chemical reactions, *i.e.*, polymerization of carbon [36,37]. To ensure the reliability of the correlation, 53 cyclic molecules without and with nitrogen contents as dopants or functional groups with different reactivities were selected as raw materials and systematically rearranged, as shown in **Figure 1.11**. The conventional bipolar pulse discharge SP and newly proposed monopolar pulse discharge SP were used to synthesize carbons, as shown in **Figure 2.3**. The emission spectra dominated by different radicals for different raw materials were obtained. The parameters of the carbon synthesized in SP reaction field were conducted using XRD, Raman and Elemental analyzer. The properties of the carbon, including resistivity and wettability, were also obtained. The analytical method of the ternary phase diagram was applied, and the correlation mapping between OES patterns and carbon products was expected.

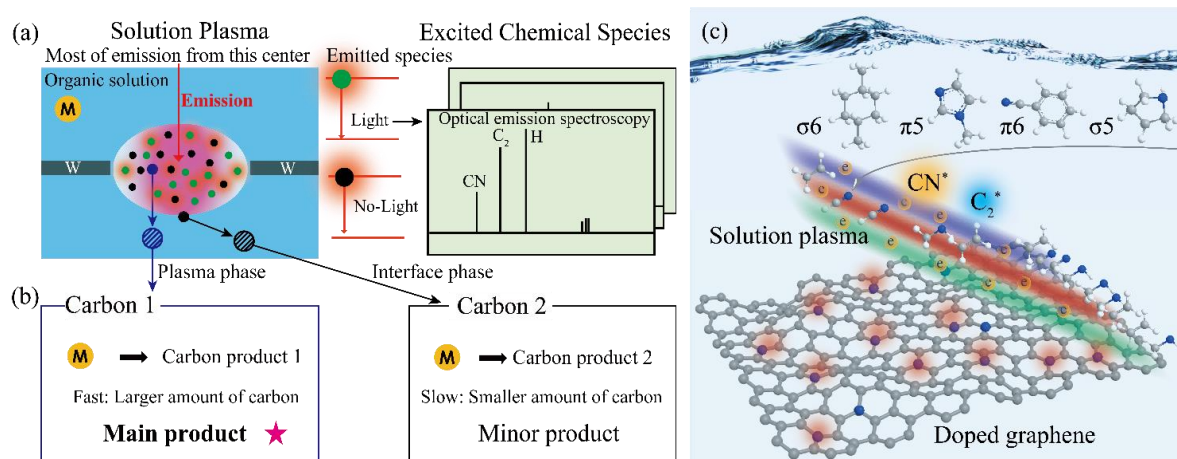
## 2.2 Experimental procedures

In the research, the typical electrode structure which is named pin-to-pin geometry (**Figure 2.1**) was applied for plasma conducting and carbon production. The discharge environment is an organic solution, which is a cyclic compound. Most of the photon emission was coming from the plasma center, which was located in the plasma phase. The emission light could be captured, and the exact radical information was shown in OES, as shown in **Figure 2.2a**. Except plasma phase, there also exists an interface phase located between plasma and solution, and the carbon product is minor due to the smaller reaction area with lower energy, as shown in **Figure 2.2b**. In contrast, the main product of carbon came from the plasma phase due to the larger bulk volume. The schematic diagram of obtaining N-doped graphene as the target product in SP is shown in **Figure 2.2c**. The discharge power sources include, for the first time, a monopolar pulse in addition to the conventional bipolar pulse, as shown in **Figure 2.3**. From the viewpoint of the kinetic process, the monopolar pulse could continuously provide a single-side electric field, which derived the mobile orientation of the active particles. It provided theoretical support for the directional growth of the carbon framework. Therefore, the innovative application of monopolar pulse SP was expected to make it easier to obtain the desired target material, *i.e.*, N-doped graphene.

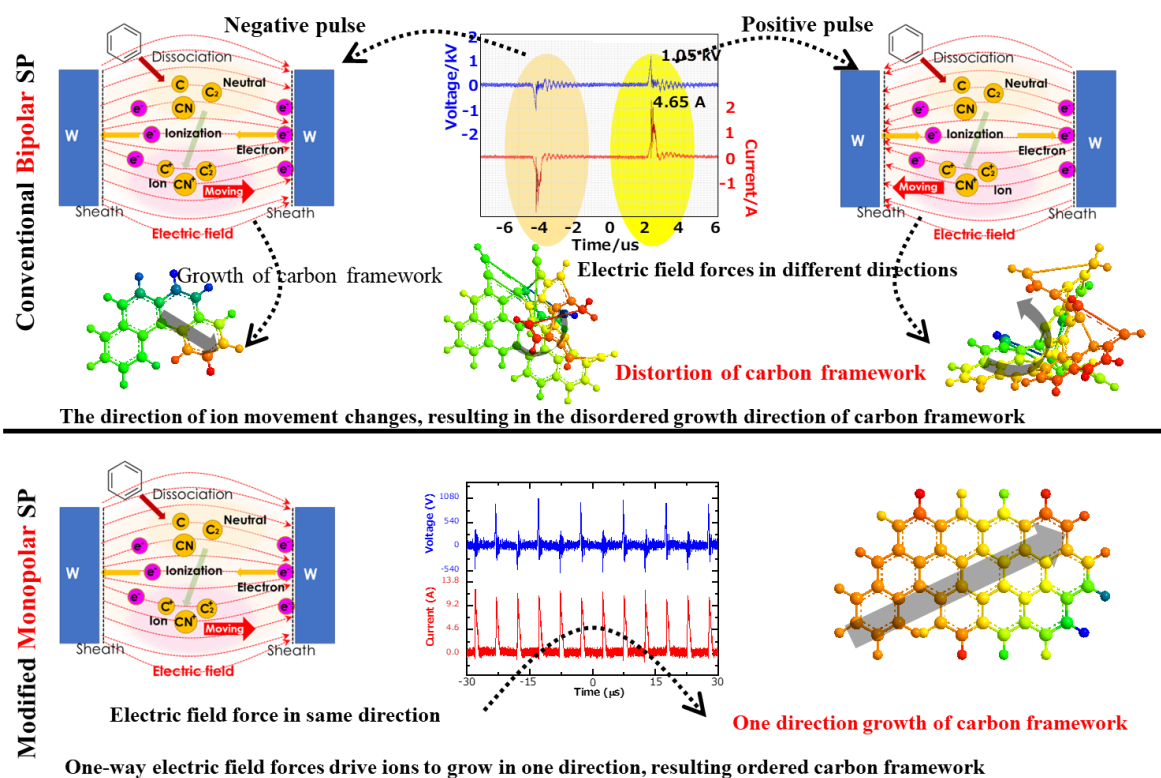
A pin-to-pin electrode structure with the high voltage electrode and the ground electrode was applied for the plasma generating and carbon production, the schematic of the setup of the experiment is shown in **Figure 2.1**. The electrode was a tungsten rod (W,  $\phi$  1.0 mm, Nilaco Co, Japan) covered with a ceramic tube ( $\phi$  2.0 $\times$ 0.5 $\times$ 100(H) mm, Nilaco Co, Japan). The SP was driven by a bipolar pulse (MPS-R06K01C-WP1-6CH, Kurita, Japan) or monopolar pulse power supply (MPP04-A4-30, Kurita, Japan). The voltage and current were measured by the high-voltage probe (P6015A, 1000X, 3.0 pF, 100 M $\Omega$ , Tektronix, USA) and current probe (PR30, Yokogawa, Japan), respectively. The signal was recorded by a digital oscilloscope (DLM2024, 2.5 GS/s, 200 MHz, Yokogawa, Japan).



**Figure 2.1** Schematic of the experiment setup and exactly conditions



**Figure 2.2** (a) The discharge environment and the emission site of solution plasma. Both the generation of OES and carbon materials were conducted from the same phase, *i.e.*, plasma phase, there must or might have one kind of correlation with each other. (b) The location of the reaction field and carbon formation process. Main product of carbon is come from the plasma phase due to the bigger volume of the reaction field. (c) Schematic diagram illustrating the synthesis target material, *i.e.*, N-doped carbon materials, in the solution plasma process.



**Figure 2.3** Bipolar- and monopolar- pulse electric properties and mechanism of growth of carbon.

The released light of chemical species, *i.e.*, radicals, was captured with a high-resolution optical emission spectrograph (Horiba Jobin Yvon, TRIAX 550) coupled with a back-illuminated CCD detector, and the wavelength range was 200–1000 nm. The optical fiber detector was covered by a quartz tube to be put as close to the plasma as possible. The instrument broadening of the spectrum could be inhibited by this method. A volume of 100 ml baker placed with a magnetic stirrer was used as a container to complete the experiment. The carbon-producing condition is shown in the graph of Figure S1. The organic solution with a purity higher than 99.5% was purchased from Kanto Chemical Co., Inc, Japan. The black carbon powder was obtained after SP, followed by vacuum filtration and oven drying at 80 °C for 12 h.

The crystallinity of the carbon products was conducted by X-ray diffraction (XRD, Smartlab, Rigaku Co., Japan) with a Cu K $\alpha$  ( $\lambda = 0.154$  nm) X-rays source. The electronic surface potential, *i.e.*, changing the polarizability of the electron density of the surface of carbon, was conducted by Raman

spectra microscope (Raman, Leica DM 2500M Ren (RL/TL), Renishaw Plc, England) utilizing a laser wavelength of 532.5 nm. The elemental composition was obtained by Elemental analysis (EA) with Perkin Elmer 2400 Series II CHNS/O analyzer. The resistivity of the carbon material was obtained by measuring the specific shape (15 mm in diameter and 0.18 mm in thickness) of the carbon pellet pressed (60 MPa in pressure) with carbon powder (25 mg in amount) through four-point probe meter (Loresta-GP MCP-T610, Mitsubishi Chemicals). The water contact angle of the carbon pallet was measured by a 2  $\mu$ L droplet of distilled water to obtain the wettability property.

### 2.3 Results and discussion

Similar OES patterns were obtained with bipolar- and monopolar-pulse SP of each group of raw materials (**Figure 2.4-2.7**). The components of the spectra strongly depended on the chemical structure of the raw materials. The spectral analysis showed that the main radicals were  $H_{\alpha}^*$ ,  $C_2^*$ ,  $CN^*$  and the identification of atoms, molecules, and radicals' transitions in the emission spectra is shown in **Table 2.1**. For the  $\pi_6$  group, the increase in the intensity of  $C_2^*$  emission spectra was exhibited as the reactivity of functional groups increased, as shown in **Figure 2.4**. A decrease in the intensity of  $C_2^*$  emission spectra was exhibited when nitrogen existed in the benzene ring. The possible reason was that the reactivity of the benzene ring could be greatly reduced because the nitrogen was a pyridinic type, which had the lone pair electrons and do not involve in the conjugation hybridization [37]. The opposite phenomenon was found in the  $\pi_5$  group, as shown in **Figure 2.5**, where the lone pair electrons of pyrrolic nitrogen formed a conjugate hybridization with the carbon atom, resulting in the enhancement of the reactivity on the ring, and thus there was a gradual increase in  $C_2/CN^*$  emission intensity [18]. In this work, this nitrogen atom was called an accelerator N.

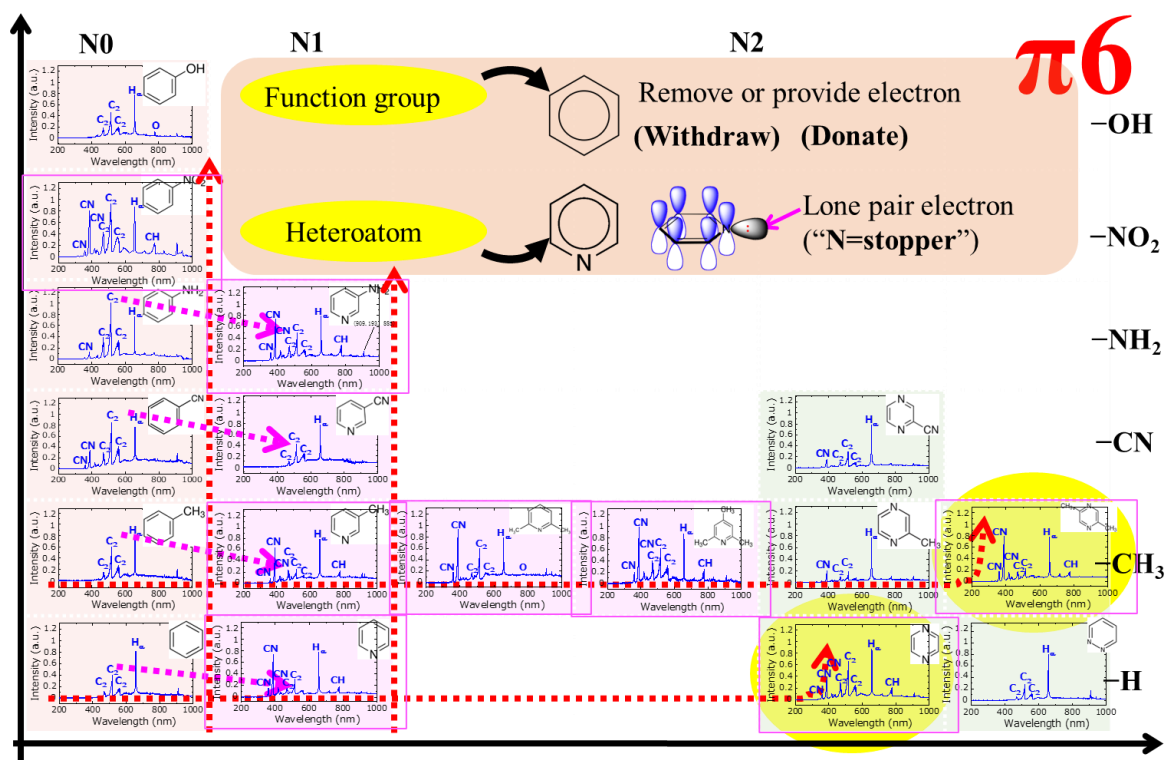


Figure 2.4 Optical emission spectra of the  $\pi_6$  group of raw materials.

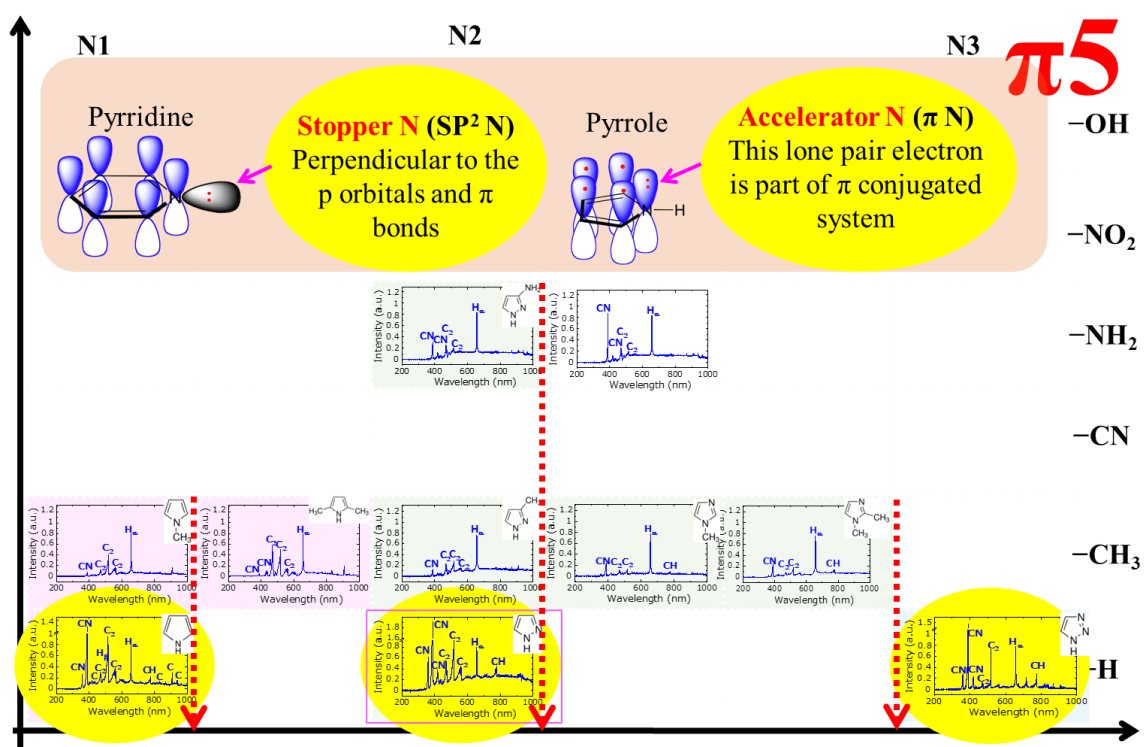
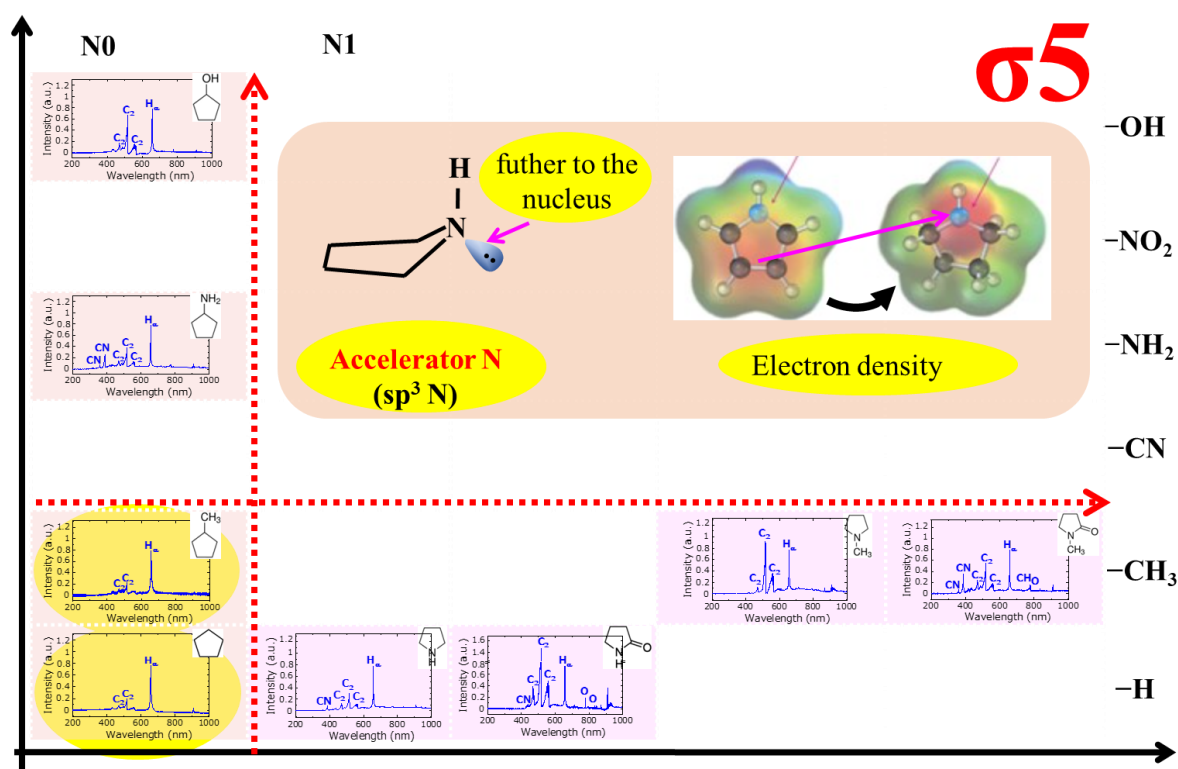


Figure 2.5 Optical emission spectra of the  $\pi_5$  group of raw materials.

For  $\sigma_5$  group, as shown in **Figure 2.6** the bonding configuration of nitrogen atom with  $sp^3$  configuration led to the lone pair electrons close to the proton, causing the increment of the reactivity at the nitrogen atom [37], which was called accelerator N. For  $\sigma_6$  group, the obtained spectra were revealed to be dominated by  $H^*$  to  $C_2/CN^*$  due to the high reactivity of molecules in the  $\sigma_6$  group, as shown in **Figure 2.7**. The ternary phase diagram indicated the relative intensity of excited chemical species in plasma from OES (*i.e.*,  $H_\alpha^*$ ,  $C_2^*$ ,  $CN^*$ ) was constructed as shown in **Figure 2.8**. The patterns of OES were classified into 4 categories, including  $H^*$ ,  $C_2^*$ ,  $CN^*$  and  $C_2/CN^*$  domination.



**Figure 2.6** Optical emission spectra of the  $\sigma_5$  group of raw materials.

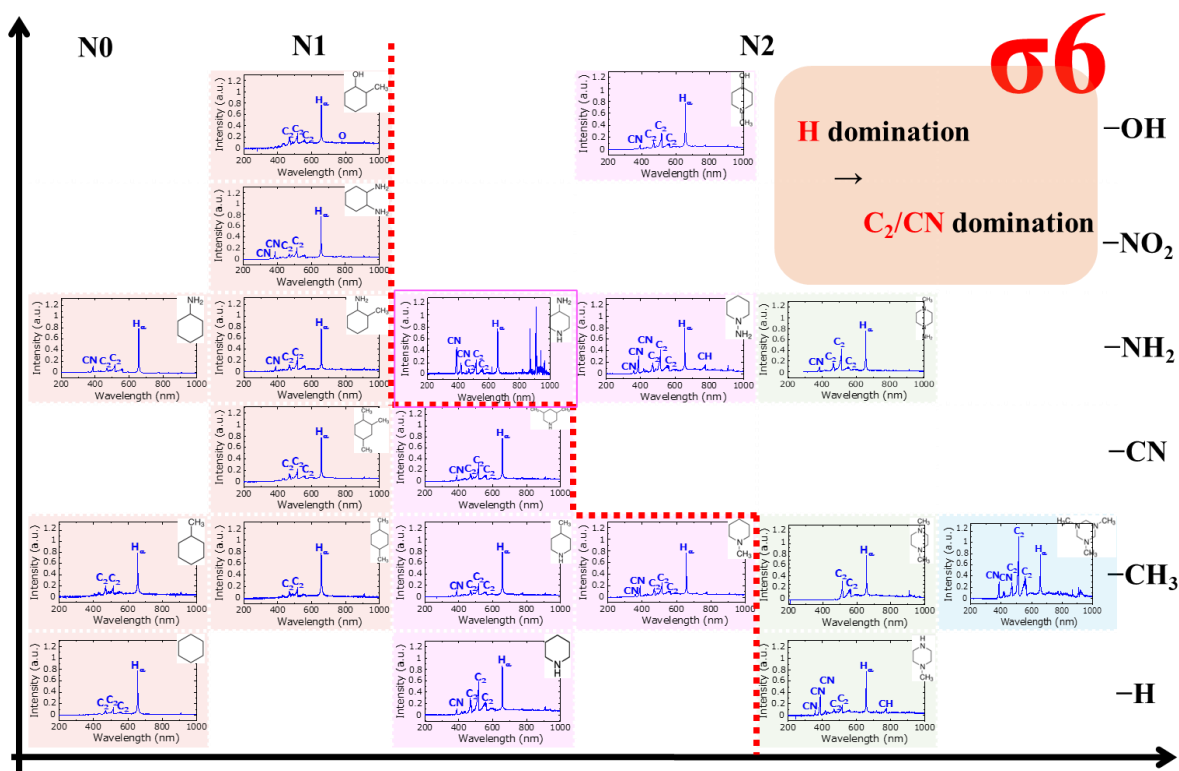


Figure 2.7 Optical emission spectra of the  $\sigma_6$  group of raw materials.

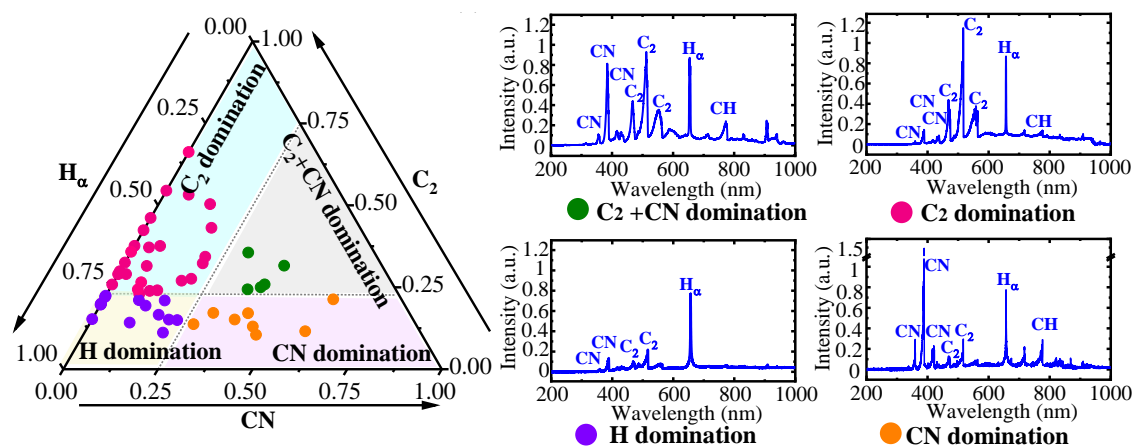


Figure 2.8 Ternary phase diagram of the cyclic organic compounds by following the patterns of OES with comparing the intensity of the radicals of  $H^*$ ,  $CN^*$  and  $C_2^*$  and the exactly typical OES patterns of  $C_2/CN^*$ ,  $C_2^*$ ,  $H^*$ , and  $CN^*$  domination.



**Table 2.1** Identification of atoms, molecules, and radicals' transitions in the emission spectra.

Transition band [21,41-48]	Wavelength (nm)	Transition	Particles
Swan system	516.5, 471.5, 547.0, 558.0	$d^3\Pi_g - a^3\Pi_u$	$C_2$
Swan system under high pressure	589.9	$d^3\Pi_g - a^3\Pi_u$	$C_2$
Deslandres cf azambuja system	385.2, 360.7, 358.7	$c^1\Pi_g - b^1\Pi_u$	$C_2$
Violet system	388.3, 415.2	$B^2\Sigma^+ - X^2\Sigma^+$	CN
Benzene cation	545.3		$C_6H_6^+$
Carbon molecule anion	545.3	$^2\Sigma - ^2\Sigma$	$C_2^-$
Fulcher $\alpha$ Hydrogen molecule	600 - 630	$d^3\Pi_u - a^3\Sigma_g^+$	$C_2$
Balmer series	656.0, 486.1, 434.0	$n=5-2, 4-2, 3-2$	$H_\alpha, H_\beta, H_\gamma$
Oxygen	777, 844.6	$^5P - ^5S_0, ^3P - ^3S_0$	O

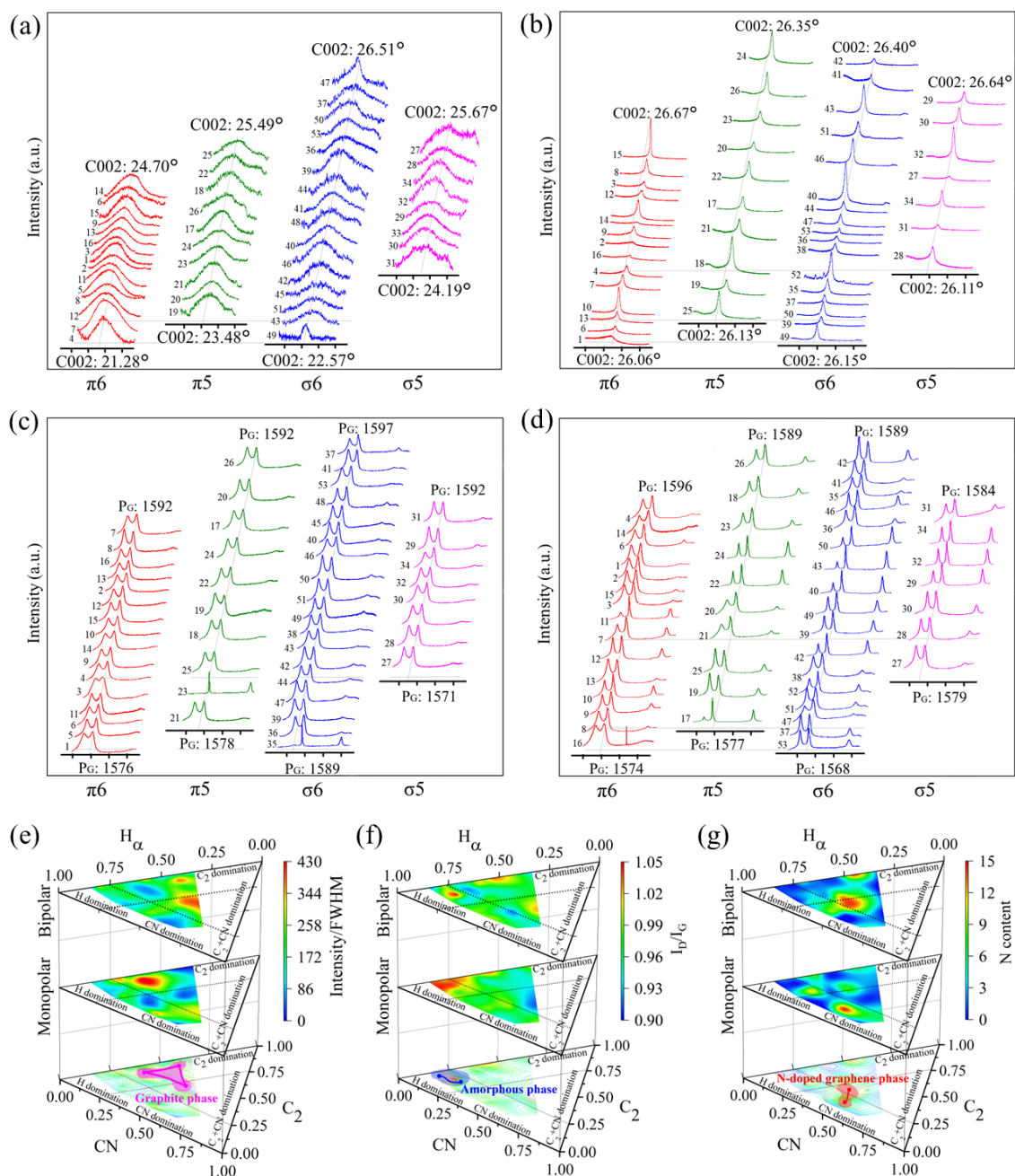
The XRD patterns obtained from the carbon samples synthesized by bipolar- and monopolar-pulse SP were shown in **Figure 2.9(a)**, (b). Carbon samples from monopolar pulse SP showed higher C002 peak intensity and lower FWHM, compared to that of bipolar pulse SP. The crystallinity was further analyzed by intensity/FWHM as shown in the ternary contour plot (**Figure 2.9e**). The OES spectra of carbon samples, which showed the strong intensity of  $C_2^*$  peak of  $C_2^*$  domination exhibited high crystallinity for both cases of the bipolar- and monopolar- pulse discharges. However, the OES spectra of carbon samples from the monopolar pulse discharge with the strong intensity of  $CN^*$  peak of  $CN^*$  domination also had relatively high crystallinity. The overall crystallinity of carbon samples from the bipolar pulse discharge was lower than that of monopolar pulse discharge. The main reason might be that the plasma during the monopolar pulse discharge showed a higher discharge current, which could enhance the dehydrogenation reaction (**Figure 2.3**). Moreover, by assuming the local thermodynamic equilibrium of SP and employing the relative intensities of Balmer H lines, the electron excitation temperature could be obtained. The results showed that the reaction field

dominated by  $C_2^*$  had a higher temperature. This evidence proved that electron and thermal transformation simultaneously facilitated the formation of the graphitic structure due to large amounts of the  $C_2^*$  radicals which induced the generation of  $\pi$ -bonding or  $\pi^*$  anti-bonding orbitals.

Furthermore, the electronic surface potential of a molecular system through vibrational and rotational states was obtained by Raman spectroscopy, as shown in **Figure 2.9c** and d. The ternary contour plot of  $I_D/I_G$  with respect to the OES patterns was constructed, as shown in **Figure 2.9f**. For both bipolar- or monopolar-pulse discharge, the carbon samples obtained from the reaction field containing mainly hydrogen of  $H^*$  domination exhibited large  $I_D/I_G$ . According to the electron excitation temperature, it could indicate that the plasma with relatively low energy could mainly generate decomposed hydrogen bonds. Thus, carbon samples with a large number of C-H bonds in  $sp^3$  structure were obtained [37], which influenced a polarization of the electron density in  $sp^2$  hybridized bonding configuration of the carbon surface. Accordingly, it could be concluded that the carbon products from SP system with  $H^*$  domination were an amorphous phase.

The correlation between the OES patterns and nitrogen content in the carbon sample from bipolar- or monopolar- pulse discharge was shown in **Figure 2.9g**. The carbon samples with high content of N were found to be obtained from the bipolar pulse SP with  $C_2^*$  domination and monopolar pulse SP with  $CN^*$  domination. It was because, from the OES patterns of SP with  $C_2/CN^*$  domination, the temperature of the reaction field could be calculated and found to be excessive, which led to the vaporization of the nitrogen element. Thus, the nitrogen doping content was relatively low. However, the OES patterns of  $C_2^*$  and  $CN^*$  dominated SP showed that the moderate temperatures could be obtained, which should promote the dehydrogenation process and suppress the vaporization of light element, such as nitrogen. This feature is more clearly reflected in the correlation of OES and carbon from monopolar pulsed SP. That is, the  $CN^*$  in the reaction field of plasma would serve as the molecular element of the nucleation and growth of N contained structure of carbon. According to **Figure 2.9e** and f, the carbon samples with the high nitrogen content had a high degree of crystallinity and low amount of disordered structure. It indicated that the carbon with high N content contributed to the formation of the graphene structure, and the kinetic diagram was obtained as shown in the

overlapping of the above ternary contour plot. The above results provided the information that the  $C_2^*$  or  $CN^*$  radicals could serve as primary units in carbon allotrope by the formation of  $sp^2/sp^3$  bonded cluster/domain sizes.



**Figure 2.9** X-ray diffraction (XRD) patterns of carbon from (a) bipolar pulse SP; (b) monopolar pulse SP. Raman spectra of carbon from (c) bipolar pulse SP; (d) monopolar pulse SP. Ternary contour plot of the correlation between OES patterns and properties of carbon of bipolar- and monopolar-pulse SP,

and kinetic phase diagram of carbon under OES patterns determined from overlapping the ternary contour plot. (e) Crystallinity level by index of intensity/FWHM from XRD, and graphite phase was confirmed by concatenating the centers. (f)  $I_D/I_G$  from Raman of carbon, and amorphous phase was confirmed by concatenating the centers. (g) N doping content from EA of carbon and N-doped graphene was confirmed.

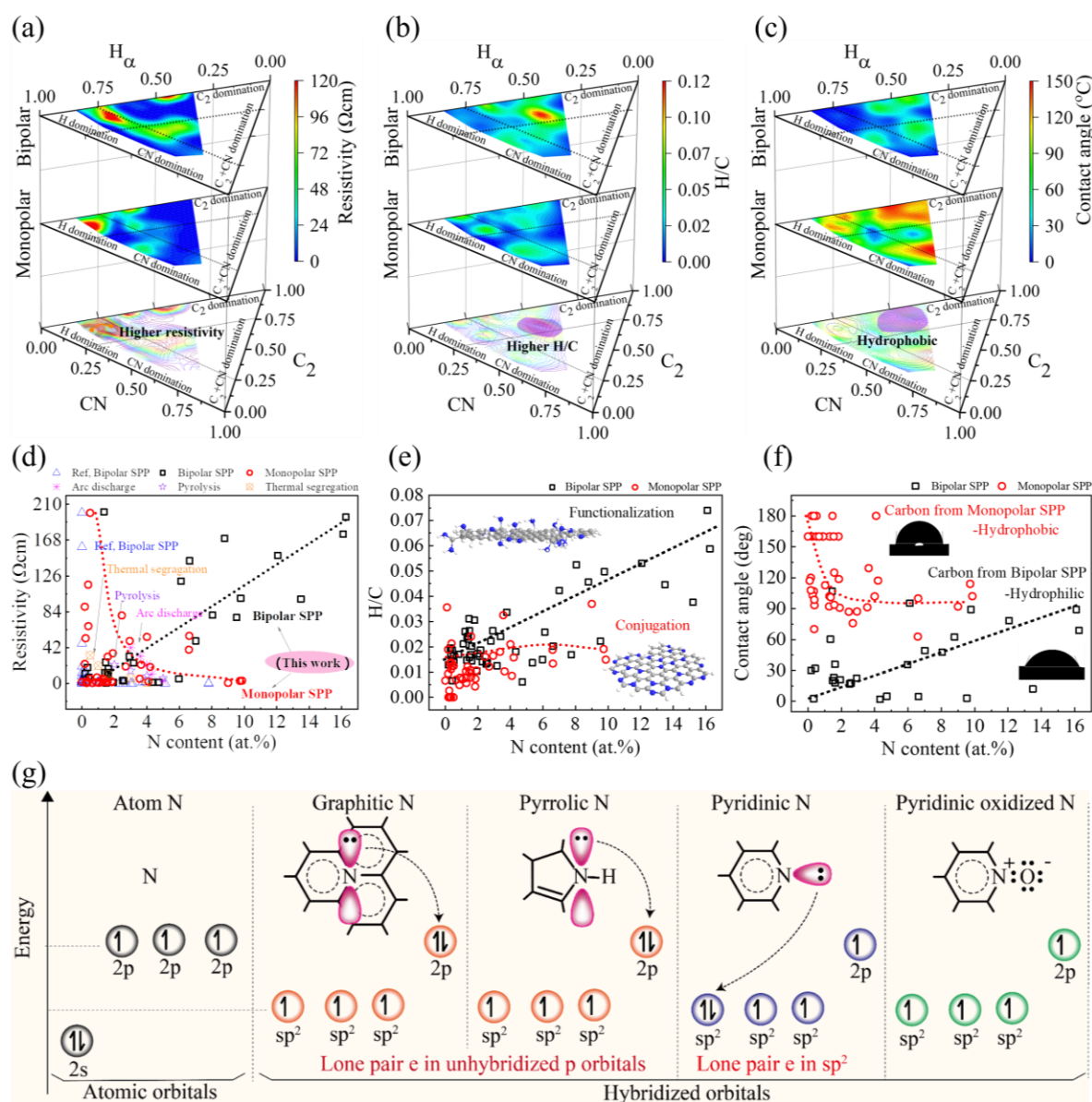
The above analysis showed the correlation between the structure of carbon and OES patterns; however, the information on the properties and performance of carbon samples were still necessary to acquire the direction for synthesizing carbon materials by SP, aiming to apply in a lithium-ion battery. One of the important properties is resistivity which relates to carrier movement. **Figure 2.10a** shows the correlation between the OES patterns and resistivities of carbon products from bipolar- or monopolar-pulse discharge. The carbon products from both bipolar- or monopolar-pulse discharge with  $H^*$  domination exhibited relatively high resistivity. This could be correlated with the OES patterns in **Figure 2.9a**. The synthesized carbon samples from SP with  $H^*$  domination were mostly amorphous phase. Consequently, it could refer that the high content of  $sp^3$  bonding configuration could lead to hinder the carrier mobility on the carbon surface.

The result of the ratio of H/C, as indicated in **Figure 2.10b**, demonstrated the carbon of  $C_2^*$  domination of bipolar pulse SP demonstrated higher H/C. The same features as the correlation of N content and OES pattern are shown in **Figure 2.9c**. In contrast, the correlation of H/C and OES patterns of carbon from monopolar pulse SP was not shown any strong correlation. To further understand the essential reasons for the appearance of the above phenomena, the effects of different types of bonding configurations of doped N on carrier transport were analyzed, as shown in **Figure 2.10g**. It is noteworthy that the inhibiting or inducing of carrier transport would be affected when heteroatom N were doped into the carbon with different bonding configurations. The ability to increase the carrier's transport followed the order as below: graphitic N > pyrrolic N > pyridinic N > pyridinic oxidized N > N containing function group. Graphitic N maintains a planar structure while lone pair of electrons,

which was in the unhybridized  $p$  orbitals, formed conjugated  $\pi$ -bonds with adjacent carbon atoms. As a result, a local electron-rich region was formed, which enhanced the electrostatic force of electron propagation on the carbon surface. However, the presence of pyrrolic N and pyridinic N in the carbon framework also introduced boundaries. Since the lone pair of electrons of pyrrolic N was involved in the aromatic ring hybridization, while the lone pair of electrons of pyridinic N was in the  $sp^2$  hybridization orbital. Thus, pyrrolic N had a stronger ability to induce electron transport than pyridinic N. For pyridinic oxidized N, the presence of greater electronegativity of the oxygen element makes the electron pair more shifted toward it, thus enhancing the carrier blockage problem due to boundary effects. In N containing function group, the withdrawing or donating electron brings the unbalance of electron density of the carbon surface. However, it exhibited obstruction in the carrier movement process.

Based on the above understanding, the performances of resistivity vs N content of this work were compared with other reported N-doped carbon materials (**Figure 2.10d**). The carbon synthesized by conventional SP, pyrolysis, thermal segregation, and arc discharge had gradually decreased resistivity as the percentage of N content increased. However, the N content was low. The carbon produced by the bipolar pulse SP used in this work showed a gradual increase in resistivity with increasing N content, as well as a gradual increase in the H/C ratio (**Figure 2.10e**), which indicated that N was present in the carbon in the form of functional groups. On the contrary, the carbon produced by monopolar pulse SP proposed in this work had a decrease in resistivity while enhancing the N content. And the H/C ratio (**Figure 2.10e**) was essentially constant as the N content increased. It indicated that monopolar discharge plasma could conduct substitution of C by N in the  $\pi$  conjugated bonding system. It was possible that this replacement was more in the form of graphitic N. However, it might also include pyrrolic N or pyridinic N. It should also be noted that the conductivity of the carbon synthesized in this work had a certain gap compared to that of commercial graphite, which was probably since the Fermi energy level of the carbon was opened after the nitrogen doping and thus had semiconductor properties.

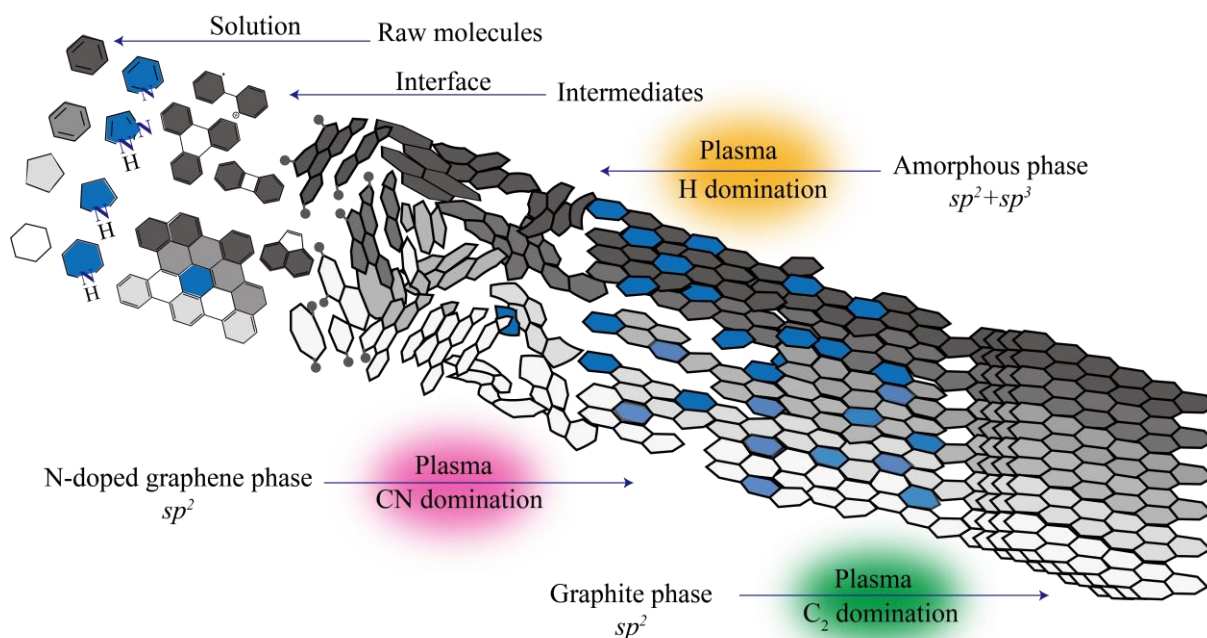
In addition, based on the understanding of the electrical characteristics of carbon synthesized by this work, the information about the hydrophilic or hydrophobic properties of carbon by measurement of water contact angle was further obtained. The results are shown in **Figure 2.10c** for carbon synthesized of bipolar- or monopolar-pulse SP. The carbon synthesized from the bipolar pulse discharge with  $C_2^*$  domination had a larger water contact angle. Meanwhile, the carbon character of this part tended to be close to the graphite and N-doped graphene phase. This might be due to the presence of  $\pi$ -bonds resulting in an overall lower polarity of electron density of the carbon surface, and the surface energy of this part of carbon was lowered, thus insufficient to resist hydrogen bonding of water molecules. Additionally, it should be noted that the contact angle of carbon synthesized by monopolar pulse discharge was higher than that synthesized by bipolar, as shown in **Figure 2.10f**. Its properties are close to hydrophobic to superhydrophobic. The possible reason might be due to the higher degree of graphitization of carbon synthesized by monopolar plasma. The N-doped carbon with lower resistivity and higher hydrophobicity has great potential to be applied in energy storage devices (*e.g.*, a lithium-ion battery) which is configured with organic electrolytes. These properties could provide sufficient wetting contact degree between electrolyte and electrode while reducing the impedance of lithium-ion exchange or intercalation/deintercalation[49,50]. Consequently, the plasma with  $H^*$  domination was highly susceptible to the formation of highly resistive amorphous carbon with the structure of  $sp^3$  bonding.



**Figure 2.10** Ternary contour plot of the correlation between OES patterns and carbon properties: (a) Resistivity of carbon of bipolar- and monopolar-pulse SP. (b) H/C ratio of carbon of bipolar- and monopolar-pulse SP. (c) The water contact angle of carbon of bipolar- and monopolar-pulse SP. (d) Resistivity vs N content of this work and refs. (e) H/C vs N content. (f) Contact angle vs N content. (g) Simplified schematic of orbitals of N dopants with different bonding configurations.

**Figure 2.11** shows the schematic diagram illustrating the transformation of raw molecules into various carbon phases under the different domination of the excited species in the SP process. The

organic molecules in the solution were first decomposed by the high-energy electrons generated in the plasma to obtain the decomposed fragments such as  $C_2^*$ ,  $CN^*$ . These fragments could further undergo polymerization to form intermediates containing polyaromatic rings at the interface between the plasma and the solution. Different radical-dominated plasmas have different effects on the intermediates in the subsequent carbonization and graphitization processes. Specifically, in the  $H^*$  dominated spectral plasma, the final carbon products tended to be mostly the amorphous phase of  $sp^2+sp^3$ . This part of the carbon had a high H/C value as well as a high resistivity. In  $CN$ -dominated spectral plasma, the final carbon products tended to be N-doped graphene phase with  $sp^2$  as the dominant bonding configuration, and the hydrophobic nature of this carbon was another typical feature. It has good applications in organic electrolyte-based energy applications, such as lithium-ion batteries. In the plasma with  $C_2^*$  as the dominant spectrum, the final carbon product tended to be  $sp^2$ -dominated graphite phase. It has a low resistivity characteristic. It is evident that the methodology based on the correlation between OES patterns and carbon products proposed in this study was a clear guideline for carbon product synthesis in SP.



**Figure 2.11** In solution plasma, the structural units increase in doping content and crystallinity with different domination of  $H^*$ ,  $C_2^*$ ,  $CN^*$  and  $C_2/CN^*$ .



## 2.4 Conclusion

This study revealed the relationship between the obtained carbon products and the plasma-generated radical components by investigating the correlation of OES patterns and characteristics of the obtained carbon products, aiming to improve the synthesis of N-doped graphene using SP. The reaction fields in SP dominated by  $H^*$ ,  $C_2^*$ , and  $CN^*$  sequentially promoted amorphous carbon, graphitic, and N-doped graphene, respectively. The low-defect graphene with nitrogen doping in the carbon framework by conjugation could be obtained by monopolar-pulse SP with  $CN^*$  or  $C_2/CN^*$  domination. The high-defect graphene with nitrogen content as a functional group on the surface was obtained by bipolar pulse SP with  $C_2^*$  domination. The systematic research could lead to a clear understanding of the reaction field for the synthesis of carbon materials from organic compounds by SP. Finally, the research was expected to open new opportunities for plasma-based technologies in material science and engineering.

## References

1. Tian, Y.; Wu, P.; Wu, X.; Jiang, X.; Xu, K.; Hou, X. Corona discharge radical emission spectroscopy: A multi-channel detector with nose-type function for discrimination analysis. *Analyst* **2013**, *138*, 2249-2253.
2. Xing, Z.; Ju, Z.; Zhao, Y.; Wan, J.; Zhu, Y.; Qiang, Y.; Qian, Y. One-pot hydrothermal synthesis of nitrogen-doped graphene as high-performance anode materials for lithium ion batteries. *Sci Rep* **2016**, *6*, 26146.
3. Souqui, L.; Palisaitis, J.; Högberg, H.; Pedersen, H. Plasma cvd of b–c–n thin films using triethylboron in argon–nitrogen plasma. *Journal of Materials Chemistry C* **2020**, *8*, 4112-4123.
4. Mishra, S.; Nguyen, H.; Adusei, P.K.; Hsieh, Y.-Y.; Shanov, V. Plasma enhanced synthesis of n doped vertically aligned carbon nanofibers on 3d graphene. *Surface and Interface Analysis* **2019**, *51*, 290-297.
5. Hamann, S.; Rond, C.; Pipa, A.V.; Wartel, M.; Lombardi, G.; Gicquel, A.; Röpcke, J. Spectroscopic study of h2microwave plasmas with small admixtures of ch4and b2h6used for

- doped diamond deposition. *Plasma Sources Science and Technology* **2014**, *23*.
- Zhang, B.; Jiang, Y.; Balasubramanian, R. Synthesis, formation mechanisms and applications of biomass-derived carbonaceous materials: A critical review. *Journal of Materials Chemistry A* **2021**, *9*, 24759-24802.
  - Dong, M.; Chan, G.C.Y.; Mao, X.; Gonzalez, J.J.; Lu, J.; Russo, R.E. Elucidation of c2 and cn formation mechanisms in laser-induced plasmas through correlation analysis of carbon isotopic ratio. *Spectrochimica Acta Part B: Atomic Spectroscopy* **2014**, *100*, 62-69.
  - Goebel, J.H.; Bregman, J.D.; Cooper, D.M.; Goorvitch, D.; Langhoff, S.R.; Witteborn, F.C. The c2h, c2, and cn electronic absorption bands in the carbon star hd 19557. *The Astrophysical Journal* **1983**, *270*.
  - Lherbier, A.; Blase, X.; Niquet, Y.M.; Triozon, F.; Roche, S. Charge transport in chemically doped 2d graphene. *Phys Rev Lett* **2008**, *101*, 036808.
  - Miyamoto, K.; Narita, S.; Masumoto, Y.; Hashishin, T.; Osawa, T.; Kimura, M.; Ochiai, M.; Uchiyama, M. Room-temperature chemical synthesis of c2. *Nat Commun* **2020**, *11*, 2134.
  - Miyamoto, K.; Narita, S.; Masumoto, Y.; Hashishin, T.; Osawa, T.; Kimura, M.; Ochiai, M.; Uchiyama, M. Reply to "a thermodynamic assessment of the reported room-temperature chemical synthesis of c2". *Nat Commun* **2021**, *12*, 1245.
  - Tan, X.Q.; Ng, S.F.; Mohamed, A.R.; Ong, W.J. Point-to-face contact heterojunctions: Interfacial design of 0d nanomaterials on 2d g-c3n4 towards photocatalytic energy applications. *Carbon Energy* **2022**.
  - Tantardini, C.; Oganov, A.R. Thermochemical electronegativities of the elements. *Nat Commun* **2021**, *12*, 2087.
  - Wu, Z.; Yu, Y.; Zhang, G.; Zhang, Y.; Guo, R.; Li, L.; Zhao, Y.; Wang, Z.; Shen, Y.; Shao, G. In situ monitored (n, o)-doping of flexible vertical graphene films with high-flux plasma enhanced chemical vapor deposition for remarkable metal-free redox catalysis essential to alkaline zinc-air batteries. *Adv Sci (Weinh)* **2022**, *9*, e2200614.
  - Zaplotnik, R.; Primc, G.; Vesel, A. Optical emission spectroscopy as a diagnostic tool for

- characterization of atmospheric plasma jets. *Applied Sciences* **2021**, *11*.
16. Kireev, D.; Liu, S.; Jin, H.; Patrick Xiao, T.; Bennett, C.H.; Akinwande, D.; Incorvia, J.A.C. Metaplastic and energy-efficient biocompatible graphene artificial synaptic transistors for enhanced accuracy neuromorphic computing. *Nat Commun* **2022**, *13*, 4386.
  17. Chae, S.; Bratescu, M.A.; Saito, N. Synthesis of few-layer graphene by peeling graphite flakes via electron exchange in solution plasma. *The Journal of Physical Chemistry C* **2017**, *121*, 23793-23802.
  18. Chae, S.; Panomsuwan, G.; Bratescu, M.A.; Teshima, K.; Saito, N. P-type doping of graphene with cationic nitrogen. *ACS Applied Nano Materials* **2019**, *2*, 1350-1355.
  19. Chae, S.; Phan, P.Q.; Panomsuwan, G.; Bratescu, M.A.; Hashimoto, T.; Teshima, K.; Saito, N. Single-walled carbon nanotubes wrapped by cationic nitrogen-doped carbon for electrocatalytic applications. *ACS Applied Nano Materials* **2020**, *3*, 10183-10189.
  20. Chokradjaroen, C.; Niu, J.; Panomsuwan, G.; Saito, N. Insight on solution plasma in aqueous solution and their application in modification of chitin and chitosan. *Int J Mol Sci* **2021**, *22*.
  21. Hyun, K.; Saito, N. The solution plasma process for heteroatom-carbon nanosheets: The role of precursors. *Sci Rep* **2017**, *7*, 3825.
  22. Morishita, T.; Ueno, T.; Panomsuwan, G.; Hieda, J.; Yoshida, A.; Bratescu, M.A.; Saito, N. Fastest formation routes of nanocarbons in solution plasma processes. *Sci Rep* **2016**, *6*, 36880.
  23. Panomsuwan, G.; Saito, N.; Ishizaki, T. Simple one-step synthesis of fluorine-doped carbon nanoparticles as potential alternative metal-free electrocatalysts for oxygen reduction reaction. *Journal of Materials Chemistry A* **2015**, *3*, 9972-9981.
  24. Panomsuwan, G.; Saito, N.; Ishizaki, T. Nitrogen-doped carbon nanoparticles derived from acrylonitrile plasma for electrochemical oxygen reduction. *Phys Chem Chem Phys* **2015**, *17*, 6227-6232.
  25. Panomsuwan, G.; Saito, N.; Ishizaki, T. From cyano-aromatic molecules to nitrogen-doped carbons by solution plasma for the oxygen reduction reaction in alkaline medium. *Materials Today: Proceedings* **2015**, *2*, 4302-4308.

26. Panomsuwan, G.; Saito, N.; Ishizaki, T. Fe–n-doped carbon-based composite as an efficient and durable electrocatalyst for the oxygen reduction reaction. *RSC Advances* **2016**, *6*, 114553-114559.
27. Panomsuwan, G.; Saito, N.; Ishizaki, T. Electrocatalytic oxygen reduction on nitrogen-doped carbon nanoparticles derived from cyano-aromatic molecules via a solution plasma approach. *Carbon* **2016**, *98*, 411-420.
28. Phan, P.Q.; Chae, S.; Pornaroontham, P.; Muta, Y.; Kim, K.; Wang, X.; Saito, N. In situ synthesis of copper nanoparticles encapsulated by nitrogen-doped graphene at room temperature via solution plasma. *RSC Advances* **2020**, *10*, 36627-36635.
29. Phan, P.Q.; Naraprawatphong, R.; Pornaroontham, P.; Park, J.; Chokradjaroen, C.; Saito, N. N-doped few-layer graphene encapsulated pt-based bimetallic nanoparticles via solution plasma as an efficient oxygen catalyst for the oxygen reduction reaction. *Materials Advances* **2021**, *2*, 322-335.
30. Deokar, G.; Jin, J.; Schwingenschlöggl, U.; Costa, P.M.F.J. Chemical vapor deposition-grown nitrogen-doped graphene's synthesis, characterization and applications. *npj 2D Materials and Applications* **2022**, *6*.
31. Guo, Y.; Zhang, S.; Zhang, R.; Wang, D.; Zhu, D.; Wang, X.; Xiao, D.; Li, N.; Zhao, Y.; Huang, Z., *et al.* Electrochemical nitrate production via nitrogen oxidation with atomically dispersed fe on n-doped carbon nanosheets. *ACS Nano* **2021**.
32. Xue, Y.; Chen, H.; Qu, J.; Dai, L. Nitrogen-doped graphene by ball-milling graphite with melamine for energy conversion and storage. *2D Materials* **2015**, *2*.
33. Li, J.; Chen, M.; Samad, A.; Dong, H.; Ray, A.; Zhang, J.; Jiang, X.; Schwingenschlogl, U.; Domke, J.; Chen, C., *et al.* Wafer-scale single-crystal monolayer graphene grown on sapphire substrate. *Nat Mater* **2022**, *21*, 740-747.
34. Saito, N.; Bratescu, M.A.; Hashimi, K. Solution plasma: A new reaction field for nanomaterials synthesis. *Japanese Journal of Applied Physics* **2018**, *57*.
35. Takai, O. Solution plasma processing (spp). *Pure and Applied Chemistry* **2008**, *80*, 2003-2011.

36. Chokradjaroen, C.; Wang, X.; Niu, J.; Fan, T.; Saito, N. Fundamentals of solution plasma for advanced materials synthesis. *Materials Today Advances* **2022**, *14*.
37. Niu, J.; Chokradjaroen, C.; Saito, N. Graphitic n-doped graphene via solution plasma with a single dielectric barrier. *Carbon* **2022**, *199*, 347-356.
38. Niu, J.; Chokradjaroen, C.; Sawada, Y.; Wang, X.; Saito, N. Plasma–solution junction for the formation of carbon material. *Coatings* **2022**, *12*.
39. Xu, S.; Chansai, S.; Stere, C.; Inceesungvorn, B.; Goguet, A.; Wangkawong, K.; Taylor, S.F.R.; Al-Janabi, N.; Hardacre, C.; Martin, P.A., *et al.* Sustaining metal–organic frameworks for water–gas shift catalysis by non-thermal plasma. *Nature Catalysis* **2019**, *2*, 142-148.
40. Fan, L.S.; Constantin, L.; Li, D.W.; Liu, L.; Keramatnejad, K.; Azina, C.; Huang, X.; Golgir, H.R.; Lu, Y.; Ahmadi, Z., *et al.* Ultraviolet laser photolysis of hydrocarbons for nondiamond carbon suppression in chemical vapor deposition of diamond films. *Light Sci Appl* **2018**, *7*, 17177.
41. Bratescu, M.A.; Cho, S.-P.; Takai, O.; Saito, N. Size-controlled gold nanoparticles synthesized in solution plasma. *The Journal of Physical Chemistry C* **2011**, *115*, 24569-24576.
42. Bratescu, M.A.; Kim, K.; Saito, N. Quantitative spectrochemical analysis of solution plasma in aromatic molecules. *Plasma Processes and Polymers* **2019**, *16*.
43. Baroch, P.; Potocky, S.; Saito, N. Generation of plasmas in water: Utilization of a high-frequency, low-voltage bipolar pulse power supply with impedance control. *Plasma Sources Science and Technology* **2011**, *20*.
44. Baroch, P.; Saito, N.; Takai, O. Special type of plasma dielectric barrier discharge reactor for direct ozonization of water and degradation of organic pollution. *Journal of Physics D: Applied Physics* **2008**, *41*.
45. Bratescu, M.A.; Saito, N.; Takai, O. Redox reactions in liquid plasma during iron oxide and oxide-hydroxide nanoparticles synthesis. *Current Applied Physics* **2011**, *11*, S30-S34.
46. Kang, J.; Li, O.L.; Saito, N. A simple synthesis method for nano-metal catalyst supported on mesoporous carbon: The solution plasma process. *Nanoscale* **2013**, *5*, 6874-6882.

47. Kang, J.; Li, O.L.; Saito, N. Synthesis of structure-controlled carbon nano spheres by solution plasma process. *Carbon* **2013**, *60*, 292-298.
48. Kim, D.W.; Li, O.L.; Saito, N. Enhancement of orr catalytic activity by multiple heteroatom-doped carbon materials. *Phys Chem Chem Phys* **2015**, *17*, 407-413.
49. Zhang, G.; Zhu, J.; Zeng, W.; Hou, S.; Gong, F.; Li, F.; Li, C.C.; Duan, H. Tin quantum dots embedded in nitrogen-doped carbon nanofibers as excellent anode for lithium-ion batteries. *Nano Energy* **2014**, *9*, 61-70.
50. Lux, S.F.; Placke, T.; Engelhardt, C.; Nowak, S.; Bieker, P.; Wirth, K.E.; Passerini, S.; Winter, M.; Meyer, H.W. Enhanced electrochemical performance of graphite anodes for lithium-ion batteries by dry coating with hydrophobic fumed silica. *Journal of The Electrochemical Society* **2012**, *159*, A1849-A1855.

## ***Chapter 3***

***Chemical Intermediates Produced by Solution  
Plasma in Cyclic Organic Compounds and the  
Structural Correlation with the Raw Molecules***

## ***Chapter 3 - Chemical Intermediates Produced by Solution Plasma in Cyclic Organic Compounds and the Structural Correlation with the Raw Molecules***

### **3.1 Introduction**

The correlation obtained in Chapter 2 showed that, in plasma phase, the  $\text{CN}^*$  radicals played an important role in influencing the amount of nitrogen content in the carbon products. However, the spectra from the OES measurement can provide information relating to only chemical species which exist at the center of the plasma. Nevertheless, the chemical species presenting at the interface between plasma and liquid as well as in solution, are also non-negligible. To truly understand the chemical reaction through solution plasma (SP), the investigation of chemical species at the interface between plasma and liquid as well as in solution is strongly recommended.

In the reaction field of the solution plasma, the interface between plasma and liquid has been believed to be a major reaction field. The solution can act as an electrode [1-3]. Since electrons have a smaller mass compared to ions, the effect of its drift-diffusion is more significant [4]. The electron can rapidly diffuse to the interface and solution, while the heavy particles, *i.e.*, ions, are retained in the plasma and seemed to be at their original position, compared to the motion of electrons. Accordingly, in the plasma, the layer of positively charged particles ( $\text{CN}^+$ ,  $\text{C}_2^+$ ,  $\text{H}^+$ , *etc.*), *i.e.*, a sheath layer, is formed [5-8]. The built-in electric field formed by the motion of ions and electrons in the sheath layer drives the positively charged particles to move at an accelerated velocity and cause collisions with solution molecules [5]. The collision process results in the excitation, ionization, or decomposition of the solution molecules and contributes secondary electrons to the plasma [9-13]. The above process is



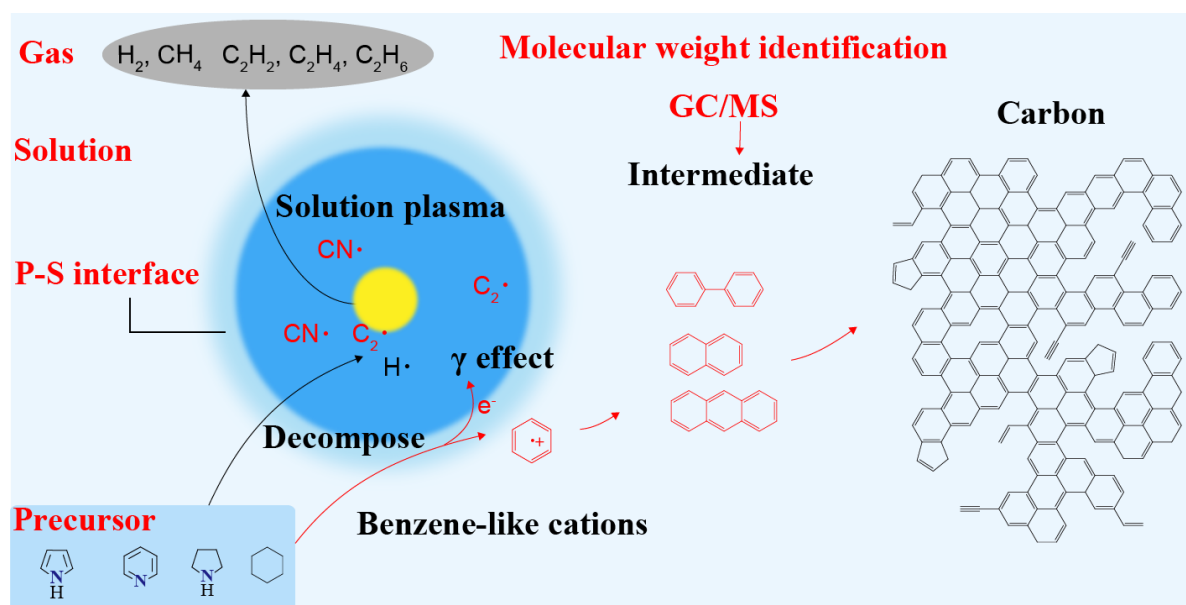
exactly the  $\gamma$  effect in the classical Townsend discharge theory [14]. Numerous chemical intermediate species are generated by collisions at the plasma-liquid interface and further undergo oligomerization and polymerization reactions to form the final carbon products [1,15,16]. Therefore, the characterization of chemically active species in the solution can perceive the relationship between the intermediate product properties and final carbon products and support to the proposal of a more reliable and intuitive reaction route for carbon product generation in the SP reaction field. It will be the essential evidence for the realization of high N-containing carbons synthesis.

2016, Morishita *et al.* explored the reaction pathways for the preparation of nitrogen-free carbon products from chain alkanes (hexane, hexadecane), cyclic alkanes (cyclohexane), and cyclic aromatic hydrocarbons (benzene) as raw materials in a solution plasma reaction field [1]. They found that saturated alkanes had lower carbon product yields and formed the final carbon product through a carbonization process in the plasma phase. Aromatic hydrocarbons had higher carbon product yields, and the final carbon products were formed through a polymerization process in the liquid phase. The two different reaction fields provided a reasonable explanation for the different crystallinity characteristics of the final carbon products. However, the study lacked the exploration of reaction routes for raw materials, including heteroatoms.

2018, Kyusung Kim *et al.* explained the reaction pathway of the SP reaction field using pyridine as a raw material [16]. They found that pyridine sequentially formed intermediates with a larger molecular mass of two rings (bipyridine, phenanthroline), and three rings (terpyridine) by polymerization. However, this study did not address the question of how the intermediates affect the structural parameters of the final carbon products. In other words, it is of great importance to discover more general patterns about the intermediates in the complex SP reaction field, which can guide scientists to obtain high N-containing carbons.

To address this issue, in this Chapter, the chemical intermediates generated in the SP reaction field were analyzed using gas chromatography-mass spectrometry (GC/MS). The 53 cyclic molecules containing one to more N atoms identified previously were used as raw materials for the SP reaction field, as shown in **Figure 3.1**. The influence of the intermediate species on the structural parameters

of the final carbon product was explored intensively, and the correlation from the raw material, bridging with the intermediate species, to the final carbon product was finally proposed, where different raw materials may have different reaction routes for the expected carbon products.

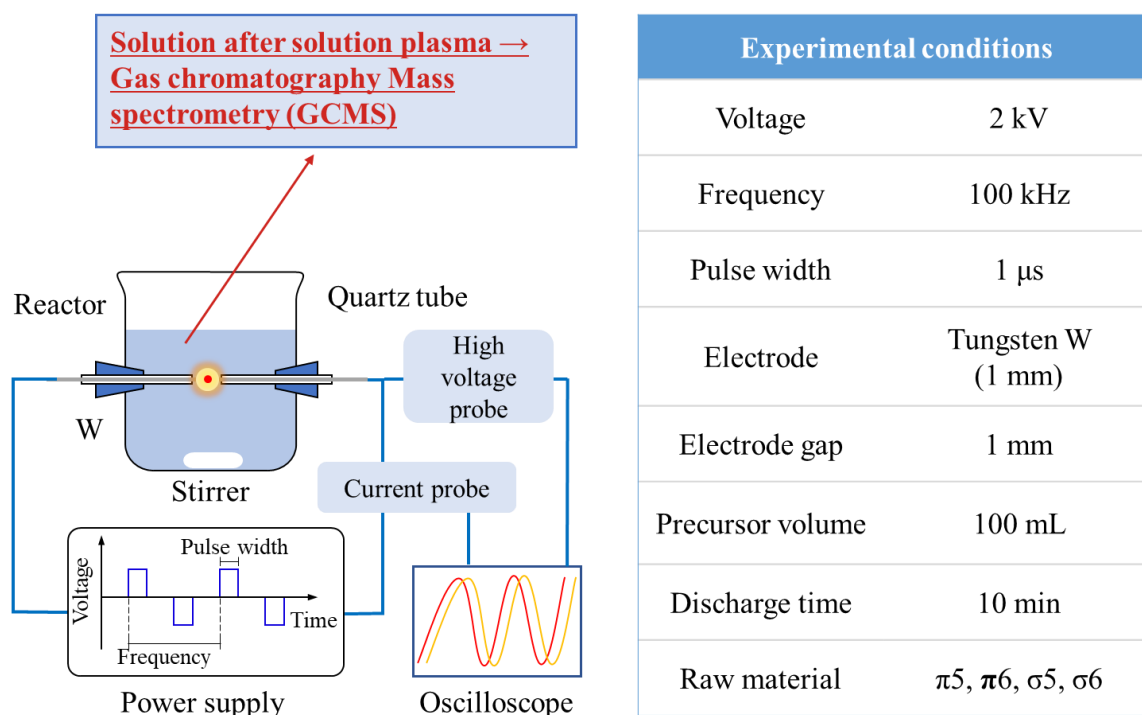


**Figure 3.1.** Schematic diagram of the chemical intermediate species in solution plasma characterized by GC/MS based on molecular weight identification.

### 3.2 Experimental procedures

**Plasma diagnosing and GC/MS characterization.** In this Chapter, the typical pin-to-pin electrode and experimental conditions, the same as in chapter 2, were applied for plasma producing, as shown in **Figure 3.2**. The discharge environment was the confirmed 53 types of raw material, which including  $\sigma$ 5-,  $\pi$ 5-,  $\sigma$ 6-,  $\pi$ 6-. The discharge power source was bipolar pulses. The carbon products obtaining process was consistent with chapter 2. 1  $\mu$ L of the solution containing the intermediate products, after ten seconds discharge, were syringed by the spitless injection into 30-m HP-5 column (Agilent Technologies 19091J-413) with the carrier gas, which was Helium (2 mL/min of flow rate). The instrument was equipped at the platform of GC/MS (JEOL JMS-Q1050GC). The temperature ramp rate of GC column was set at 5  $^{\circ}$ C/min, until 300  $^{\circ}$ C. The range of the mass-to-charge ratio of mass spectrometry was set from 20 to 600 m/z.

**Carbon products characterization.** The methods of characterization of carbon products were the same as in chapter 2. It includes the crystallinity of carbon conducted through X-ray diffraction (XRD, Smartlab, Rigaku Co., Japan) with a Cu K $\alpha$  ( $\lambda = 0.154$  nm) X-rays source. The index of defect of carbon was conducted by Raman spectra microscope (Raman, Leica DM 2500M Ren (RL/TL), Renishaw Plc, England) utilizing a laser wavelength of 532.5 nm. The N content of carbon was conducted by Elemental analysis (EA) with Perkin Elmer 2400 Series II CHNS/O analyzer.



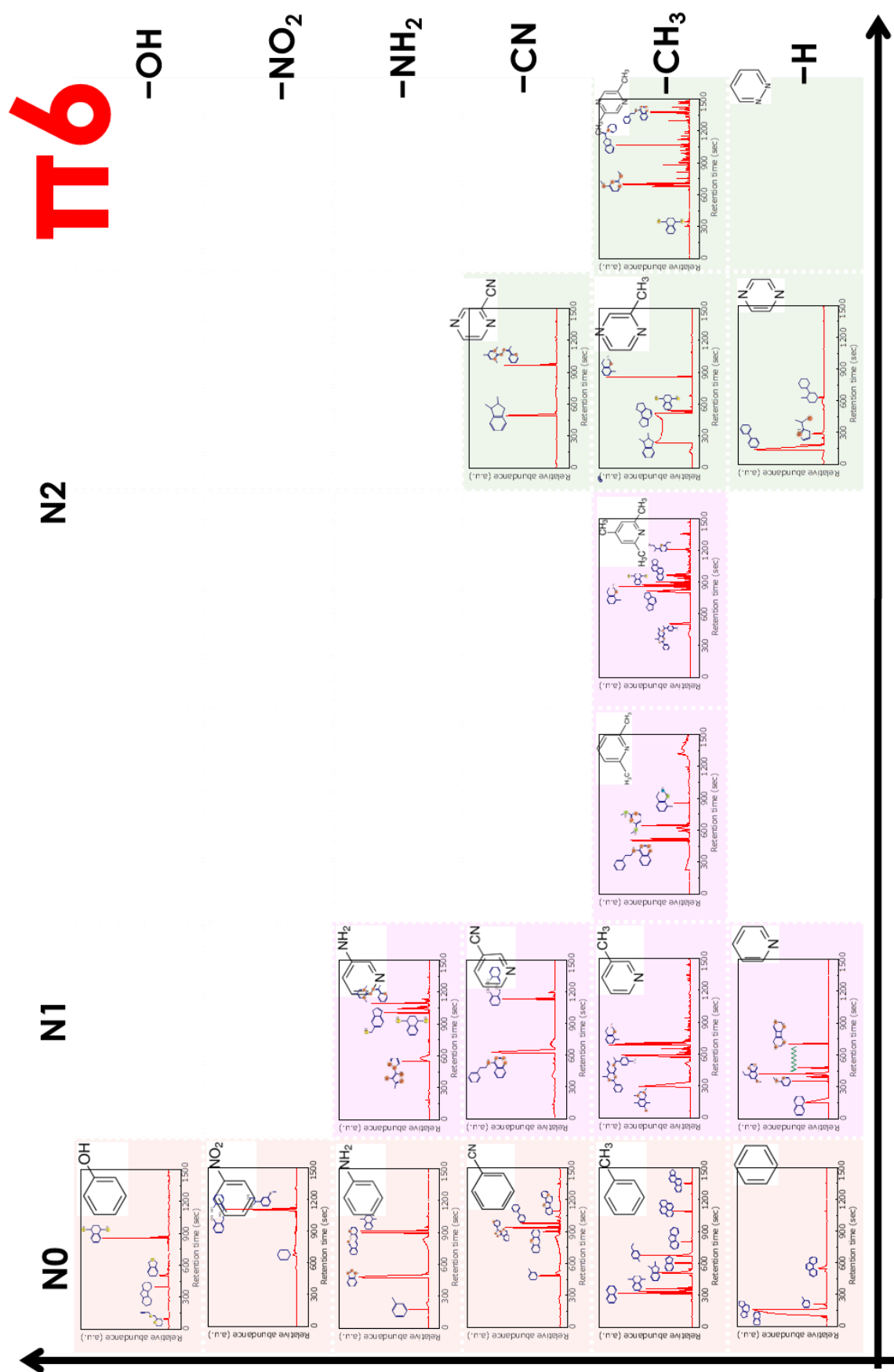
**Figure 3.2.** Schematic image of the experiment setup and the exact experimental conditions, including the parameters of power sources, electrode configuration and discharge time.

### 3.3 Results and discussion

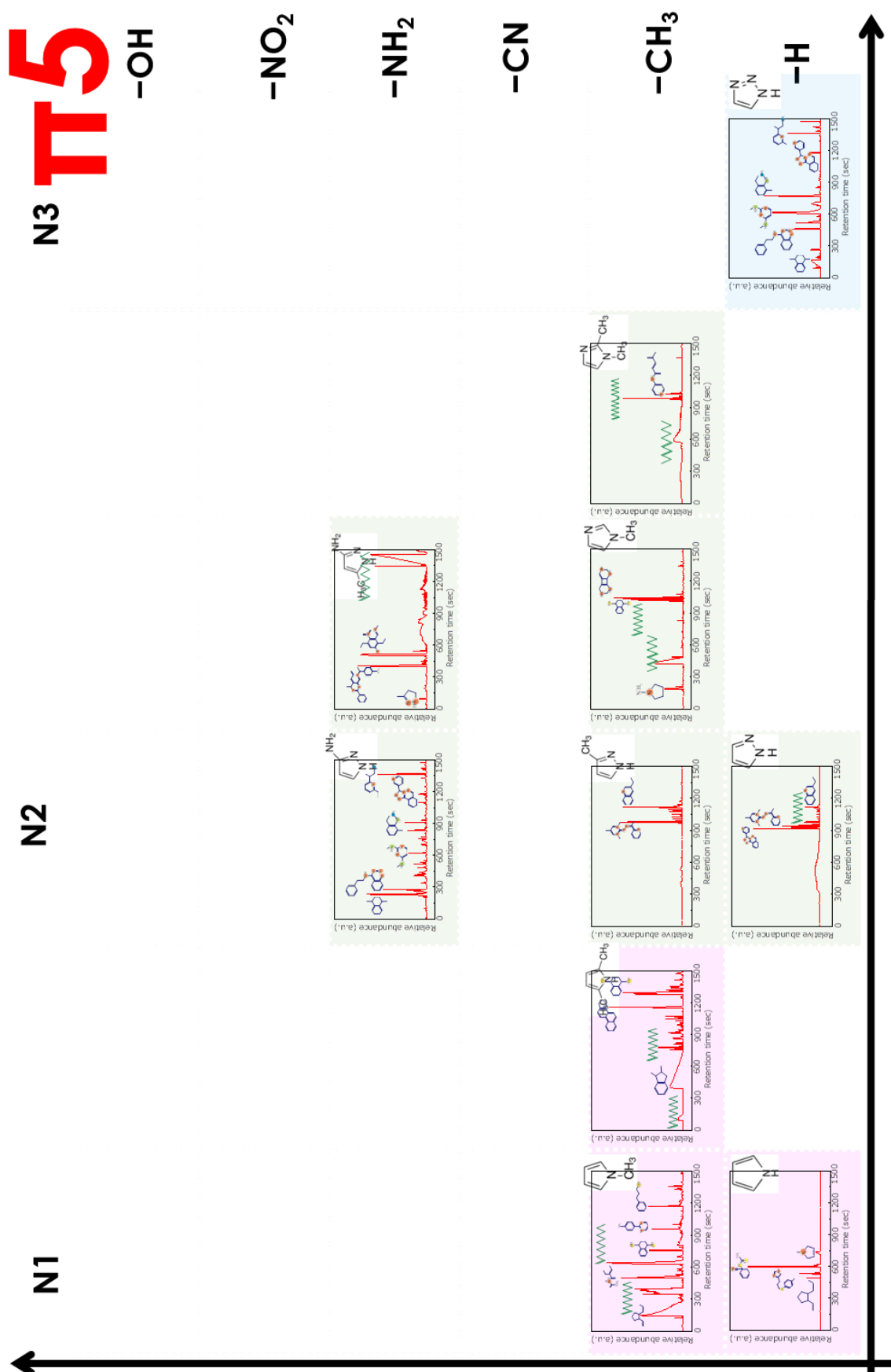
**Figure 3.3–3.6** show the results of GC/MS qualitative analysis of the intermediate species in SP reaction filed from the raw material of  $\sigma$ 5-,  $\pi$ 5-,  $\sigma$ 6-,  $\pi$ 6-, respectively. The results showed that in the case of aromatic cyclic molecules without N ( $\pi$ 6-,  $\pi$ 5-) used as raw material, most of the intermediate products were found to be unsaturated aromatic molecules with two, three, or four rings (detailed molecular structures with categorized by the number of C are shown in **Figure 3.8**) and no chain-like

molecules partially existed. In the case of aromatic cyclic molecules with N ( $\pi 6-$ ,  $\pi 5-$ ) used as raw materials, the intermediate products were dominated by monocyclic to polycyclic molecules (detailed molecular structures categorized by the number of C are shown in **Figure 3.7**) with N atoms hybridized by participating in  $\pi$ -bonds configuration of the aromatic ring structure. The N bonding configuration included pyridinic N, graphitic N, and pyrrolic N [17]. There were also molecules with N atoms which presented as functional groups attached to the aromatic ring. The obtained analysis result indicated that when the aromatic ring molecules ( $\pi 6-$ ,  $\pi 5-$ ) were used as raw materials in the SP reaction field, it could suggest that the final carbon products were produced through the polymerization process after it underwent the excitation process of ring-like intermediates as the elemental fragments. It is also important to mention that within the group of  $\pi 6-$  and  $\pi 5-$  molecules, as the functional group activity increased, there was no regular change in the number or intensity of intermediate chemical species from GC/MS. This means that the changes in the species and quantity of chemical intermediates in the complex reaction field of SP do not follow the classification based on the general rules of molecular chemical activity.

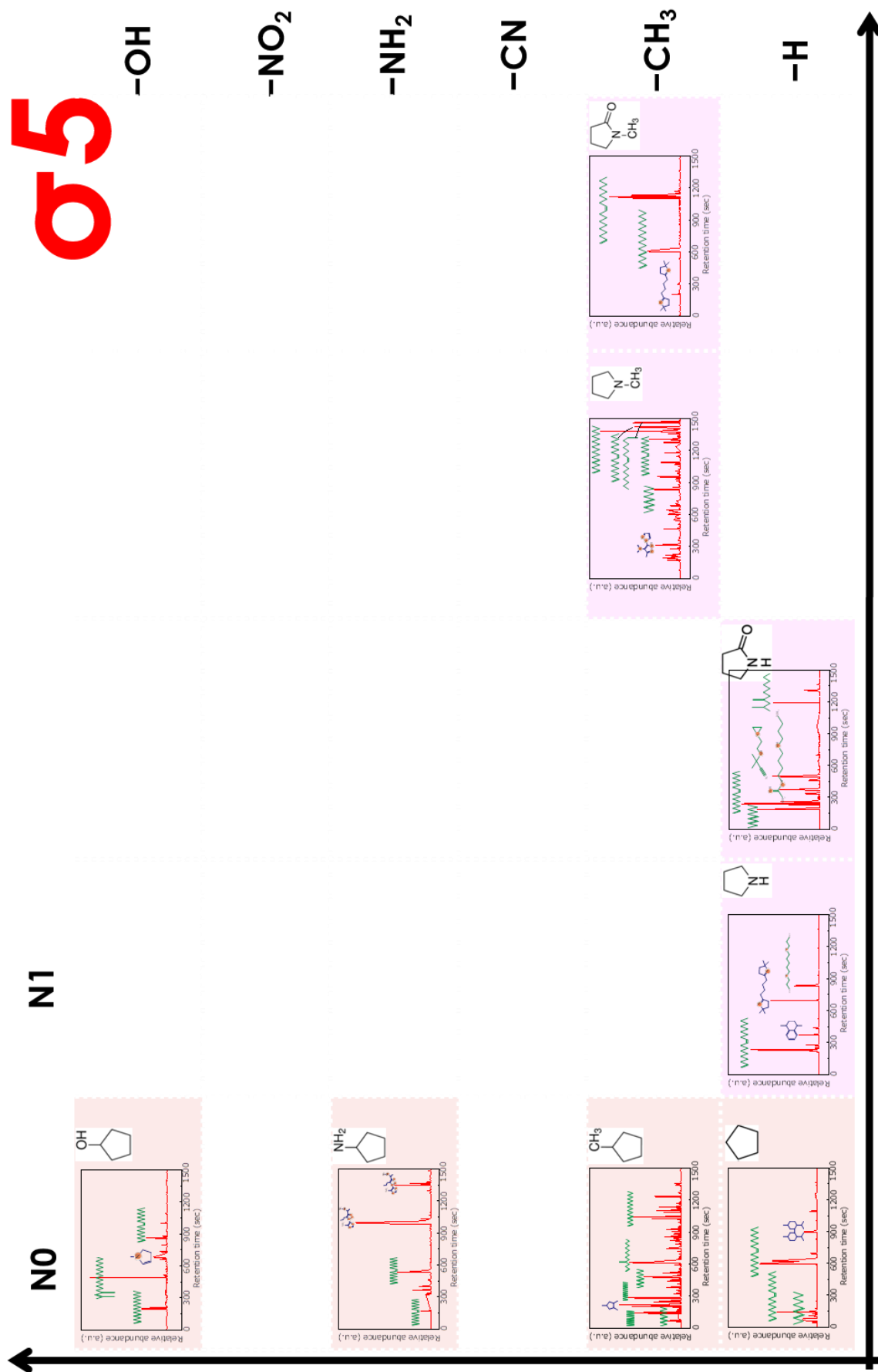
In the SP reaction field with saturated cyclic molecules ( $\sigma 5-$ ,  $\sigma 6-$ ) used as the raw material, the intermediate products were mainly long-chain molecules (the detailed molecular structures categorized by the number of C are shown in **Figure 3.9**) and contained slightly amount of N atoms. This indicates that the raw material molecules ( $\sigma 5-$ ,  $\sigma 6-$ ) were decomposed into short-chain hydrocarbon molecules at the plasma-liquid interface sites. This might be because a single bond had low bond energy than that of the double bond, and thus the raw material molecules of  $\sigma 5$  and  $\sigma 6$  groups were more easily decomposed but not only excited under the  $\gamma$  effect from ions. The decomposed short-chain molecules further formed long-chain molecules through electron transfer reactions. The above results indicated that the raw materials of saturated cyclic molecules ( $\sigma 5-$ ,  $\sigma 6-$ ) undergo excitation and decomposition in the SP reaction field to produce the final carbon products through the polymerization process of chain-like intermediates as the elemental fragments.



**Figure 3.3.** GC/MS qualitative analysis of the intermediates in the SP reaction filed corresponding to the raw materials of  $\pi 6$ .



**Figure 3.4.** GC/MS qualitative analysis of the intermediates in the SP reaction filed corresponding to the raw materials of  $\pi 5$ -.



**Figure 3.5.** GC/MS qualitative analysis of the intermediates in the SP reaction filed corresponding to the raw materials of σ5.

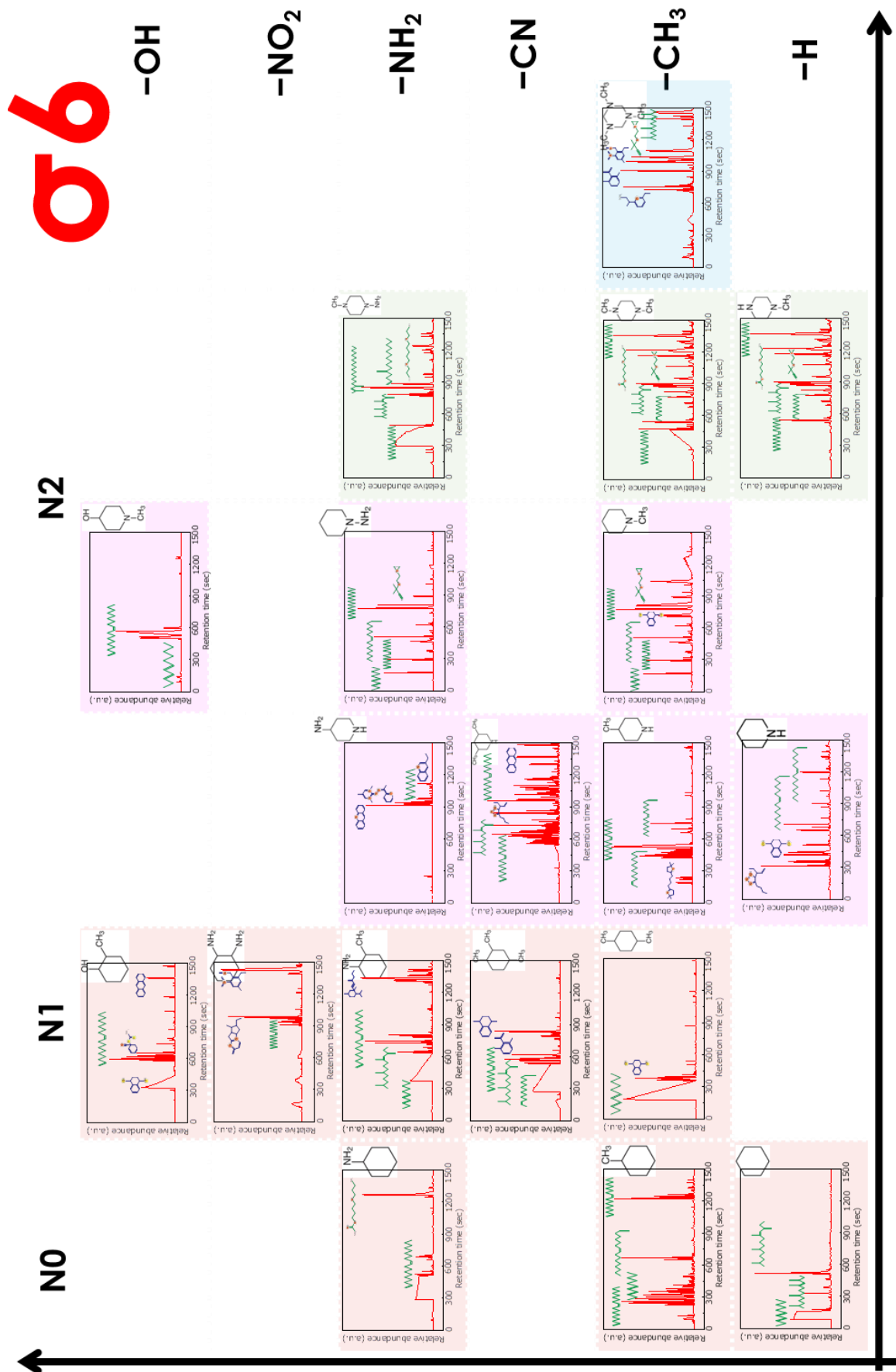

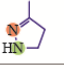
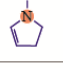




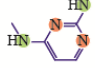
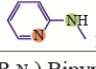
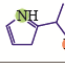
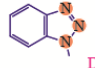
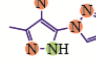
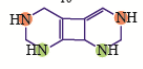
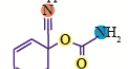
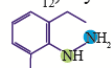
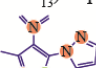
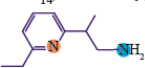
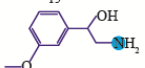
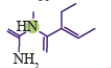
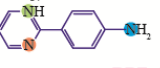
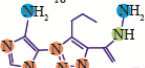
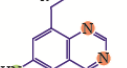
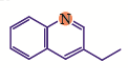
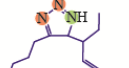
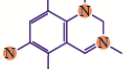
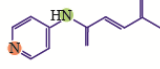
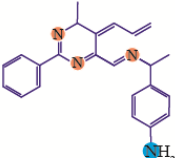
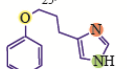
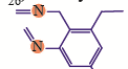
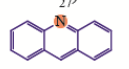
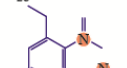
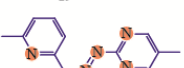
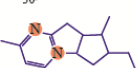
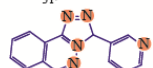
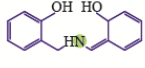
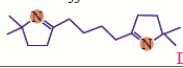
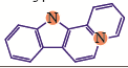
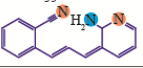
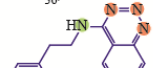
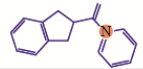


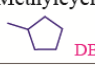
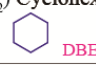
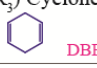
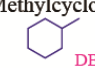
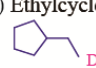

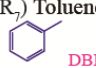

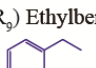
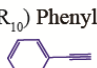
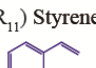
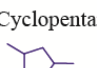
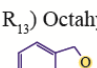
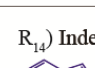


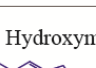

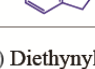


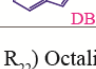
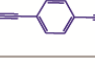
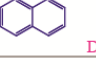
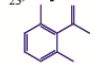
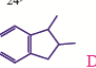



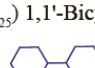
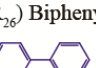
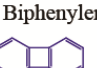
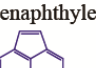


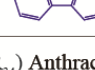
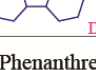
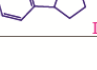
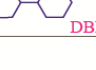
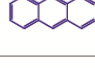

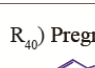
Figure 3.6. GC/MS qualitative analysis of the intermediates in the SP reaction filed corresponding to the raw materials of  $\sigma_6$ .



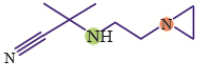
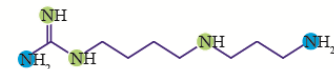



















C numbers	Moleculat name and structure				
			The pink color of umnber is Double Bond Equivalent (DBE)		
C4	R-N <sub>1</sub> ) Pyrrolidinamine  DBE=1	R-N <sub>2</sub> ) Pyrazole  DBE=2			
C5	R-N <sub>3</sub> ) H-Pyrrole  DBE=2	R-N <sub>4</sub> ) Pyrrole  DBE=2	Over the aromatic ring  On the aromatic ring  In the aromatic ring 		
C6	R-N <sub>5</sub> ) Pyrimidine  DBE=4	R-N <sub>6</sub> ) Pyridinamine  DBE=4			R-N <sub>7</sub> ) Proline  DBE=3
C7	R-N <sub>8</sub> ) Benzotriazole  DBE=6	R-N <sub>9</sub> ) Bipyrazolyl  DBE=6			
C8	R-N <sub>10</sub> ) Cyclobuta  DBE=5	R-N <sub>11</sub> ) Carbamate  DBE=6			
C9	R-N <sub>12</sub> ) Hydrazine  DBE=4	R-N <sub>13</sub> ) Bipyrazolyl  DBE=8	R-N <sub>14</sub> ) Methoxypheny  DBE=4	R-N <sub>15</sub> ) Methoxyphenyl  DBE=4	
C10	R-N <sub>16</sub> ) Butenamide  DBE=3	R-N <sub>17</sub> ) Benzenamine  DBE=8	R-N <sub>18</sub> ) Carboxylic  DBE=7		
C11	R-N <sub>19</sub> ) Dimethoxy  DBE=7	R-N <sub>20</sub> ) Tetrahydroquinoline  DBE=7	R-N <sub>21</sub> ) Triazole-4-carboxylic  DBE=4		
C12	R-N <sub>22</sub> ) Dinitrobenzaldehyde  DBE=6	R-N <sub>23</sub> ) Pyridin-4-ylcarbamoyl  DBE=7	C23 R-N <sub>24</sub> ) Hydrazone  DBE=14		
C13	R-N <sub>25</sub> ) Limidazole  DBE=7	R-N <sub>26</sub> ) Phenylmethyl cyanide  DBE=6	R-N <sub>27</sub> ) Acridine  DBE=10		
C14	R-N <sub>28</sub> ) Dinitrobenzaldehyde  DBE=6	R-N <sub>29</sub> ) Pyridylethanone  DBE=9	R-N <sub>30</sub> ) H-Furo-oxazol  DBE=6	R-N <sub>31</sub> ) Phthalazine  DBE=13	
				R-N <sub>32</sub> ) Hydroxybenzyl  DBE=8	
C15	R-N <sub>33</sub> ) Hexanedioic  DBE=4	R-N <sub>34</sub> ) Octahydroindolo  DBE=12	R-N <sub>35</sub> ) Cyanobenzyl  DBE=11	R-N <sub>36</sub> ) Benzo-triazine  DBE=11	
C16	R-N <sub>37</sub> ) Methanone  DBE=10				

**Figure 3.7.** The ring structures with N containing the intermediate products obtained from the SP reaction field in the discharge environment of different raw materials. The carbon numbers of each chemical species were from C4 to C23, and the corresponding double bond equivalent was calculated.

Chapter 3 - Chemical Intermediates Produced by Solution Plasma in Cyclic Organic Compounds and the Structural Correlation with the Raw Molecules

C numbers	Molecular name and structure		The pink color of number is Double Bond Equivalent (DBE)			
C6	R <sub>1</sub> ) Methylcyclopentane  DBE=1	R <sub>2</sub> ) Cyclohexane  DBE=1	R <sub>3</sub> ) Cyclohexadiene  DBE=3			
C7	R <sub>4</sub> ) Methylcyclohexane  DBE=1	R <sub>5</sub> ) Ethylcyclohexane  DBE=1	R <sub>6</sub> ) Norbornane  DBE=2	R <sub>7</sub> ) Toluene  DBE=4		
C8	R <sub>8</sub> ) Ethylcyclohexane  DBE=2	R <sub>9</sub> ) Ethylbenzene  DBE=4	R <sub>10</sub> ) Phenylethyne  DBE=6	R <sub>11</sub> ) Styrene  DBE=5	R <sub>12</sub> ) Cyclopentanetriol  DBE=1	R <sub>13</sub> ) Octahydro  DBE=5
C9	R <sub>14</sub> ) Indene  DBE=6	R <sub>15</sub> ) Tetrahydro  DBE=3	R <sub>16</sub> ) Methylbenzene  DBE=4	R <sub>17</sub> ) Hydroxymethyl  DBE=6	R <sub>18</sub> ) Propanol  DBE=4	
C10	R <sub>19</sub> ) Diethynylbenzene  DBE=8	R <sub>20</sub> ) Naphthalene  DBE=8	R <sub>21</sub> ) Vinylcyclopentene  DBE=3	R <sub>22</sub> ) Octalin  DBE=5		
C11	R <sub>23</sub> ) Cyclohexen  DBE=5	R <sub>24</sub> ) Indene  DBE=5				
C12	R <sub>25</sub> ) 1,1'-Bicyclohexyl  DBE=2	R <sub>26</sub> ) Biphenyl  DBE=8	R <sub>27</sub> ) Biphenylene  DBE=9	R <sub>28</sub> ) Acenaphthylene  DBE=9	R <sub>29</sub> ) Hexahydro-as-indacene  DBE=6	
C13	R <sub>30</sub> ) Fluorene  DBE=9	R <sub>31</sub> ) Dodecahydro  DBE=3	R <sub>32</sub> ) Tricyclo  DBE=6	R <sub>33</sub> ) Bicyclohexyl  DBE=2		
C14	R <sub>34</sub> ) Anthracene  DBE=10	R <sub>35</sub> ) Phenanthrene  DBE=10				
C16	R <sub>36</sub> ) Naphthalene  DBE=11	R <sub>37</sub> ) Pyrene  DBE=12	R <sub>38</sub> ) Fluoranthene  DBE=12	R <sub>39</sub> ) Bis-Benzene  DBE=12		
C17	R <sub>40</sub> ) Pregnane  DBE=11					
C18	R <sub>41</sub> ) Propiolic  DBE=4					
C20	R <sub>42</sub> ) Menthane  DBE=2					

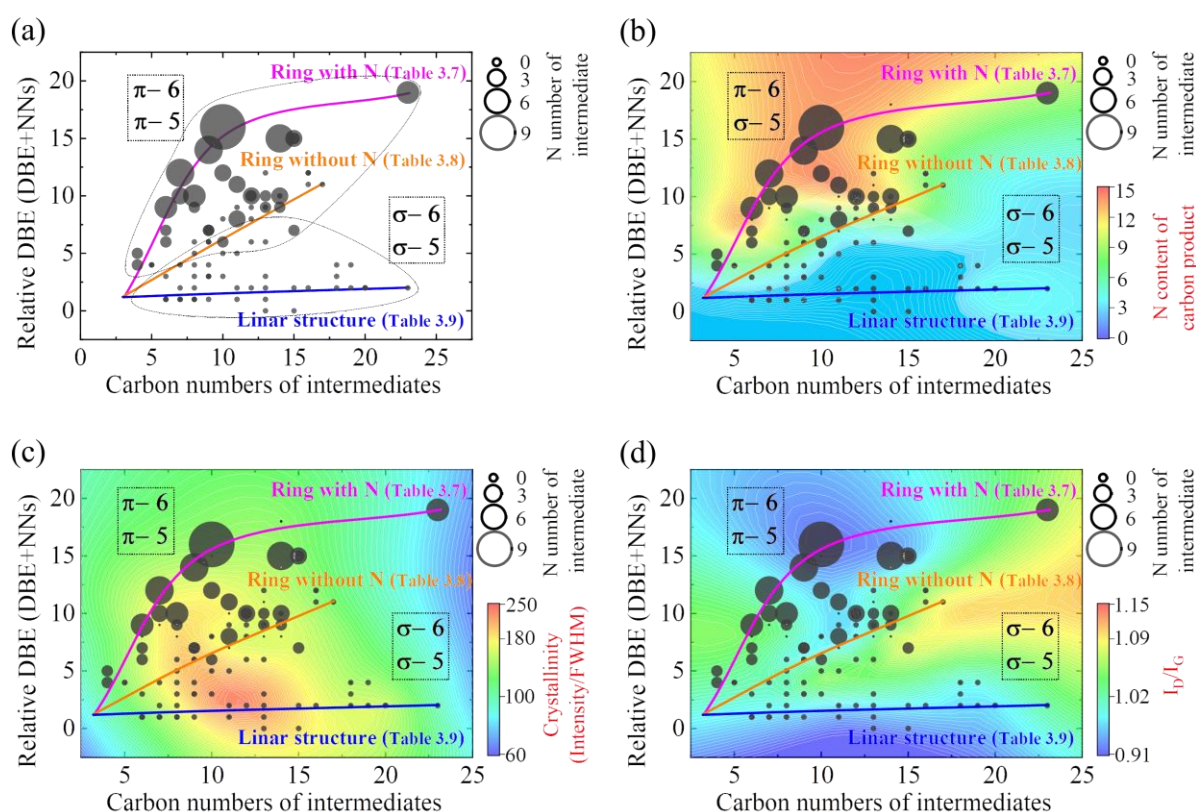
**Figure 3.8.** The ring structures without N contain the intermediate products obtained from the SP reaction field in the discharge environment of different raw materials. The carbon numbers of each chemical species were from C6 to C20, and the corresponding double bond equivalent was calculated.

C numbers	Moleculat name and structure	The pink color of unumber is Double Bond Equivalent (DBE)	
C8	L <sub>1</sub> ) Aziridyl]ethylamino]isobutyronitrile 	L <sub>2</sub> ) N-8-Guanidino-spermidine 	
C9	L <sub>2</sub> ) Triazaundecane 	L <sub>4</sub> ) 1-Nonene 	<div style="border: 1px solid black; padding: 5px;">                 Over the aromatic ring                    On the aromatic ring                    In the aromatic ring   </div>
C11	L <sub>2</sub> ) Decadien 	L <sub>6</sub> ) 1-Undecene 	
C13	L <sub>7</sub> ) Hexyl isovalerate 	L <sub>8</sub> ) Decane 	
C15	L <sub>9</sub> ) Tetradecenal 	L <sub>10</sub> ) Dodecane 	
C16	L <sub>11</sub> ) Hexadecenal 	L <sub>12</sub> ) Allyl nonyl ester 	
C18	L <sub>13</sub> ) Trimethyldodec 	L <sub>14</sub> ) Trimethyldodec 	
C19	L <sub>15</sub> ) Octadecenal 	L <sub>16</sub> ) Cyclopropaneoctanal 	
	L <sub>17</sub> ) Nonadecatetraene 		
C23	L <sub>18</sub> ) Butenoic 		

**Figure 3.9.** The linear structures of the intermediate products obtained from the SP reaction field in the discharge environment of different raw materials. The carbon numbers of each chemical species were changed from C8 to C23, and the corresponding double bond equivalent was calculated.

According to the obtained results in the above summary, the different structures of intermediates produced by solution plasma formed from different raw materials and be identified. Statistical analysis was demonstrated to make the correlation between raw materials and intermediates. The carbon numbers of each intermediate were calculated and counted. Double bond equivalents (DBE) refer to the level of unsaturation of covalent bonds within an organic molecule or the number of unsaturated bonds present [17-19]. For example, benzene has three double bonds and one ring, and thus the DBE of benzene is four. Moreover, the triple bond is considered to have a DBE of two. The detailed formula is  $DBE=C-H/2+N/2+1$ , where C is the number of carbon atoms, H is the number of hydrogen atoms, and N is the number of nitrogen atoms [17,20]. Accordingly, the double bond equivalents of each intermediate were calculated and labeled in **Figures 3.7-3.9**.

The relative double bond equivalents, *i.e.*, DBE+N, were calculated and applied to distinguish between intermediates containing or not containing N atoms. **Figure 3.10(a)** shows the iso-abundance plots of DBE+N versus carbon numbers for all intermediates. Meanwhile, the number of nitrogen atoms for each different intermediate was showed the bubble diagram format. As the number of carbons of the intermediates increased, the DBE+N of the ring intermediates with N also showed an increasing trend, and the rate of the increase became faster compared to the other two structures. In addition, the number of N atoms also tended to increase with the increase in the number of carbon atoms. For the linear structure intermediates, the DBE+N did not show a significant change with the increase in the number of carbon atoms. Since linear intermediates mostly existed as C–C single bonds. To clarify the correlation between intermediates and carbon products, the dominant intermediate produced in the SP reaction field from each raw material (as shown in **Table 3.1**) was chosen as a representative to correspond to the structural parameters of the carbon products. As shown in **Figure 3.10**, the intermediates generated in the SP reaction field with  $\pi 6$ - and  $\pi 5$ - as raw materials had higher DBE, even though they had the same number of carbons compared to  $\sigma 6$ - and  $\sigma 5$ - as raw materials.



**Figure 3.10.** (a) The iso-abundance plots of relative double bond equivalent (DBE) with nitrogen numbers (NNs) vs carbon numbers for the class of nitrogen numbers (NNs) of intermediates; The iso-abundance plots of relative double bond equivalent (DBE) with nitrogen numbers (NNs) vs carbon numbers for the class of nitrogen numbers (NNs) of intermediates and (b) N content of carbon products, (c) crystallinity from intensity/FWHM of C002 peak from XRD, (d) defect index calculated by  $I_D/I_G$  from Raman characterization.

The structural parameters of the carbon products in the fourth coordinates of **Figure 3.10(a)** and showed the correlation between the intermediates and the carbon products by using the fitted pseudo-color plot, as shown in **Figure 3.10(b)-(d)**. From the distribution of the N content of carbon products (**Figure 3.10 (b)**), the ring intermediate with nitrogen induced the carbon products with higher N content. Moreover, the higher content of nitrogen in the intermediate products was also found to result in the higher nitrogen content of the carbon products. This evidence also supported that the generation of carbon products in the SP reaction field was related to the polymerization process of intermediates

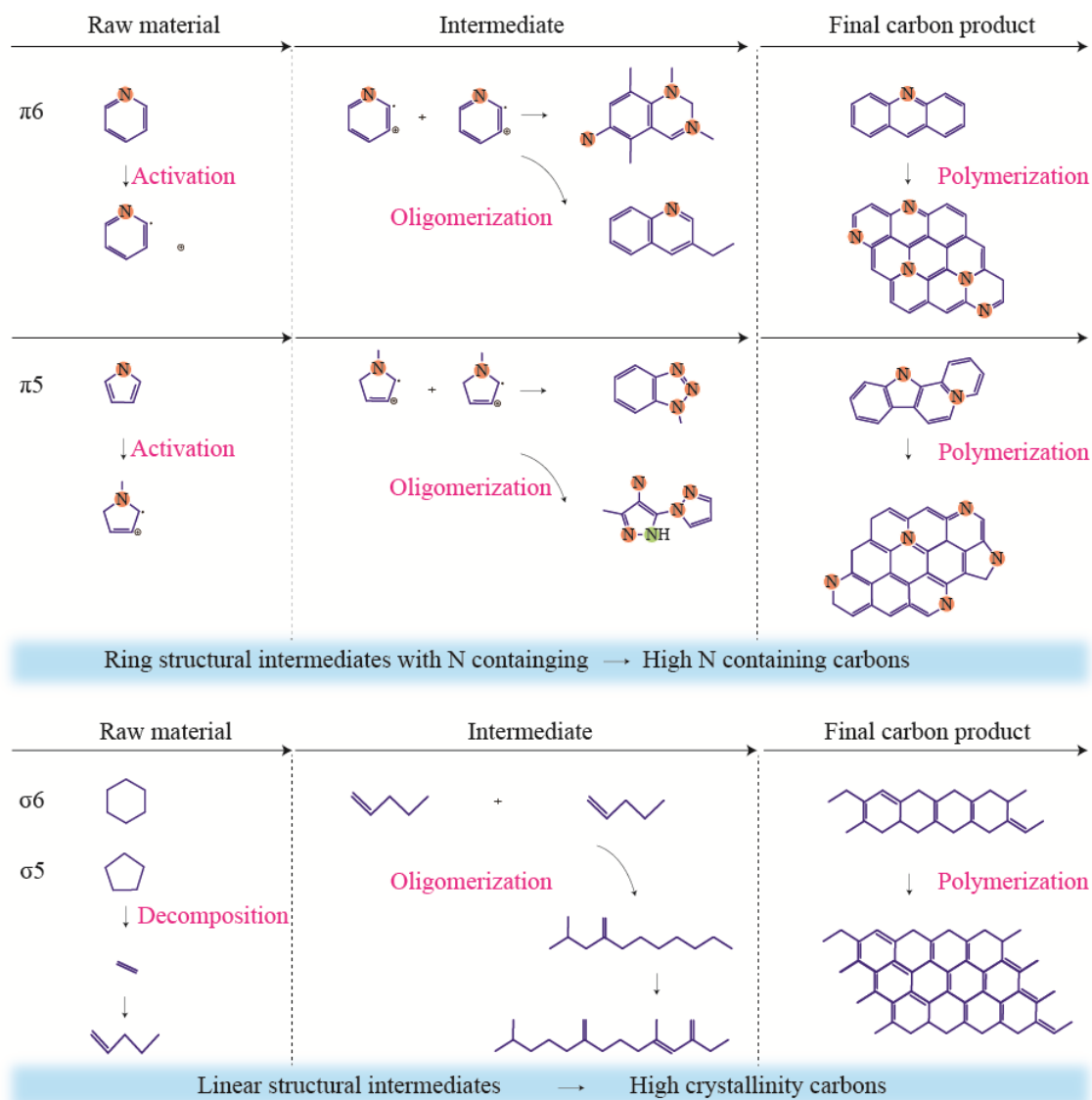
within the solution. **Figure 3.10(c)** shows the degree of crystallinity of the carbon products in relation to the intermediates as well as the raw materials. We can see that the intermediates with linear molecular structure produced by  $\sigma_6$ -,  $\sigma_5$ - as raw materials in the SP reaction field could contribute to the formation of carbon materials with high crystallinity. This might be due to the absence of N atoms in the carbon chain structure, which promoted the formation of linear chain alkanes and thus ensured that the carbon framework did not suffer from bending and distortion during the polymerization process. **Figure 3.10(d)** shows the correlation between the molecular vibration, *i.e.*,  $I_D/I_G$ , which can indicate the structural properties of carbon products and the chemical structure of intermediates. It was found that the carbon products produced with the intermediates of the linear structure had lower  $I_D/I_G$  values, which was due to the higher crystallinity of the product. However, the carbon products with higher N content, *i.e.*, the intermediates of the ring with N, also had lower  $I_D/I_G$  values. It might be due to the introduction of N atoms into the carbon framework in the form of graphitic, pyridinic, or pyrrolic could not cause significant damage to the electronic surface potential [21-23].

**Table 3.1.** The number of the intermediate representing each raw material, the corresponding carbon number, double bond equivalent, and N number of the intermediate.

Name	Inte	C	DBE	N	Name	Inte	C	DBE	N
Benzene	R <sub>20</sub>	10	8	0	Methyl cyclopentane	R <sub>12</sub>	8	1	0
Toluene	R <sub>20</sub>	10	8	0	Cycloheptylamine	RN <sub>18</sub>	10	7	8
Benzonitrile	RN <sub>31</sub>	14	13	5	Cyclopentanol	L <sub>18</sub>	23	2	0
Aniline	RN <sub>8</sub>	7	6	3	Pyrrolidine	L <sub>16</sub>	19	2	0
Nitrobenzene	RN <sub>32</sub>	14	8	1	2-Pyrrolidone	L <sub>16</sub>	19	2	0
Phenol	R <sub>22</sub>	10	5	0	1-Methylpyrrolidine	L <sub>15</sub>	19	2	0
Pyridine	RN <sub>19</sub>	11	7	3	1-Methyl-2-pyrrolidone	L <sub>16</sub>	19	2	0
3-Methylpyridine	RN <sub>12</sub>	9	4	2	Cyclohexane	L <sub>13</sub>	18	2	0
3-Cyanopyridine	RN <sub>36</sub>	15	11	4	Methylcyclohexane	L <sub>16</sub>	19	2	0
3-Aminopyridine	RN <sub>29</sub>	14	9	5	Cyclohexylamine	L <sub>2</sub>	8	1	0
2,6-Lutidine	RN <sub>36</sub>	15	11	4	1,4-Dimethylcyclohexane	L <sub>5</sub>	11	2	0
2,4,6-Trimethylpyridine	RN <sub>12</sub>	9	4	2	2-Methylcyclohexylamine	R <sub>41</sub>	18	4	0
Pyrazine	R <sub>26</sub>	12	8	0	1,2-Cyclohexanediamine	RN <sub>30</sub>	14	6	2
2-Methylpyrazine	RN <sub>12</sub>	9	4	2	2-Methylcyclohexanol	L <sub>16</sub>	19	2	0
2,5-Dimethylpyrazine	RN <sub>5</sub>	6	4	4	1,2,4-Trimethylcyclohexane	R <sub>22</sub>	10	5	0
Cyan pyrazine	RN <sub>29</sub>	14	9	5	Piperidine	RN <sub>21</sub>	11	4	3
Pyrrole	RN <sub>11</sub>	8	6	2	4-Methylpiperidine	L <sub>16</sub>	19	2	0
1-Methylpyrrole	L <sub>6</sub>	11	1	0	4-Aminopiperidine	RN <sub>27</sub>	13	10	1
2,5-Dimethylpyrrole	R <sub>40</sub>	17	11	0	3,5-Dimethylpiperidine	L <sub>13</sub>	18	2	0
Pyrazole	RN <sub>31</sub>	14	13	5	1-Methylpiperidine	L <sub>15</sub>	19	2	0
3-Methylpyrazole	RN <sub>29</sub>	14	9	5	1-Aminopiperidine	L <sub>15</sub>	19	2	0
3-Aminopyrazole	RN <sub>36</sub>	15	11	4	4-Hydroxy-1-methylpiperidine	L <sub>16</sub>	19	2	0
3-Amino-5-methylpyrazole	RN <sub>28</sub>	14	6	3	1-Methylpiperazine	L <sub>16</sub>	19	2	0
1-Methylimidazole	RN <sub>10</sub>	8	5	4	1-Amino-4-methylpiperazine	L <sub>18</sub>	23	2	0
1,2-Dimethylimidazole	L <sub>16</sub>	19	2	0	N,N'-Dimethylpiperazine	L <sub>2</sub>	8	1	0
1H-1,2,3-Triazole	RN <sub>28</sub>	14	6	3	1,3,5-Trimethylhexahydro-1,3,5-triazine <sup>8</sup>	RN <sub>26</sub>	13	6	2
Cyclopentane	L <sub>16</sub>	19	2	0					

Consequently, the reaction route for the generation of carbon products in the SP reaction field based on different intermediates could be proposed, as shown in **Figure 3.11**. The aromatic ring raw material ( $\pi 6-$ ,  $\pi 5-$ ) with nitrogen was easier to form excited particles under the  $\gamma$  effect in the plasma. The electron energy level on the  $\pi$  orbitals is closer to the Fermi energy level of the molecule [1,24,25]. Therefore, the molecules of  $\pi 6-$  and  $\pi 5-$  groups were more reactive and easily activated by the collision of ions at the plasma-solution interface. The appearance of nitrogen-containing radical cations with a benzene ring structure provided the fragments to grow the graphene structure and undergo the oligomerization reactions to form ring-like intermediates with high molecular mass. The ring-like intermediates with high molecular mass, *i.e.*, polycyclic aromatic hydrocarbons, further reacted by polymerization to form high N-containing carbon products. Oppositely, for non-aromatic ring hydrocarbons ( $\sigma 6-$ ,  $\sigma 5-$ ), the C-C bonds were decomposed into short-chain hydrocarbon compounds by thermal interaction at the center of the plasma or by collisional ionization at the plasma-solution interface. The GC/MS results of the intermediate products showed that the decomposed short-chain hydrocarbons gradually formed long-chain hydrocarbon compounds after oligomerization reactions in the solution environment rather than ring-like compounds. Since the nitrogen atoms were less in the intermediate products, there was no bending or distortion of the chain hydrocarbons due to N atoms [26]. Further dehydrogenation and polymerization of the long straight-chain hydrocarbon compounds, catalyzed by the plasma, resulted in a more crystalline final carbon product.





**Figure 3.11.** (a) Reaction routes in SP reaction field from raw materials to final carbon products by intermediates of ring structure and linear structure.

### 3.4 Conclusion

The correlation between the intermediate species in SP reaction field and the structural parameters of carbon products was discovered. The synthesis pathway of N-doped carbons was found to be altered depending on the organic molecules as the raw material. According to the discovered information in this Chapter, in graphene synthesis, non-aromatic ring molecules ( $\sigma 6$ -,  $\sigma 5$ -) are recommended as raw materials for SP reactions to enhance the crystallinity of carbon products.

However, in high N-containing heterogeneous graphene synthesis, aromatic ring molecules ( $\pi 6$ -,  $\pi 5$ -) are recommended as raw materials for the SP reaction to enhance the concentration of N atom doping while ensuring that no excessive defects are introduced to the carbon framework.

## References

1. Morishita, T.; Ueno, T.; Panomsuwan, G.; Hieda, J.; Yoshida, A.; Bratescu, M.A.; Saito, N. Fastest formation routes of nanocarbons in solution plasma processes. *Sci Rep* **2016**, *6*, 36880.
2. Niu, J.; Chokradjaroen, C.; Saito, N. Graphitic n-doped graphene via solution plasma with a single dielectric barrier. *Carbon* **2022**, *199*, 347-356.
3. Niu, J.; Chokradjaroen, C.; Sawada, Y.; Wang, X.; Saito, N. Plasma–solution junction for the formation of carbon material. *Coatings* **2022**, *12*.
4. Liu, W.; Chai, M.; Hu, W.; Zhao, L.; Tian, J. Generation of atmospheric pressure diffuse dielectric barrier discharge based on multiple potentials in air. *Plasma Science and Technology* **2019**, *21*.
5. Chokradjaroen, C.; Niu, J.; Panomsuwan, G.; Saito, N. Insight on solution plasma in aqueous solution and their application in modification of chitin and chitosan. *Int J Mol Sci* **2021**, *22*.
6. Chen, Q.; Kaneko, T.; Matsuda, N.; Hatakeyama, R. Potential structure of discharge plasma inside liquid directly measured by an electrostatic probe. *Applied Physics Letters* **2013**, *102*.
7. Chen, Q.; Kaneko, T.; Hatakeyama, R. Characterization of pulse-driven gas-liquid interfacial discharge plasmas and application to synthesis of gold nanoparticle-DNA encapsulated carbon nanotubes. *Current Applied Physics* **2011**, *11*, S63-S66.
8. Chen, C.; Fu, W.; Zhang, C.; Lu, D.; Han, M.; Yan, Y. Langmuir probe diagnostics with optical emission spectrometry (oes) for coaxial line microwave plasma. *Applied Sciences* **2020**, *10*.
9. Stollenwerk, L.; Stroth, U. Electric charging in dielectric barrier discharges with asymmetric gamma-coefficients. *Contributions to Plasma Physics* **2011**, *51*, 61-67.
10. Li, X.; Wu, K.; Liu, R.; Yang, L.; Geng, J.; Wang, B.; Jia, P. Spatial–temporal evolution and plasma parameters' diagnosis of a transverse glow discharge in atmospheric pressure air. *IEEE*

*Transactions on Plasma Science* **2019**, *47*, 1330-1335.

11. Hill, N.; Kurrat, M. Discharge mechanisms in liquid nitrogen—breakdown field strength of gaseous nitrogen. *IEEE Transactions on Applied Superconductivity* **2018**, *28*, 1-5.
12. Derzsi, A.; Horváth, B.; Donkó, Z.; Schulze, J. Surface processes in low-pressure capacitive radio frequency discharges driven by tailored voltage waveforms. *Plasma Sources Science and Technology* **2020**, *29*.
13. Arumugam, S.; Alex, P.; Sinha, S.K. Effective secondary electron emission coefficient in dc abnormal glow discharge plasmas. *Physics of Plasmas* **2017**, *24*.
14. Akishev, Y.; Karalnik, V.; Medvedev, M.; Petryakov, A.; Shao, T.; Zhang, C.; Huang, B. About the possible source of seed electrons initiating the very first breakdown in a dbd operating with the air at atmospheric pressure. *Plasma Sources Science and Technology* **2021**, *30*.
15. Kim, K.; Chokradjaroen, C.; Saito, N. Solution plasma: New synthesis method of n-doped carbon dots as ultra-sensitive fluorescence detector for 2,4,6-trinitrophenol. *Nano Express* **2020**, *1*.
16. Kim, K.; Hashimi, K.; Bratescu, M.A.; Saito, N. The initial reactions from pyridine to hetero-carbon nanomaterials through solution plasma. *Nanoscience and Nanotechnology Letters* **2018**, *10*, 814-819.
17. Guo, X.-H.; Wei, X.-Y.; Hu, L.; Liu, X.-J.; Chen, M.-X.; Xu, M.-L.; Zong, Z.-M. Molecular characterization of a middle/low-temperature coal tar by multiple mass spectrometries. *Fuel* **2021**, *306*.
18. Weber, M.; Wolf, J.C.; Haisch, C. Gas chromatography-atmospheric pressure inlet-mass spectrometer utilizing plasma-based soft ionization for the analysis of saturated, aliphatic hydrocarbons. *J Am Soc Mass Spectrom* **2021**, *32*, 1707-1715.
19. Li, J.; Xiong, Z.; Zeng, K.; Zhong, D.; Zhang, X.; Chen, W.; Nzihou, A.; Flamant, G.; Yang, H.; Chen, H. Characteristics and evolution of nitrogen in the heavy components of algae pyrolysis bio-oil. *Environ Sci Technol* **2021**, *55*, 6373-6385.
20. Alves Filho, E.G.; Silva, L.M.A.; de Brito, E.S.; Castro, D.R.G.; Bezerra, J.A.; Sanches, E.A.; Rodrigues, S.; Fernandes, F.A.N.; Campelo, P.H. Effect of glow and dielectric barrier discharges

- plasma on volatile and non-volatile chemical profiling of camu-camu juice. *Food and Bioprocess Technology* **2021**, *14*, 1275-1286.
21. Skrzypek, E. First- and second-order raman spectra of carbonaceous material through successive contact and regional metamorphic events (ryoke belt, sw japan). *Lithos* **2021**, 388-389.
  22. Sebastian, F.L.; Zorn, N.F.; Settele, S.; Lindenthal, S.; Berger, F.J.; Bendel, C.; Li, H.; Flavel, B.S.; Zaumseil, J. Absolute quantification of sp(3) defects in semiconducting single-wall carbon nanotubes by raman spectroscopy. *J Phys Chem Lett* **2022**, *13*, 3542-3548.
  23. Taborowska, P.; Stando, G.; Sahlman, M.; Krzywiewski, M.; Lundstrom, M.; Janas, D. Doping of carbon nanotubes by halogenated solvents. *Sci Rep* **2022**, *12*, 7004.
  24. Panomsuwan, G.; Saito, N.; Ishizaki, T. From cyano-aromatic molecules to nitrogen-doped carbons by solution plasma for the oxygen reduction reaction in alkaline medium. *Materials Today: Proceedings* **2015**, *2*, 4302-4308.
  25. Panomsuwan, G.; Saito, N.; Ishizaki, T. Electrocatalytic oxygen reduction on nitrogen-doped carbon nanoparticles derived from cyano-aromatic molecules via a solution plasma approach. *Carbon* **2016**, *98*, 411-420.
  26. Naraprawatphong, R.; Chokradjaroen, C.; Thiangtham, S.; Yang, L.; Saito, N. Nanoscale advanced carbons as an anode for lithium-ion battery. *Materials Today Advances* **2022**, *16*.

## ***Chapter 4***

***Plasma Potential Induced by Solution Plasma  
in Cyclic Organic Compounds and the  
Structural Correlation with the Raw Molecules***

## ***Chapter 4 - Plasma Potential Induced by Solution Plasma in Cyclic Organic Compounds and the Structural Correlation with the Raw Molecules***

### **4.1 Introduction**

The previous chapters showed the correlation between the properties of raw materials and intermediate in the SP reaction field and the structural parameters of the obtained carbon products. However, this obtained information could allow us to understand the phenomena inside the plasma and the solution near the plasma-liquid interface. In the plasma phase,  $CN^*$ , as an important chemically active radical, affected the nitrogen doping content of the final carbon products. The  $CN^*$  reactive radicals were mainly produced by 6- or 5- aromatic hydrocarbons. In the solution near the plasma-liquid interface, many ring-like nitrogen-containing intermediates were produced to promote the nitrogen doping content of the carbon products. The ring containing nitrogen intermediates was mainly derived from 6- aromatic hydrocarbons and some 5-. Among the fifty-three raw materials, 2,5-dimethylhydrazine, pyrazole, 3-amino-5-methyl pyrazole, pyridine, 3-methylpyridine, nitrobenzene, *etc.*, were able to cover the above two characteristics at the same time. However, information on the plasma-liquid interface is still rare; therefore, it is needed to be studied to clearly clarify the SP reaction pathway to produce the carbon products.

For non-equilibrium solution plasma (SP), the plasma phase provides a high-temperature reaction field and high-energy electrons [1,2]. The molecules can be ionized and decomposed by electron bombardment at the initial stage of plasma formation in the plasma phase, *i.e.*, during the development of the electron avalanche. As a result, numerous particles with highly reactive ions, radicals, and

electrons are produced [3-5]. Typical ionic groups include  $C_2^+$ ,  $CN^+$ , and  $H^+$ . However, the particles involved in the carbon framework generation reaction are mainly  $C_2^+$  and  $CN^+$  [6-9]. As mentioned above, these cations are directed and accelerated to the plasma-liquid interface by the potential difference between the plasma phase and the liquid phase, during which carbonization and collisional ionization reactions also occur continuously, as shown in **Figure 4.1**. If the cation is under the effect of high potential difference, it will have higher energy, and thus the  $\gamma$  effect from the collision with the solution molecules in the plasma-liquid interface can be more obvious [10-14]. If the potential difference between the plasma phase and the liquid phase is low, a weaker  $\gamma$  effect has resulted. The potential difference between the phases thus strongly affects the energy obtained by the cations, which was expected to determine the extent to the polymerization reaction within the liquid phase that plays a key role in the synthesis of high N-containing carbons.

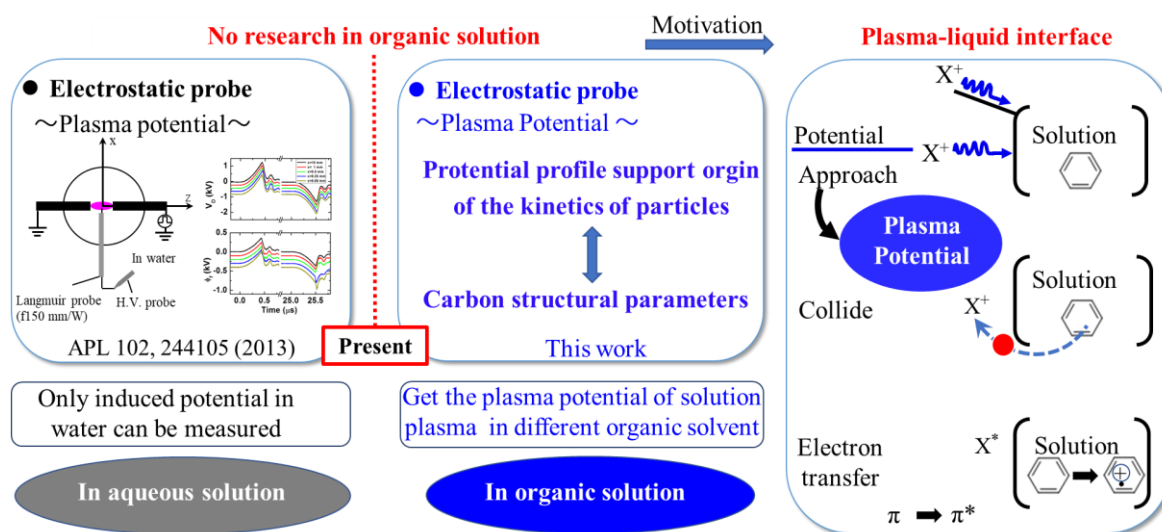
To investigate the relationship between different phases in a solution plasma reaction field, a suitable technique for reliably acquiring the important information within each phase is mandatory. Using a laser is one of the widely used optical methods for the determination of diagnostic plasmas. Lasers have an excellent specific wavelength distribution, *i.e.*, monochromaticity, with equal amplitude phases, which can ensure high brightness and high directionality that can be used in specific directions [15-17]. Plasma interaction with laser light induces a series of reactions such as Thompson scattering, Michael interference, *etc.* By analyzing specific reactions, such as changes in the number and length of stripes, it is possible to theoretically diagnose a specific location of plasma. Thus, the laser method has a high capability to diagnose different phases of plasma. However, the solution plasma generated in organic solvents can rapidly generate carbon products; therefore, the solution quickly turns black and opaque. Therefore, the laser method is unsuitable for solution plasma diagnosis under organic solutions.

The probe method is one of the classic methods for plasma diagnosis [18-23]. A metal probe is inserted into a specific location of the plasma to obtain information about the electron temperature, ion temperature, and potential at the corresponding location. This method has the advantages of high stability, low cost, and relative ease of operation compared to the laser method. However, in the case

of solution plasma, which is a typical high-frequency and high-voltage discharge, once the probe is inserted into the plasma, it will inevitably form a sheath layer on its surface for the purpose of shielding the metal potential. Therefore, the probe size notably influences the information obtained about the plasma. The probe diameter should be smaller than the length of the Debye shield so that credible plasma potential information can be obtained. In 2013, Chen *et al.* carried out a pioneering exploration of the floating potential information of the solution plasma in an aqueous solution environment utilizing the electrostatic probe method [19], as shown in **Figure 4.1**. By comparing the ratio between the probe potential and the discharge potential, they clearly found the floating potential from the plasma phase to the solution phase. The OES information was simultaneously combined and analyzed, thus finally identifying the existence of a double-layer structure with negative ion aggregation within the plasma phase and positive ion aggregation at the plasma-liquid interface in the solution plasma reaction field. The probe method with modification was believed to be one of the alternative methods, which should be suitable for solution plasma diagnosis under organic solutions.

This chapter proposes a diagnostic of the potential information between different phases in the solution plasma reaction field in fifty-three organic solutions using the electrostatic probe technique, as shown in **Figure 4.1**. The necessary process design for the synthesis of high N-containing carbon in solution plasma reaction fields is explored from a kinetic control point of view by establishing a correlation between the potential profile obtained based on the probe method and the structural parameters of the final carbon product.





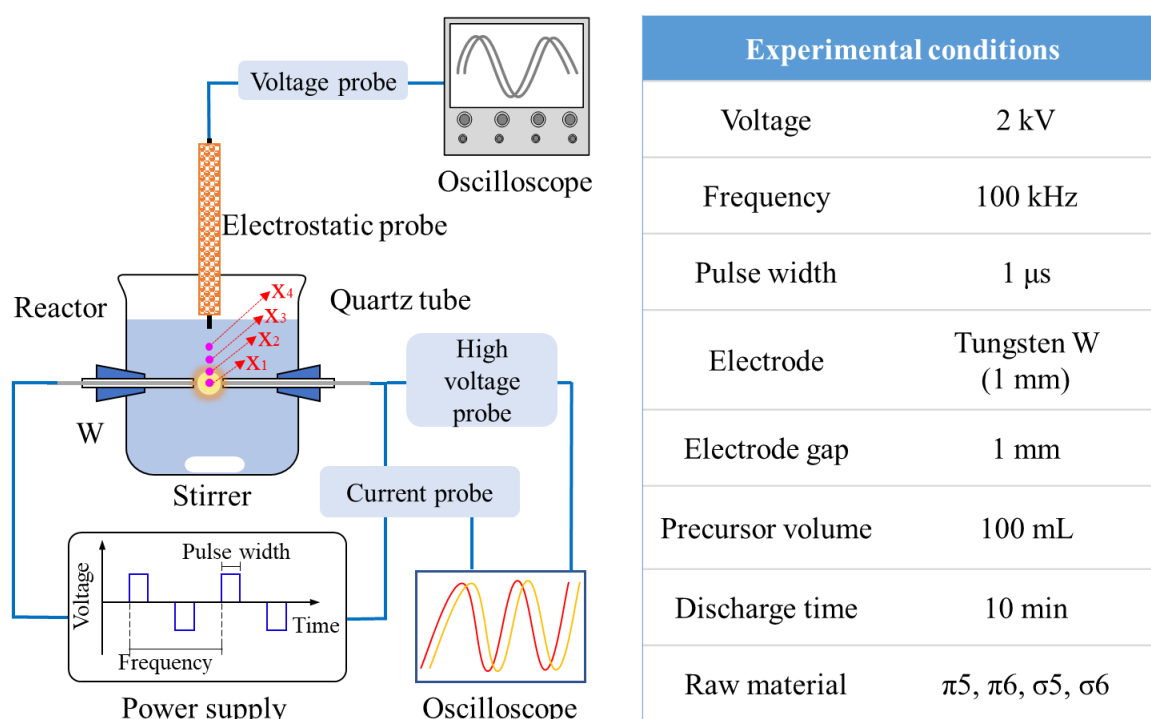
**Figure 4.1.** The schematic diagram of the motivation of applying the electrostatic probe method in organic solution for SP compared with applied to SP in aqueous solution and the electron transfer reaction that happened based on the plasma potential induced collision with molecules at the plasma-liquid interface.

## 4.2 Experimental procedures

**Plasma diagnosing with the electrostatic probe.** To ensure the overall uniformity of this study, the structure of the discharge electrodes and the driving power conditions used in this chapter are consistent with those in Chapters 2 and 3, as shown in **Figure 4.2**. The raw material for discharge generation was also 53 organic materials. The front section of the probe was a tungsten wire with a radius of 50  $\mu\text{m}$ , and the upper surface was covered by a ceramic tube with an inner diameter of 0.4 mm. The tungsten wire was fixed inside the ceramic tube utilizing an intravenous needle, which eliminated the interference of the probe signal caused by particles such as electrons adsorbed on the inner wall of the ceramic tube entering the probe. The tip of the probe was exposed to the ceramic tube by 0.1 mm. It was used to determine the potential signal at different locations in the plasma reaction field. The probe was swept from the plasma phase up to the liquid phase position, and the voltage signal on the electrostatic probe was collected every 0.5 mm using a high voltage probe (P6015A,

1000X, 3.0pF, 100M $\Omega$ , Tektronix, USA) and an oscilloscope (DLM2024, 2.5GS/s, 200MHz, Yokogawa, Japan). This included plasma phase  $x_1$ , gas phase  $x_2$ , liquid phase  $x_3$ , and liquid phase  $x_4$ .

**Carbon products characterization.** The methods of characterization of carbon products were the same as in chapter 2 and chapter 3. It includes the crystallinity of carbon conducted through X-ray diffraction (XRD, Smartlab, Rigaku Co., Japan) with a Cu K $\alpha$  ( $\lambda = 0.154$  nm) X-rays source. The index of defect of carbon was conducted by Raman spectra microscope (Raman, Leica DM 2500M Ren (RL/TL), Renishaw Plc, England) utilizing a laser wavelength of 532.5 nm. The N content of carbon was conducted by Elemental analysis (EA) with Perkin Elmer 2400 Series II CHNS/O analyzer.



**Figure 4.2.** Schematic image of the experiment setup and the exact experimental conditions, including the parameters of power sources, electrode configuration, and the discharge time; setup of the electrostatic probe at the different positions of  $x_1$  (plasma phase),  $x_2$  (gas phase),  $x_3$  (liquid phase) and  $x_4$  (liquid phase) was shown at the top the baker.

### 4.3 Results and discussion

Figures 4.3-4.6 show the results of the probe measurement for the solution plasma using fifty-three raw materials in the reaction field with. The plasma phase was set as the original position, *i.e.*, 0 mm, and gradually moving 0.5 mm in sequence and obtaining the normalized floating potential ( $\phi_{\text{probe}}/V_{\text{Discharge}}$ ) as a function of probe position which represented the plasma phase, gas, and liquid phases. The solution plasma using the solution of molecules in the  $\pi 6$ - group as the raw materials revealed the possibility of increasing or decreasing the floating potential in the gas phase compared to that in the plasma phase without any obvious pattern, as shown in **Figure 4.3**. Among these molecules, cyanpyrazine showed the most obvious increase of the potential in the gas phase. For the molecules in the  $\pi 5$ - group, the floating potential from the plasma phase to the gas phase showed a decreasing trend, except for the 3-amino-5-methyl pyrazole. Meanwhile, for the molecules in the  $\sigma 5$ - group, the potential from the plasma phase to the gas phase and liquid phase showed a gradually decreasing trend, but only 1-methyl pyrrolidine has a gradually increasing trend. For the molecules in the  $\sigma 6$ - group, there was a gradual increase in the floating potential from the plasma phase to the gas phase and liquid phase, including 2-methylcyclohexanol, 1-amino-4-methylpiperazine, and 1-3-5-trimethylhexahydro-1-3-5-triazine. According to the obtained results, the changes in the floating potentials could not be classified based on the chemical activity of raw materials due to the complexity of the solution plasma reaction field. In general, the gradual decrease of the electric potential from the plasma phase to the gas phase and the liquid phase should be found [24]. However, in this study, a different phenomenon was found, the increase in potential. To have a better understanding the nature of the physical meaning of the plasma floating potential in a more profound way, the equivalent circuit diagram method was used to equivalently convert the plasma phase, gas phase, and liquid phase components. It helped to explore further particles' movement under the action of electric potential.

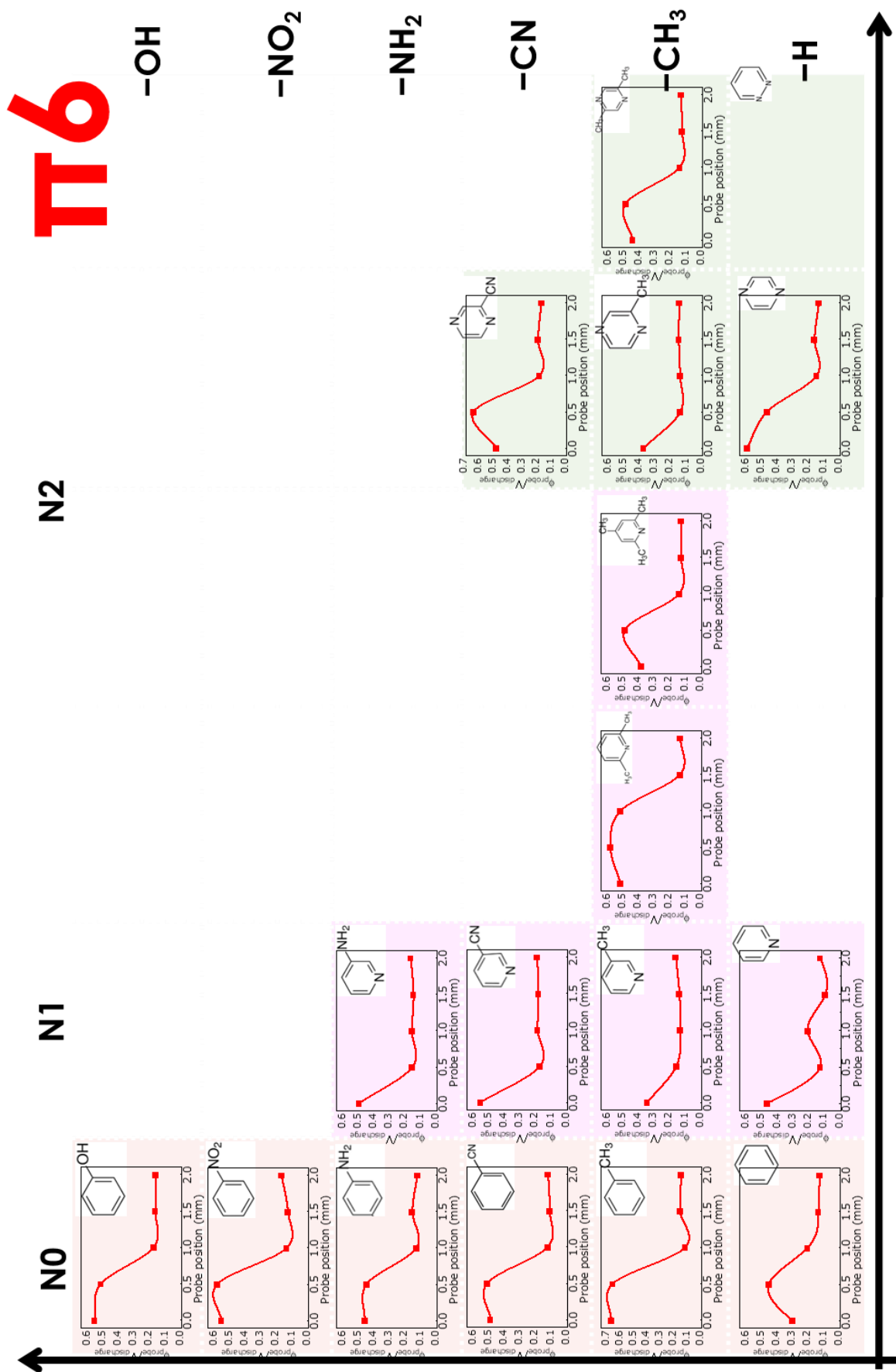


Figure 4.3. Profile of plasma potential in the SP reaction filed corresponding to the raw materials of  $\pi 6$ .

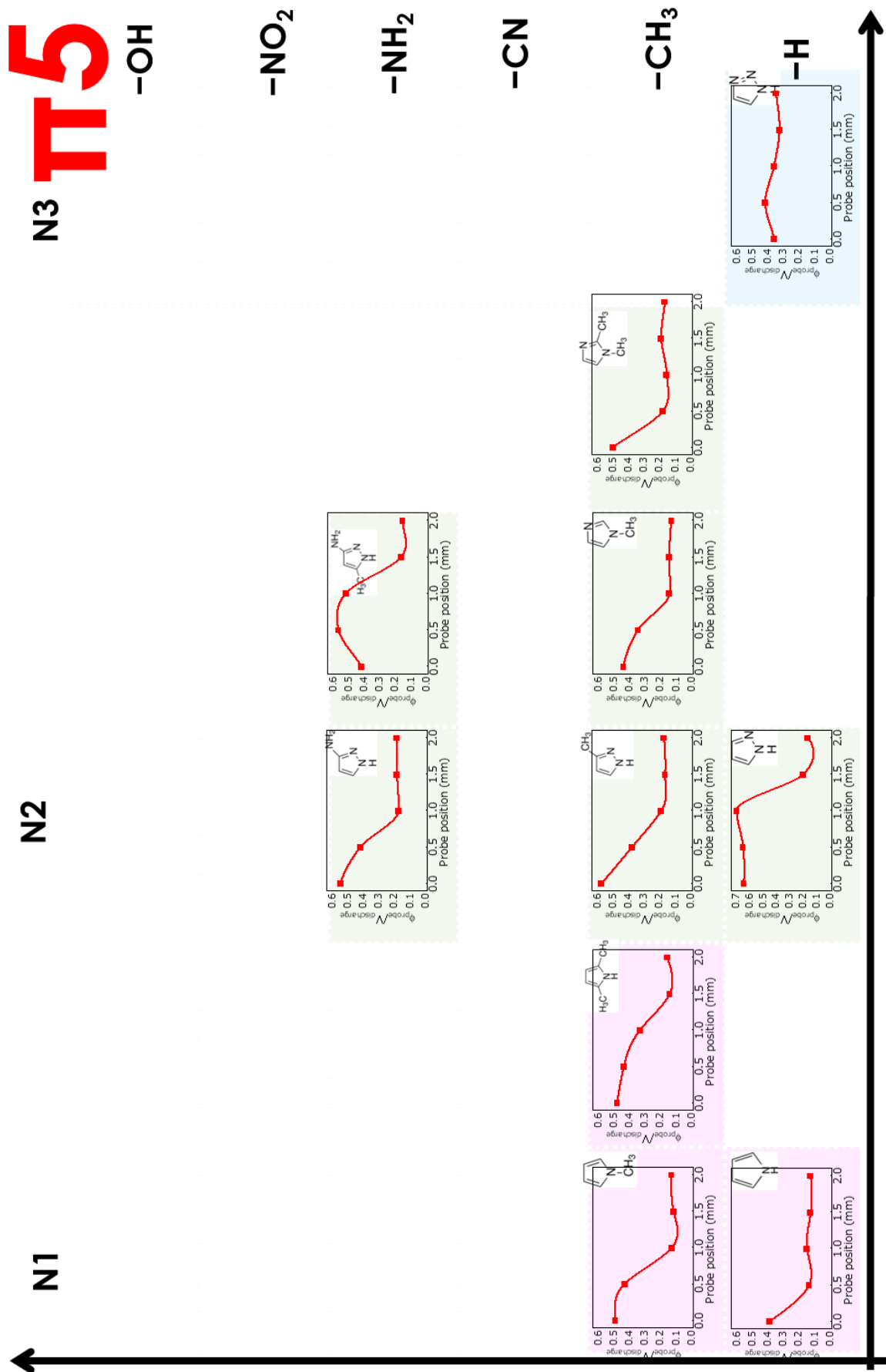


Figure 4.4. Profile of plasma potential in the SP reaction filed corresponding to the raw materials of  $\pi_5$ .

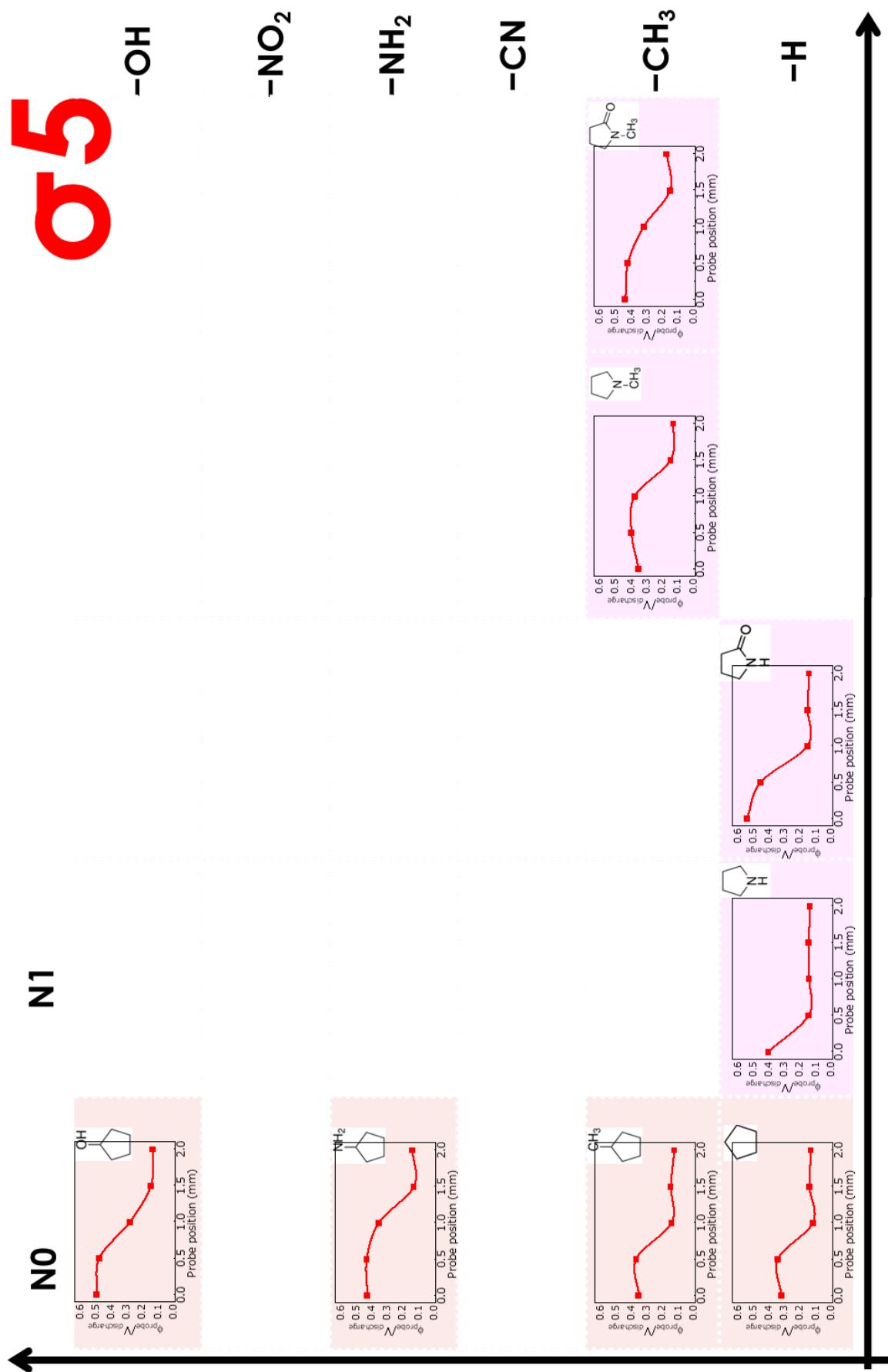


Figure 4.5. Profile of plasma potential in the SP reaction filed corresponding to the raw materials of  $\sigma_5$ .

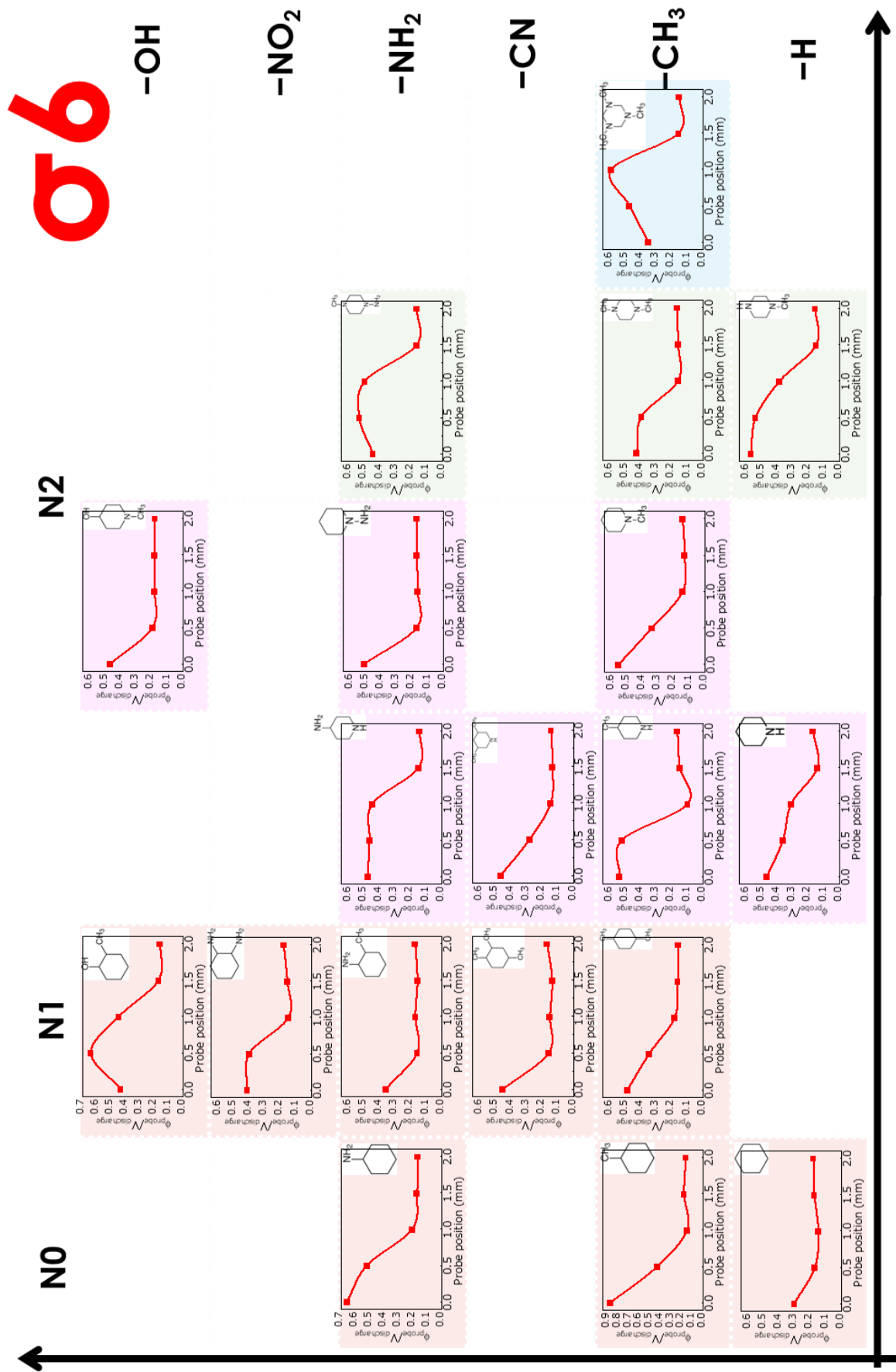
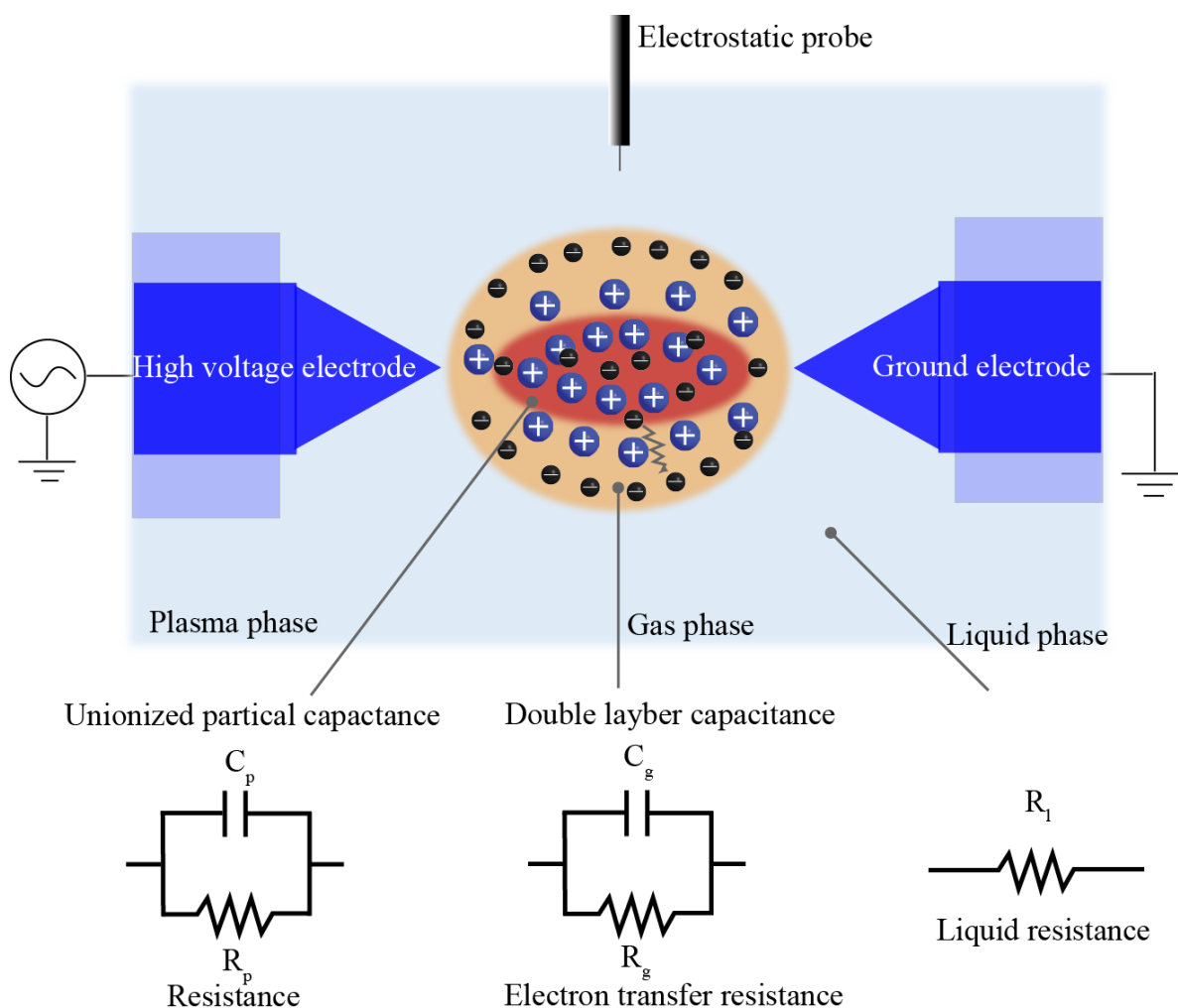


Figure 4.6. Profile of plasma potential in the SP reaction filed corresponding to the raw materials of  $\sigma_6$ .

**Figure 4.7** shows the equivalent circuit diagram for different parts in the solution plasma reaction field. Since the plasma was the ionization achieved by the molecules of the solution part, and thus the plasma phase had resistive and capacitive properties, the equivalent circuit of the plasma phase was composed of a series connection of resistance  $R_p$  and capacitance  $C_p$  [25-27]. The gas phase was a vapor layer formed by the heat of the solution molecules, and there were particles such as ions supplied by the plasma phase inside it; thus, the gas phase also had resistive and capacitive properties, *i.e.*, the equivalent circuit of the gas phase consisted of the resistance  $R_g$  and the capacitance  $C_g$  in series. Finally, the solution phase should not have many conducting particles, and thus its equivalent circuit had only a resistive component  $R_l$ .



**Figure 4.7.** Equivalent circuit diagram of the measurement by the electrostatic probe in solution plasma reaction field;  $C_p$ ,  $R_p$  are the equivalent capacitance and resistance of the plasma phase;  $C_g$ ,  $R_g$



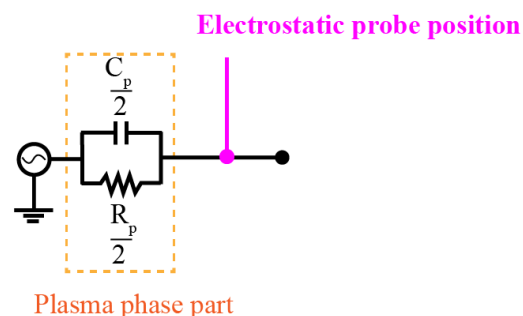
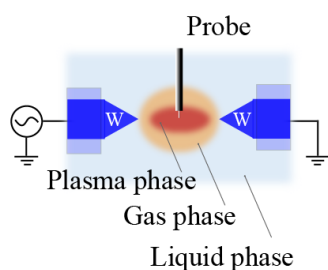
are the equivalent capacitance and resistance of the gas phase;  $R_1$  is the equivalent resistance of the liquid phase.

The equivalent circuit schematic for the measurement of the floating potential within different phases in the plasma reaction field using the electrostatic probe method is shown in **Figure 4.8**. Since the probe was in the middle of the plasma, the discharge voltage supplied by the power supply was first consumed by half of the equivalent resistance and half of the equivalent capacitance of the plasma phase, and finally conducted to the electrostatic probe. When the electrostatic probe detected the potential of the gas phase, as shown in **Figure 4.8(b)**, the power supply voltage was first consumed by half of the resistance and capacitance of the plasma phase, after which a voltage drop was formed in the resistance and capacitance of the gas phase, and finally, the remaining voltage was conducted to the electrostatic probe. Similarly, when the electrostatic probe performed potential detection for the liquid phase, as shown in **Figure 4.8(c)**, the power supply potential further formed a voltage drop across the solution resistance, which was finally conducted to the electrostatic probe. The same power supply voltage with different discharge materials can also cause the plasma phases to have large differences in equivalent resistance and capacitance. The capacitive component is constantly in the process of charging and discharging in the AC circuit. When the charged particles move to the gas phase, the capacitance's ability to store charge is increased, which in turn causes an increase in the potential at the probe position compared to the plasma phase [28]. The proposed analysis provided an understanding of the increased potential in the gas or liquid phase compared to the plasma phase from the electrical engineering point of view, which further deepened my understanding of the working principle of the electrostatic probe.

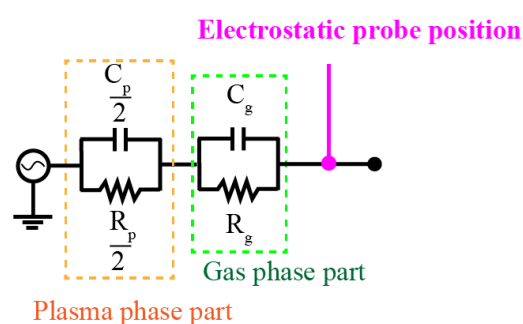
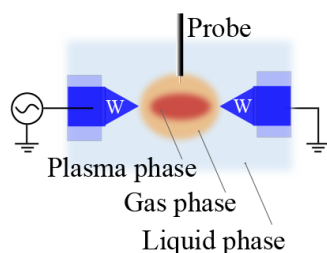
To further discover the pattern of potential variation between different phases, standardized floating potential profiles of each raw material were plotted and listed according to the high and low potential of the liquid phases from left to right, as shown in **Figure 4.9**. The number of raw materials corresponding to each phase-dominated potential profile is also indicated. It can obviously observe

that there were three different potential profiles, including  $\phi_{p0-0.5-1}$  domination with high potential from the plasma phase to the liquid phase,  $\phi_{p0-0.5}$  domination with high potential from the plasma phase to the gas phase, and  $\phi_{p0}$  domination with high potential in the plasma phase only.

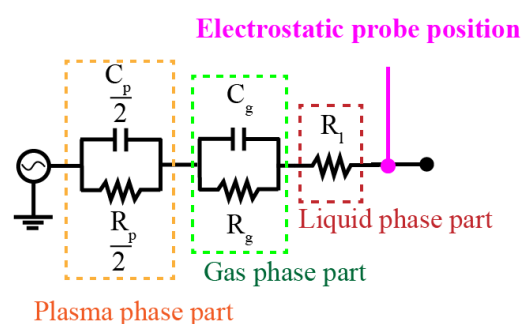
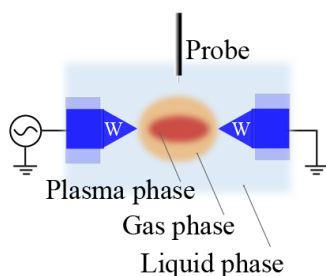
(a) Probe measurement of plasma phase



(b) Probe measurement of gas phase



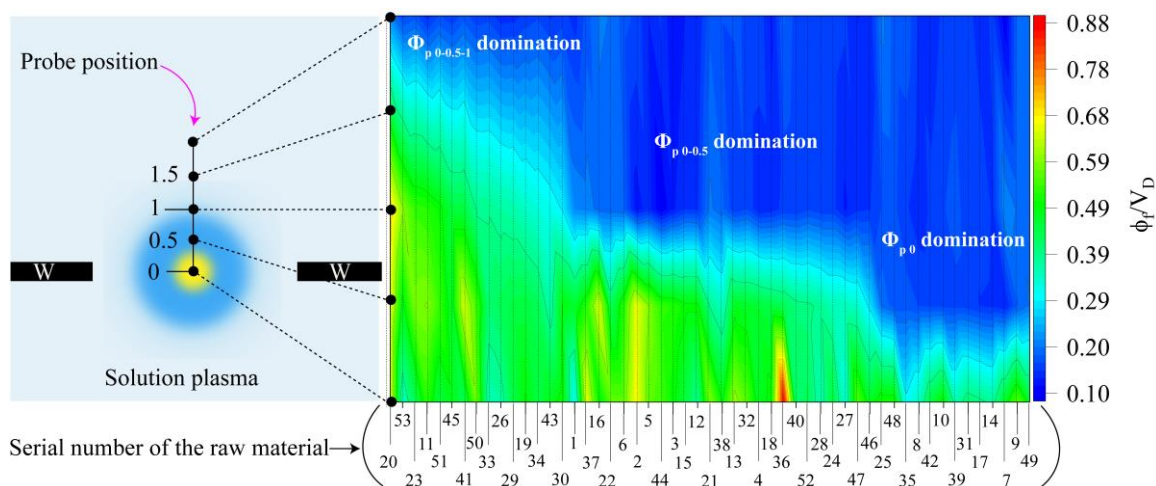
(c) Probe measurement of liquid phase



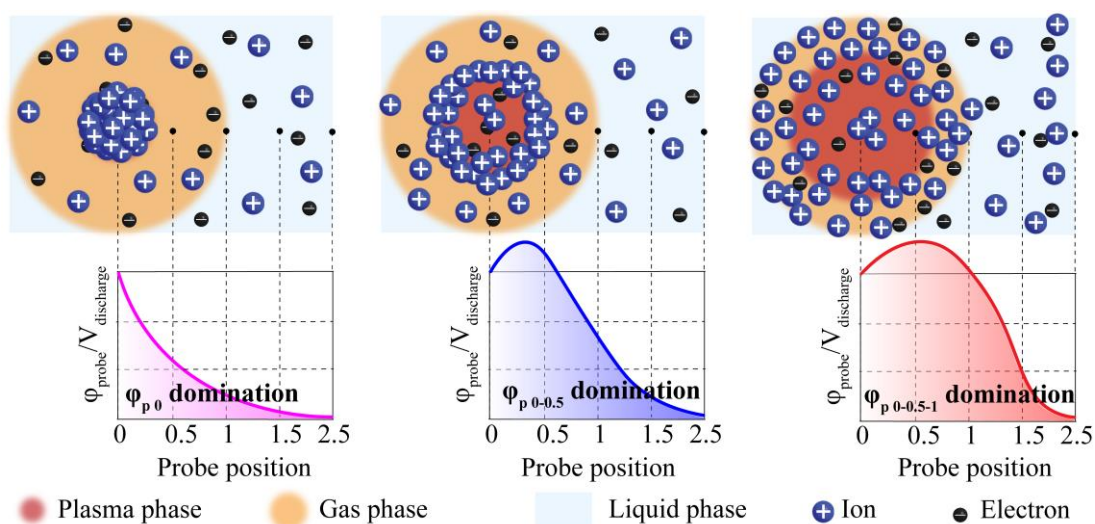
**Figure 4.8.** The equivalent circuit diagram of the electrostatic probe for the potential detection of different phases. (a) plasma phase, (b) gas phase, (c) liquid phase.

The high potential domination in different phases could be analyzed from the kinetic viewpoint, as given in **Figure 4.10**. The  $\phi_{p0}$  domination referred to the presence of more positively charged particles within the plasma phase compared to the gas or liquid phase. The  $\phi_{p0-0.5}$  domination implied the presence of a more significant density of positive charges in both the plasma phase and the gas

phase due to the charge aggregation by moving toward the plasma boundary under the effect of the sheath layer. Similarly, the  $\phi_{p0-0.5-1}$  domination referred to the charges which were more uniformly aggregated in the plasma phase, gas phase, and liquid phase. The above states of potential distribution clearly reflected the existence form of active particles in the plasma reaction field.

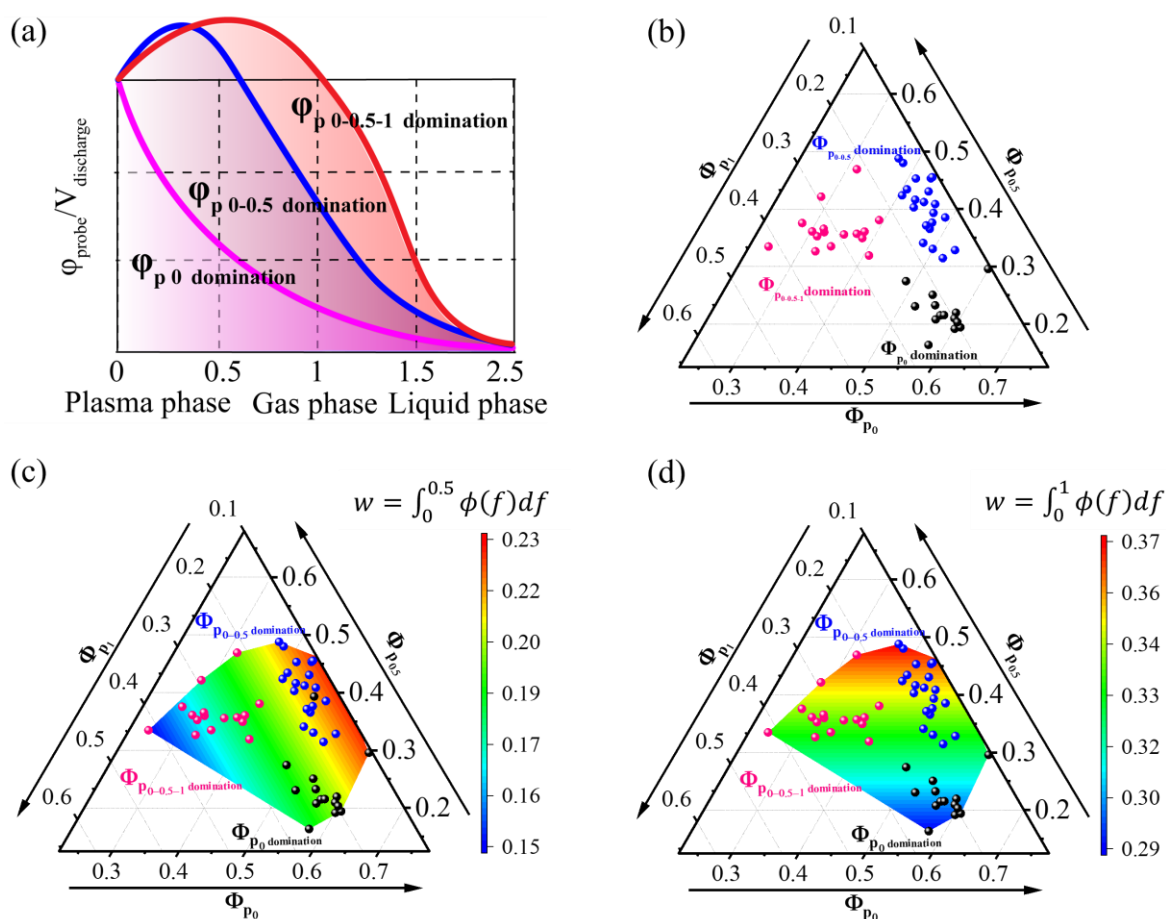


**Figure 4.9.** The mapping of the normalized potential profiles from each raw material as the function of the position of the probe. The serial numbers of the raw material were labeled at the bottom of the mapping.



**Figure 4.10.** The particle distribution in SP reaction field corresponds to the patterns of normalized potential domination, including  $\phi_{p0}$  domination,  $\phi_{p0-0.5}$  domination, and  $\phi_{p0-0.5-1}$  domination.

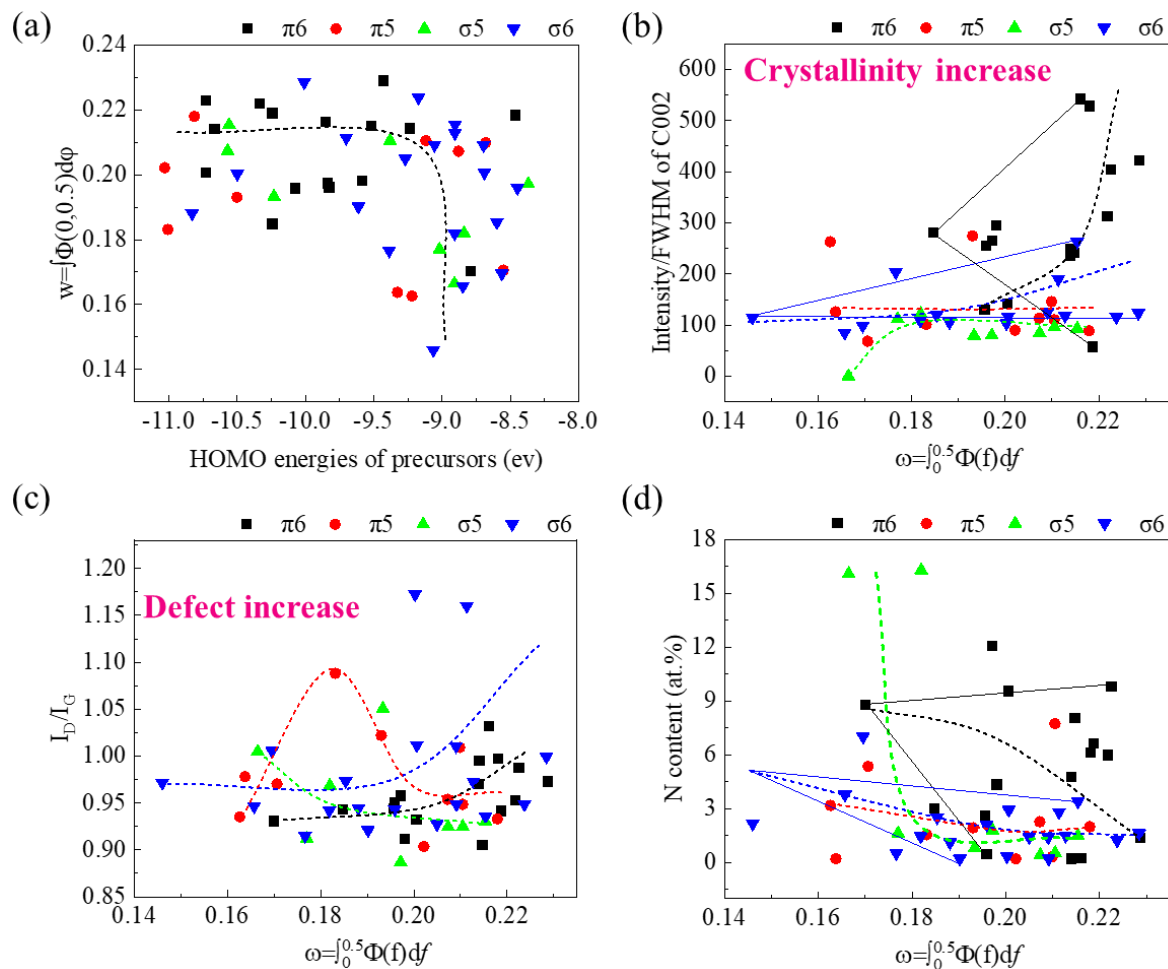
Based on the three different potential-dominated profile patterns in **Figure 4.11(a)**, ternary scatter diagrams could be presented with respect to positions 0 mm, 0.5 mm, and 1 mm, as in **Figure 4.11(b)**. **Figure 4.11(c)** shows the integration of the normalized potential over the probe positions 0 to 0.5 mm, with the pattern of  $\phi_{p0-0.5}$  having the largest integration value. **Figure 4.11(d)** shows the integration of standardized potential over the probe positions 0 to 1 mm, where the larger integration values contain both a part of the pattern of  $\phi_{p0-0.5}$  and a part of the pattern of  $\phi_{p0-0.5-1}$ . To briefly summarize, the integration of the potential over the probe position reflected the magnitude of the energy obtained by the charged particles after being accelerated. Thus, to further discover the correlation between the potential and the property of raw materials and the structural parameters of the carbon products.



**Figure 4.11.** (a) Patterns of the potential profiles including  $\phi_{p0}$  domination,  $\phi_{p0-0.5}$  domination and  $\phi_{p0-0.5-1}$  domination; (b) A ternary scatter plot with the potential at 0 mm, 0.5 mm, and 1 mm as coordinates, the three different potential domination regions were marked using different colors; (c) Integration of

normalized potential profile over probe position from 0 to 0.5 mm; (d) Integration of normalized potential profile over probe position from 0 to 1 mm.

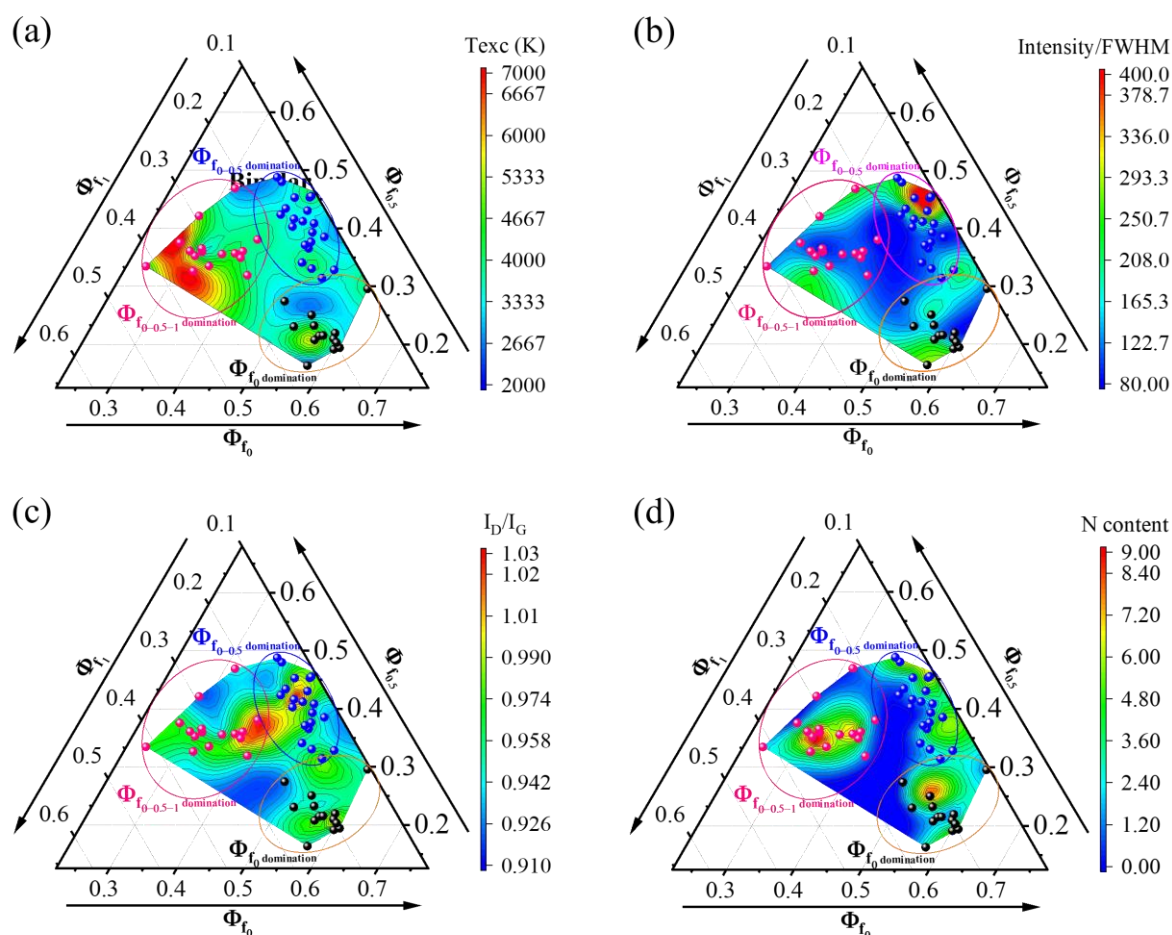
**Figure 4.12** shows the correlation between the work of the electric potential within the 0 to 0.5 mm probe position and the energy value of the highest molecular occupied orbital (HOMO) of the raw material molecule. As the energy of HOMO increased, *i.e.*, the ionization potential of the molecule increased, the integration of the work done by the electric potential within 0 to 0.5 mm showed a trend of invariance followed by a gradual decrease. This phenomenon could be caused by the fact that the higher HOMO energy led to a lower ionization process of the molecules driven by the same supply voltage, which resulted in both the plasma phase and the gas phase having a lower density of charged particles [21,29-32]. Thus, it could lead to a decrease of the potential within 0 to 0.5 mm. **Figure 4.12(b)** shows the trend of crystallinity (intensity/FWHM of C002 peak from XRD results) index of carbon products regarding the work done by the electric potential in the plasma reaction field from 0 to 0.5 mm. The degree of crystallinity of the carbon products gradually increased as the work done by the electric potential became larger. This could be explained by the higher reactivity of particles such as C<sub>2</sub> involved in the formation of carbon framework under the effect of higher electric potential. As a result, the process of dehydrogenation reaction was found to be enhanced, and thus a relatively high degree of crystallinity of carbon products was obtained. **Figure 4.12(c)** shows the correlation between the defect parameters ID/IG of Raman results for carbon products with respect to the work done by the electric potential. As the work done by the electric potential increased, there was no drastic change in the degree of defects in the carbon products, which might be due to the involvement of the heteroatomic components and perturbation of the chemical reactions in the formation of the carbon products. **Figure 4.12(d)** shows the correlation between the N component content in the carbon products regarding the work done by the electric potential in the range of 0 to 0.5 mm. However, a more regularly varying curvilinear correlation did not appear in this component.



**Figure 4.12.** (a) The correlation of the integration work done by the potential from 0 to 0.5 mm with the HOMO energies of the raw materials; (b) The correlation of the crystallinity of carbon products with the integration work done by the potential from 0 to 0.5 mm; (c) The correlation of the  $I_D/I_G$  of Raman from carbon products with the integration work done by the potential from 0 to 0.5 mm; (d) The correlation of the N content of carbon products with the integration work done by the potential from 0 to 0.5 mm.

**Figure 4.13** shows the correlation map of the patterning of the electric potential profiles using ternary contour plots about the plasma reaction field with the excitation temperature and the structural parameters of the carbon products. **Figure 4.13(a)** shows that the dominant region of  $\phi_{p0-0.5-1}$  had a higher electron excitation temperature. It could indicate that a higher potential from the plasma phase to the liquid phase will simultaneously raise the temperature of the plasma reaction field. Combined

with **Figure 4.13(b)** and **(c)**, a higher potential from the plasma phase to the gas phase was significantly found to enhance the crystallinity of the carbon products. A similar result was also found in **Figure 4.12(b)**. **Figure 4.13(d)** reveals the correlation between the N content of the carbon products and the potential-dominated pattern within the plasma reaction field. The carbon products with high N content could be formed in both the  $\Phi_{p0}$  and  $\Phi_{p0-0.5-1}$  regions. Previously, **Figure 4.12(d)** also shows the consistent result that there was no strong correlation between the high N-containing carbon products obtained in the plasma reaction field and the suspension potential of the plasma phase, the gas phase, and the liquid phase.



**Figure 4.13.** (a) The correlation of the domination patterns of normalized floating potential with the excitation temperature of plasma; (b) The correlation of the domination patterns of normalized floating potential with the N content of carbon materials; (c) The correlation of the domination patterns of normalized floating potential with the  $I_D/I_G$  of Raman from carbon products; (d) The correlation of the

domination patterns of normalized floating potential with the crystallinity of carbons from C002 peak of XRD characterization.

#### 4.4 Conclusion

The correlation between the electric potential in SP reaction field and the structural parameters of carbon products was investigated. The electric potential at different phases (*i.e.*, plasma, interface, and gas phases) was evaluated by an electrostatic probe technique. As a result, the reaction field with the high electric potential in the plasma phase could result in the formation of graphite-like carbon. However, there was an unclear correlation between the electric potential and nitrogen content in the carbon products.

#### References

1. Saito, N.; Bratescu, M.A.; Hashimi, K. Solution plasma: A new reaction field for nanomaterials synthesis. *Japanese Journal of Applied Physics* **2018**, *57*.
2. Takai, O. Solution plasma processing (spp). *Pure and Applied Chemistry* **2008**, *80*, 2003-2011.
3. Chae, S.; Panomsuwan, G.; Bratescu, M.A.; Teshima, K.; Saito, N. P-type doping of graphene with cationic nitrogen. *ACS Applied Nano Materials* **2019**, *2*, 1350-1355.
4. Kim, K.; Chokradjaroen, C.; Saito, N. Solution plasma: New synthesis method of n-doped carbon dots as ultra-sensitive fluorescence detector for 2,4,6-trinitrophenol. *Nano Express* **2020**, *1*.
5. Kim, K.; Hashimi, K.; Bratescu, M.A.; Saito, N. The initial reactions from pyridine to hetero-carbon nanomaterials through solution plasma. *Nanoscience and Nanotechnology Letters* **2018**, *10*, 814-819.
6. Chae, S.; Phan, P.Q.; Panomsuwan, G.; Bratescu, M.A.; Hashimoto, T.; Teshima, K.; Saito, N. Single-walled carbon nanotubes wrapped by cationic nitrogen-doped carbon for electrocatalytic applications. *ACS Applied Nano Materials* **2020**, *3*, 10183-10189.
7. Chokradjaroen, C.; Niu, J.; Panomsuwan, G.; Saito, N. Insight on solution plasma in aqueous



- solution and their application in modification of chitin and chitosan. *Int J Mol Sci* **2021**, *22*.
8. Heo, Y.K.; Bratescu, M.A.; Ueno, T.; Saito, N. Synthesis of mono-dispersed nanofluids using solution plasma. *J Appl Phys* **2014**, *116*, 024302.
  9. Heo, Y.K.; Lee, S.H.; Bratescu, M.A.; Kim, S.M.; Lee, G.J.; Saito, N. Generation of non-equilibrium condition in solution plasma discharge using low-pass filter circuit. *Plasma Processes and Polymers* **2016**, *14*.
  10. Arumugam, S.; Alex, P.; Sinha, S.K. Effective secondary electron emission coefficient in dc abnormal glow discharge plasmas. *Physics of Plasmas* **2017**, *24*.
  11. Derzsi, A.; Horváth, B.; Donkó, Z.; Schulze, J. Surface processes in low-pressure capacitive radio frequency discharges driven by tailored voltage waveforms. *Plasma Sources Science and Technology* **2020**, *29*.
  12. Hill, N.; Kurrat, M. Discharge mechanisms in liquid nitrogen—breakdown field strength of gaseous nitrogen. *IEEE Transactions on Applied Superconductivity* **2018**, *28*, 1-5.
  13. Li, X.; Wu, K.; Liu, R.; Yang, L.; Geng, J.; Wang, B.; Jia, P. Spatial–temporal evolution and plasma parameters’ diagnosis of a transverse glow discharge in atmospheric pressure air. *IEEE Transactions on Plasma Science* **2019**, *47*, 1330-1335.
  14. Stollenwerk, L.; Stroth, U. Electric charging in dielectric barrier discharges with asymmetric gamma-coefficients. *Contributions to Plasma Physics* **2011**, *51*, 61-67.
  15. Funaba, H.; Yasuhara, R.; Uehara, H.; Yamada, I.; Sakamoto, R.; Osakabe, M.; Den Hartog, D.J. Electron temperature and density measurement by thomson scattering with a high repetition rate laser of 20 khz on lhd. *Sci Rep* **2022**, *12*, 15112.
  16. Miles, R.B.; Michael, J.B.; Limbach, C.M.; McGuire, S.D.; Chng, T.L.; Edwards, M.R.; DeLuca, N.J.; Shneider, M.N.; Dogariu, A. New diagnostic methods for laser plasma- and microwave-enhanced combustion. *Philos Trans A Math Phys Eng Sci* **2015**, *373*.
  17. Ross, J.S.; Park, H.S.; Amendt, P.; Divol, L.; Kugland, N.L.; Rozmus, W.; Glenzer, S.H. Thomson scattering diagnostic for the measurement of ion species fraction. *Rev Sci Instrum* **2012**, *83*, 10E323.

18. Kiel, R.E. Continuum electrostatic probe theory for large sheaths on spheres and cylinders. *Journal of Applied Physics* **1969**, *40*, 3668-3673.
19. Chen, Q.; Kaneko, T.; Matsuda, N.; Hatakeyama, R. Potential structure of discharge plasma inside liquid directly measured by an electrostatic probe. *Applied Physics Letters* **2013**, *102*.
20. Chiad, B.T.; Hammadi, O.A.; Kadhim, F.J.; Khalaf, M.K. Langmuir probe diagnostics of low-pressure glow discharge plasma using argon-nitrogen mixtures. *IRAQI JOURNAL OF APPLIED PHYSICS* **2016**.
21. Arumugam, S.; Perumal, M.; Anjana, K.P.; Satyanarayana, S.V.M.; Sinha, S.K. Plasma–metal junction. *Physics of Plasmas* **2020**, *27*.
22. Chen, C.; Fu, W.; Zhang, C.; Lu, D.; Han, M.; Yan, Y. Langmuir probe diagnostics with optical emission spectrometry (oes) for coaxial line microwave plasma. *Applied Sciences* **2020**, *10*.
23. Hippler, R.; Cada, M.; Hubicka, Z. Time-resolved langmuir probe diagnostics of a bipolar high power impulse magnetron sputtering discharge. *Applied Physics Letters* **2020**, *116*.
24. Kolobov, V.; Godyak, V. Electron kinetics in low-temperature plasmas. *Physics of Plasmas* **2019**, *26*.
25. Qiao, L.; Zhang, X.; Yan, B.; Han, Z.; Yang, C.; Liu, Y. Analysis of underwater plasma discharge based on equivalent circuit parameters. *AIP Advances* **2021**, *11*.
26. Nishida, K.; Mochizuki, S.; Ohta, M.; Yasumoto, M.; Lettry, J.; Mattei, S.; Hatayama, A. Equivalent circuit of radio frequency-plasma with the transformer model. *Rev Sci Instrum* **2014**, *85*, 02B117.
27. Foster, J.; Sommers, B.; Weatherford, B.; Yee, B.; Gupta, M. Characterization of the evolution of underwater dbd plasma jet. *Plasma Sources Science and Technology* **2011**, *20*.
28. Magar, H.S.; Hassan, R.Y.A.; Mulchandani, A. Electrochemical impedance spectroscopy (eis): Principles, construction, and biosensing applications. *Sensors (Basel)* **2021**, *21*.
29. Lian, Z.; Sakamoto, M.; Vequizo, J.J.M.; Ranasinghe, C.S.K.; Yamakata, A.; Nagai, T.; Kimoto, K.; Kobayashi, Y.; Tamai, N.; Teranishi, T. Plasmonic p-n junction for infrared light to chemical energy conversion. *J Am Chem Soc* **2019**, *141*, 2446-2450.

30. Xu, F.; Meng, K.; Cheng, B.; Wang, S.; Xu, J.; Yu, J. Unique s-scheme heterojunctions in self-assembled tio<sub>2</sub>/cspbbr<sub>3</sub> hybrids for co<sub>2</sub> photoreduction. *Nat Commun* **2020**, *11*, 4613.
31. Zhu, D.; Huang, Y.; Zhang, L.; Fan, H.; Wang, H. Pf<sub>6</sub> – intercalation into graphite electrode from gamma-butyrolactone/ethyl methyl carbonate. *Journal of The Electrochemical Society* **2020**, *167*.
32. Wang, X.; Lei, M.; Zhang, T.; Zhang, Q.; Zhang, R.; Yang, M. A water-stable multi-responsive luminescent zn-mof sensor for detecting tnp, nzf and cr<sub>2</sub>o<sub>7</sub>(<sup>2-</sup>) in aqueous media. *Dalton Trans* **2021**, *50*, 3816-3824.

## ***Chapter 5***

### ***Graphitic N-doped Graphene via Solution Plasma with a Single Dielectric Barrier***

# ***Chapter 5 - Graphitic N-doped Graphene via Solution Plasma with a Single Dielectric Barrier***

## **5.1 Introduction**

Based on the obtained correlations from previous chapters, the different raw materials could result in reaction fields with different characteristics, such as active species and intermediates. Six-membered ring molecules could lead to the formation of CN\* radicals in the plasma phase. In contrast, intermediate products in the solution phase were found to be ring-structured molecules with nitrogen inside the ring. This characteristic of the reaction field in the SP could promote the content of nitrogen in carbon products. According to this evidence, a novel discharge system was proposed, in this Chapter, to obtain the reaction field that can significantly enhance the content of nitrogen in carbon products with the planar structure. In other words, the discharge system was expected to provide a stable solution plasma with low-temperature characteristics to produce high nitrogen doped graphene products.

The doping of nitrogen atoms in graphene has various forms of bonding configurations. For example, graphitic nitrogen located in the graphene framework, pyrrole nitrogen bonded in a five-membered ring at the edge, and pyridinic nitrogen bonded in a six-membered ring at the edge, as well as functional groups in the form of nitrile, nitro, *etc.*, are usually presented in the graphene framework [1-5]. It has been reported that pyridinic nitrogen can increase the charge density of  $\pi$ -states near the Fermi energy level in graphene, thus enhancing the electrocatalytic activity of graphene. The five-membered ring structure of pyrrolic nitrogen possesses redox ability [6]. Graphitic nitrogen refers to the nitrogen atoms that are embedded in the graphene framework. The nitrogen atom forms covalent

bonds with the three surrounding carbon atoms based on its lone pair of electrons participating in the  $\pi$ -bond structure of graphene to form a conjugate [7-8]. Thus, graphitic nitrogen donates electrons to the electrical structure of the graphene surface while can ensure that the planarity of the carbon framework is preserved [9]. As a result, it can provide a carrier transport on the surface. However, there is some research reported on graphene doped with graphitic nitrogen (g-NG). Nitrogen-rich raw materials (*e.g.*, urea and ammonia) have been widely used in the carbon synthesis process and frequently resulted in functionalization, not doping [10-32]. The regulation of bonding configuration, especially for graphitic nitrogen, is still challenging.

Utilization of the low-temperature reaction field in the solution plasma process has been reported that it can ensure the nitrogen doping content [21, 23, 24, 28, 31-36]. However, previous studies have reported a maximum nitrogen content of 13.2% in the synthesized carbon products via the conventional solution plasma [21, 24, 37]. Thus, enhancing the percentage of nitrogen doping, especially graphitic nitrogen doping, is still ongoing research. As mentioned before, the studies in Chapters 2 through Chapter 4 demonstrated that the choice of raw materials seriously influenced the characteristics of plasma and carbon products. However, not only the choice of raw materials but it was also believed that controlling the energy of plasma results in the suitable characteristics of plasma to produce high nitrogen doped graphene products. Usually, the conventional pin-to-pin electrode can lead to a plasma with typical instabilities, depending on operating conditions and raw materials. The sudden increase of the reaction field temperature caused by the transition of the plasma mode (*i.e.*, from stable glow discharge to unstable abnormal glow discharge) can hinder the high concentration of nitrogen doping [38-40]. At the same time, it cannot be neglected that the unstable plasma is highly susceptible to the melting of the metal electrode, which inevitably leads to the contamination of the carbon product with metal impurities [41-43].

Accordingly, in this chapter, a system for generating solution plasma using dielectric barrier discharge has been proposed to obtain stable plasma. It is well known that dielectric barrier electrode structures in gas-phase discharges have a long history [43-45]. Inspired by this idea, further suppression of the discharge current is expected to be achieved in the liquid-phase environment using

a dielectric barrier, thus controlling the discharge mode without abrupt changes. A criss-cross electrode system was designed using a single-side dielectric to achieve discharge in organic solutions, as shown in **Figure 5.1**. Moreover, the reasonable selection of raw materials was conducted based on the corrections in the previous chapters. The electrical, morphological, and optical diagnostics of the solution discharges generated by the criss-cross electrode system were carried out to demonstrate the stability of the discharges. Finally, crystallinity characterization using X-ray diffraction (XRD), defect analysis by Raman spectroscopy, N-doping content characterization by X-ray photoelectron spectroscopy (XPS), morphology characterization by field emission scanning electron microscopy (FE-SEM), and nanostructure morphology characterization by transmission electron microscopy (TEM) were conducted for the synthesized carbon products.

## **5.2 Experimental procedures**

### **5.2.1 Experimental setup**

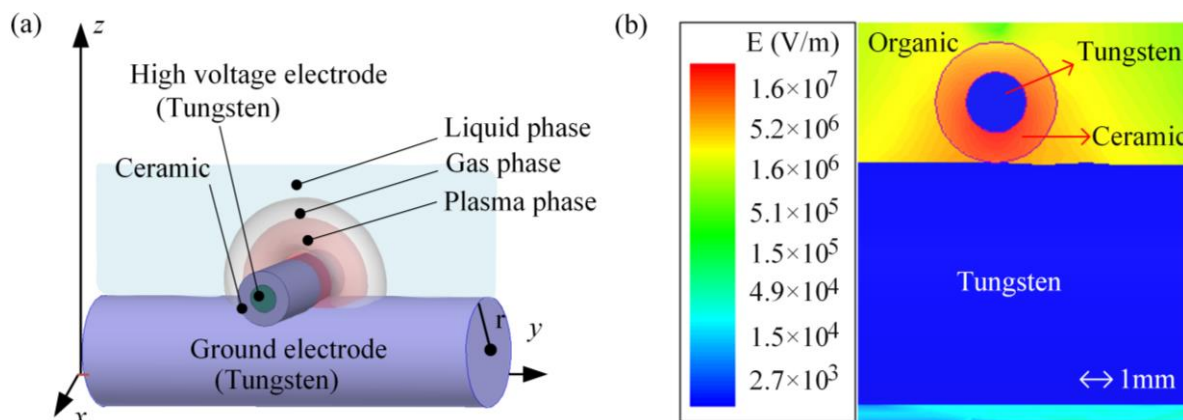
A single dielectric barrier electrode structure with close contact and cross-shaped was arranged at a 90° between the high voltage electrode and the ground electrode, called a criss-cross electrode system, as shown in **Figure 5.1a**. The high voltage electrode was a tungsten rod (W,  $\phi$  1.0 mm, Nilaco Co, Japan) covered with a ceramic tube ( $\phi$  2.0 $\times$ 0.5 $\times$ 100(H) mm, Nilaco Co, Japan) as a dielectric layer. The ground electrode was another tungsten rod (W,  $\phi$  4.0 mm, Nilaco Co, Japan). **Figure 5.2** shows the schematic diagram of the SP experimental setup system. The SP process was driven by an AC power supply (MPS-R06K01C-WP1-6CH, Kurita, Japan). The voltage was measured by a high-voltage probe (P6015A, 1000X, 3.0 pF, 100 M $\Omega$ , Tektronix, USA), and the discharge current was measured by a current probe (PR30, Yokogawa, Japan). The voltage and current (V/I) signals were finally displayed and recorded by a digital oscilloscope (DLM2024, 2.5 GS/s, 200 MHz, Yokogawa, Japan). The generated species during the SP discharge were revealed by using spatially resolved optical emission spectroscopy (SR-OES). The SR-OES consisted of the pinhole with the size of 1 mm, three lenses ( $L_1$ : 4 mm of diameter, 6 mm of focal length;  $L_2$ : 4 mm of diameter, 12 mm of focal length;

$L_3$ : 4 mm of diameter, 5 mm of focal length), optical fiber, and an optical spectrometer (USB2000+, Ocean Optics, USA) with the wavelength range 200–900 nm. This method can overcome the problem of unidirectional spectroscopic detection posed by conventional ways using fibers alone. It can collect light from the entire plasma region for analyzing the composition of spectra. The discharge process was photographed using Nikon Digital Camera D<sub>4</sub> with an exposure time of 125  $\mu$ s. This experiment was carried out in a glass container with a volume of 200 ml, and the electrode was placed at the center of the glass reactor. The entire discharge process was carried out with a magnetic stirrer.

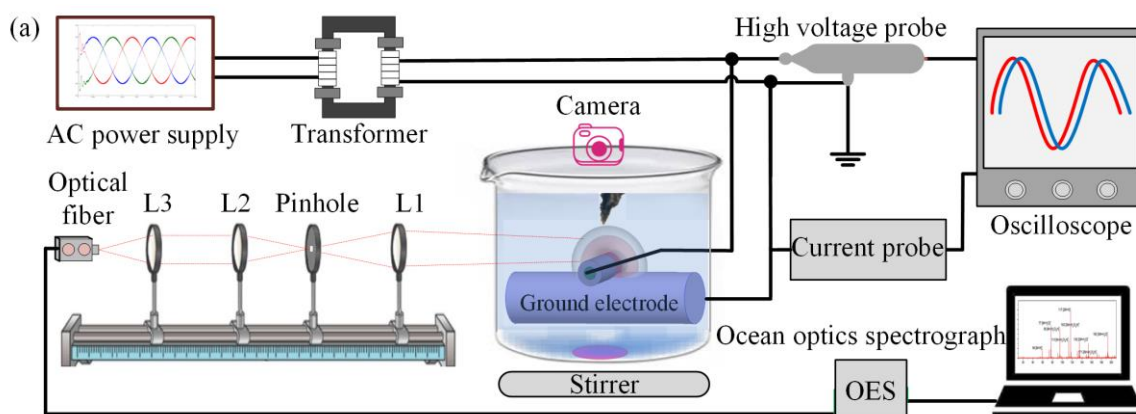
### 5.2.2 Synthesis process and product characterization

The synthesis of NG via the solution plasma was conducted by utilizing 150 ml of a mixed organic solution with 50 wt% benzene ( $C_6H_6$ , >99.5%, Kanto Chemical Co., Inc, Japan) and 50 wt% *N,N*-dimethylformamide (DMF, >99.5%,  $C_3H_7NO$ , Kanto Chemical Co., Inc, Japan). The characteristics of the plasma under a criss-cross system focusing on electrical, optical, discharge mode, and morphological properties were investigated. The discharge was conducted in the solution for 15 minutes with an applied voltage of 1.6 kV, a frequency of 180 kHz, and a pulse width of 1  $\mu$ s. After the solution plasma, black powder product was obtained and collected by vacuum filtration, followed by repeatedly washing by using ethanol to remove the residual organic component and then drying at 80 °C for 8 h in an oven. The conditions of characterization of carbon products, including XRD and Raman, were kept consistent with Chapters 2 to 4. The chemical bonding state of carbon products was performed by X-ray photoelectron spectroscopy (XPS, ULVAC-PHI 5000 VERSAPROBE-II, Inc., Japan) with the X-ray source of Mg Ka. Carbon products' macroscopic scale and morphology were performed by field emission scanning electron microscopy (FE-SEM, JSM-7610F, JEOL Ltd., Japan). The nanoscale of the morphology of the carbon products was performed by transmission electron microscopy (TEM, JEM-2100PLUS JEOL Ltd., Japan). Moreover, the robustness of the electrode system is tested by discharging it in different raw material environments. These raw materials include benzonitrile ( $C_6H_5CN$ ), aniline ( $C_6H_5NH_2$ ), pyridine ( $C_5H_5N$ ), 2-cyanopyridine ( $C_5H_4NCN$ ), 2-aminopyridine ( $C_5H_4NNH_2$ ).





**Figure 5.1.** (a) schematic diagram of the criss-cross system and (b) distribution of electric field in the criss-cross system in organic solution.



**Figure 5.2.** Schematic illustration of the SP experiment arrangement system.

### 5.3 Results and discussion

#### 5.3.1 Solution plasma formation and analysis

In solution plasma, the generation and maintenance of plasma are strongly determined by the electric field distribution, which is a basis of theoretical analysis for the formation of the glow mode of discharge in the organic liquid environment [43, 46]. Herein, the electric field was provided for the discharge under the same excitation (1.6 kV) and environment of the experiment by Ansys Maxwell. The calculation was based on the finite-element analysis, as shown in **Figure 5.1b**. The criss-cross system showed that the strength of the breakdown field

was extremely enough for the generating of the discharge. At the same time, the seed electrons were found to be essential in high-frequency discharge [47]. In general, the density of the electron avalanche is determined by the density of seed electrons [48]. In this system, there were several seed electron sources, including (i) donation from the metal electrode or the ions existing in the solution environment by the effect of the electric field, (ii) free electrons existing in the solution environment [49]. In the typical solution plasma, the electrode structure is a pin-to-pin system. The main source of seed electrons was reported to be only from the metal electrodes, which could be overwhelmingly extracted, due to the bare surface of the metal, resulting in a strong electric field. In contrast, the criss-cross system had a barrier, a ceramic tube, on the metal surface to block the electron extracted in the electric field. Consequently, the source of seed electrons in the criss-cross system became the bulk solution, and the amount was extremely less than that the metal provided. As a result, the density of electron avalanche could be inhibited, which was the key to avoiding the streamer transition. Moreover, it can be found that the electric field was slowly diminished in the gap of the electrodes, as shown in **Figure 5.1b**. It provided the formation of discharge from the contact space at first. The pre-discharge in the micro space provided the seed electron to the further far position of the space by the effect of drift and diffusion, resulting in a uniform discharge distribution with a large scale [50]. The above analysis proved that the stable glow discharge is obtained in the criss-cross system based on forming a moderate growth of electron avalanche in the dielectric barrier electrode structure. Therefore, the solution plasma generated in the criss-cross system can continuously proceed at a stable state and avoid the evaporation of light element, *i.e.*, nitrogen atom, to create a high potential of producing high N-containing carbon products.

The plasma characteristics generated from the criss-cross system were investigated, as shown in **Figure 5.3**, including morphological, optical, and electrical characterization. The emergence and annihilation of the solution plasma by pseudo-color images with the observation in space and time were conducted, as shown in **Figure 5.3a**. The discharge was first generated from the upper half of the electrode, which was covered by a ceramic tube at 125  $\mu\text{s}$ . The discharge spread downstream to the lower half of the electrode, and the maximum scale of the plasma was reached at 250  $\mu\text{s}$ . Then, the upper half plasma gradually became weaker, while the lower half continued to increase the density at 375  $\mu\text{s}$ . It could imply that the solution plasma generated from the criss-cross system had good uniformity. The spatial scale of plasma was up to  $3 \times 16$  mm, and it can be considered as one kind of larger-scale discharge compared with typical discharge generated by the pin-to-pin electrode. In addition, the erosion of metal electrodes was not found even after 15 minutes of the discharge by the criss-cross system. It could mean that the discharge could avoid excessive energy in the criss-cross system.

The schematic diagram of the configuration of generated plasma is shown in **Figure 5.3b**. The plasma phase was existed by surrounding the electrode surface, enclosed by the gas phase and liquid phase in order. Therefore, the interfaces were formed by means of plasma-gas and gas-liquid. In the plasma phase, there was a large number of active particles, *i.e.*, ions, radicals, electrons, and so on [51]. The continuous replenishment of secondary electrons was important for forming the self-maintained solution plasma discharge [52]. According to the  $\gamma$  effect that showed in Chapter 3, the collision reaction between ions and molecules of the raw materials continuously occurred to provide enough amount of secondary electrons at the plasma-liquid interface [28]. The cationic benzene ring could be produced to act as exciting fragments for the polymerization of the carbon framework. Furthermore, the emission of the excited

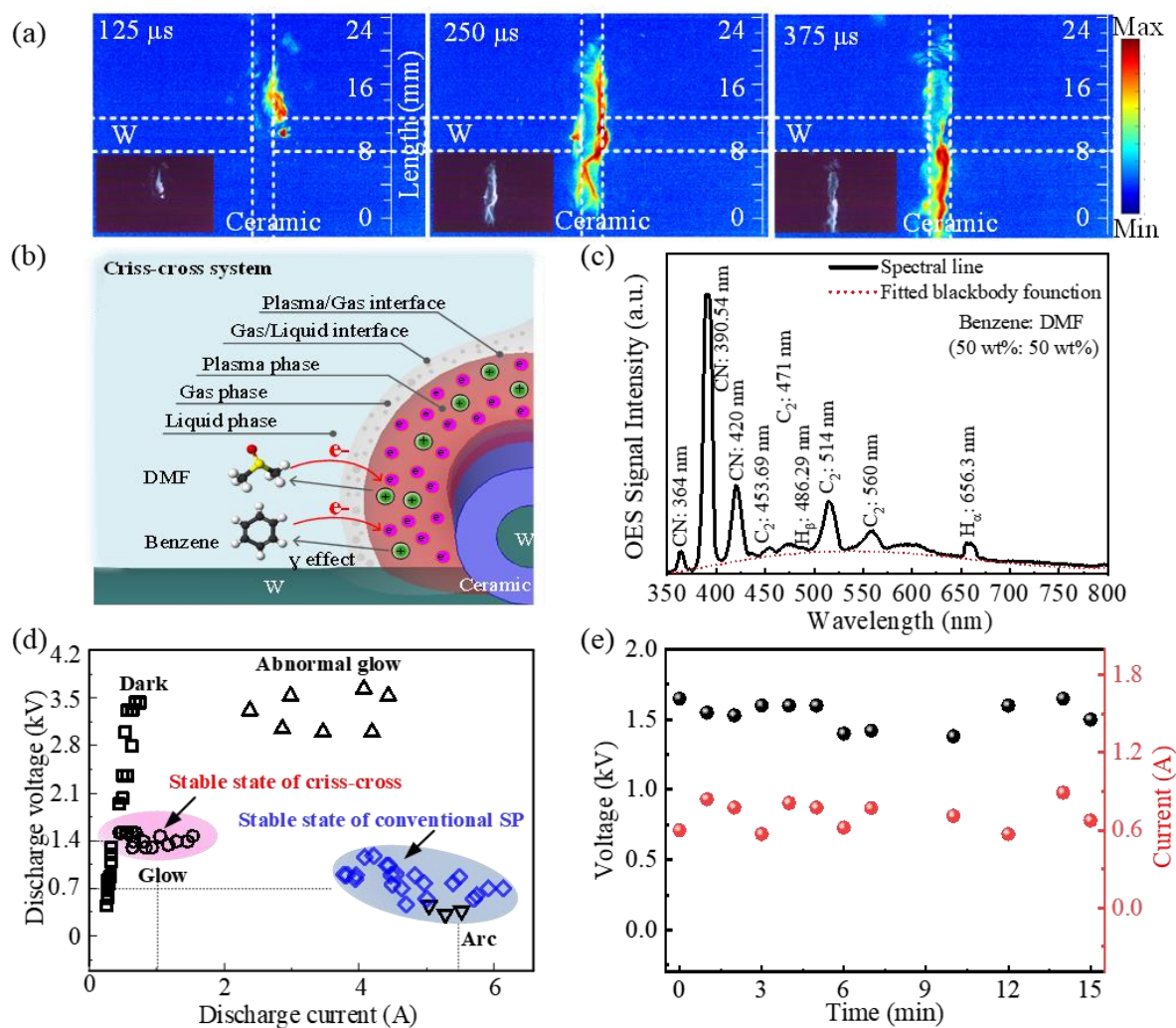
chemical species was detected by SR-OES, as shown in **Figure 5.3c**. The emission peaks, which exhibited  $C_2^*$ , and  $CN^*$  radicals, were continuous radiation bands and can represent the decomposition of organic solution. According to the categorization of OES patterns from Chapter 2, the CN domination could be confirmed in the plasma reaction field formed in the criss-cross system, which referred that the high nitrogen-containing carbon products should be obtained.

The black-body temperature ( $T_b$ ), which indicates the heavy particles' temperature, was calculated by assuming the plasma reaction field has the local thermal equilibrium (LET) on the foundation of Plank's theory. In the typical solution plasma, the  $T_b$  was previously reported to be higher than 4000 K [28]. Meanwhile, the  $T_b$  calculated from the emission pattern of the discharge in the criss-cross system was around 2505 K. It could imply that the discharge mode of the criss-cross system was stabilized in the glow type. At the same time, due to the IE (ionization energy) of DMF ( $9.12 \pm 0.02$  eV) being lower than that of benzene ( $9.25 \pm 0.07$  eV), according to the NIST database, it could be suggested that the  $CN^*$  radicals were generated from the decomposition of DMF. The ring structure of benzene could be preserved in the process of collision at the plasma-liquid interface, which was important for the polymerization reaction.

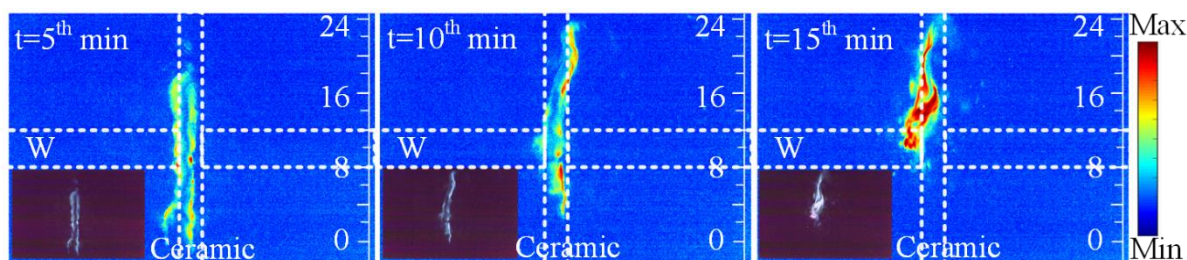
**Figure 5.3d** shows the V-I characteristics of the discharge from a criss-cross system in the liquid environment of the mixture of benzene and DMF. The discharge was gradually generated from the dark plasma mode; no light emission was observed, and it only produced a relatively small current that was detected by the oscilloscope. The breakdown occurred after the appearance of numerous bubbles that were produced from electrolysis and Joule heating. After that, the glow mode of the discharge was transferred. The current was tiny, changed from 0.32 A to 1.68 A; however, the voltage of the plasma did not fluctuate. When the

discharge current continued to increase, the abnormal glow mode and arc mode were shown, respectively. The current range of the glow mode was relatively wide, which meant that the discharge could be stable in the glowing state. Compared with the typical solution plasma, the stable state of the criss-cross system was shown at a lower discharge current. It implied that the reaction field had a lower energy, resulting in preventing the evaporation of the nitrogen atoms and remaining in the carbon framework by forming  $sp^2$  bonding structure via polymerization. Moreover, by prolonging the discharge up to 15 mins, a slight change in V-I and discharge image could be observed, as shown in **Figure 5.3e** and **Figure 5.4**. There was a slight fluctuation of the voltage and current, and a uniform distributed plasma was exhibited. Therefore, it could indicate that the criss-cross system could generate a plasma that stabilizes in glow mode with good stability.

Moreover, the influence of raw materials was also investigated to find the reliability of the proposed system in the Chapter. The other ring molecules, including benzonitrile (IE = 9.60), aniline (IE = 8.45), pyridine (IE = 9.25), 2-cyanopyridine (IE = 9.58), and 2-aminopyridine (IE = 9.30) were also selected as raw materials. Almost all the IE values of the raw materials are higher than that of DMF, which means the ring structures of the raw molecules can also be kept the same as the benzene of the above proposed to support the polymerization reaction of the carbon formation.



**Figure 5.2.** The plasma morphological, optical, and electrical properties of the glow discharge under a criss-cross system in the precursor of a mixture of benzene and DMF: (a) plasma spatial distribution properties by digital image (expose time was 125  $\mu\text{s}$ ) and the converted pseudo-color image (Scale: Light intensity) in space and time; (b) schematic diagram of the plasma configuration; (c) SROES spectrum of the glow discharge; (d) V–I characteristics indicating plasma modes (dark, glow, abnormal glow, and arc) transition (50 measurements of voltage and current in various modes), and the stable state of discharge in both the systems of criss-cross and conventional SP; (e) state of the glow discharge by voltage and current variations in 15 mins.



**Figure 5.4.** The record of discharge stare by digital images (expose time was 125  $\mu$ s) with the converted pseudo-color images at the fifth, tenth, and fifteenth minutes.

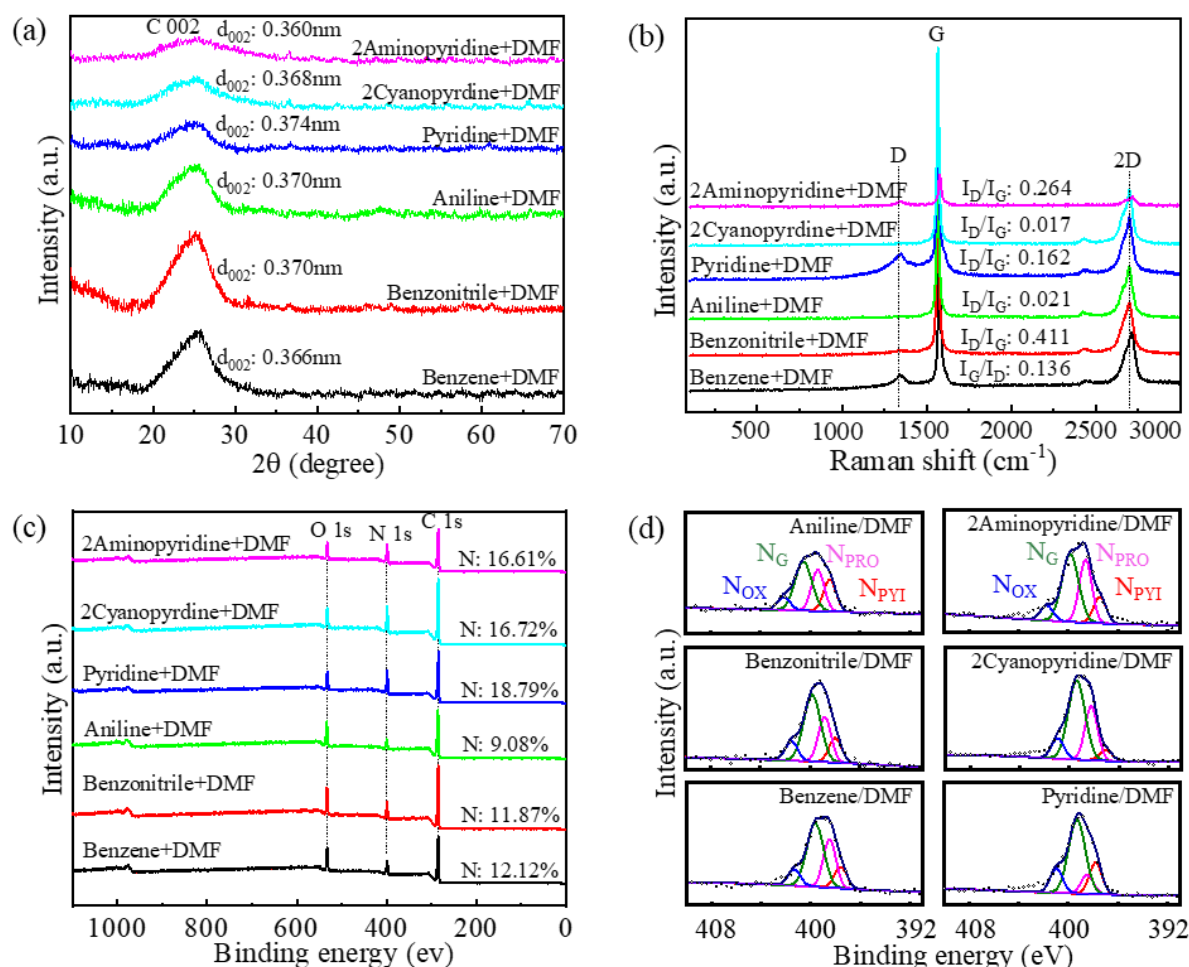
### 5.3.2 Product characterization

The carbon products produced by the criss-cross system were also well-characterized. The influences of the raw materials (*i.e.*, benzene/DMF, benzonitrile/DMF, aniline/DMF, pyridine/DMF, 2-cyanopyridine/DMF, and 2-aminopyridine/DMF) and the power sources conditions (*i.e.*, frequencies and discharge times) were also studied. The structure analysis of the products was investigated by XRD, as shown in **Figure 5.5a**. A characteristic broad peak was found at around  $23.5^\circ$ , which corresponds to (002) crystal plane of carbon. Besides, it could be observed in the XRD pattern of all the carbon synthesized from the criss-cross system [27, 53]. The calculated lattice spacing ( $d_{002}$ ) is shown in **Table 5.1**. It showed that the carbon products have a larger 002 lattice spacing than that of pristine graphite (0.335 nm) [21].

Furthermore, the Raman spectroscopy of the products was conducted to collect information on layer number, N doping bonding configuration (in-plane, edge, function group), and other electronic structures through vibrational and rotational states of the molecular system, as the results of Raman spectra, **Figure 5.5b**, the characteristic peaks of D band ( $\sim 1340\text{ cm}^{-1}$ ), G band ( $\sim 1580\text{ cm}^{-1}$ ), the 2D band ( $\sim 2710\text{ cm}^{-1}$ ) were found [22-24]. The G band of all the carbon products exhibited extremely strong intensity. However, the intensity of D band from the products was weak. Generally, both D and G bands are attributed to the

$sp^2$ -bonded C atoms with a vibrations state. However, G band indicates the existence of the basic  $sp^2$  lattice C atoms [21, 51], while D band is attributed to the breathing oscillation of hexagonal carbon lattice, and it can be forbidden in a perfect symmetry structure. The D band also relates to the increase of polarizability in the carbon lattice, which can be occurred for several reasons, including the introduction of heteroatoms or the defects, edges, and functional groups [54]. Moreover, the ratio of D and G peak intensities ( $I_D/I_G$ ) was calculated (**Table 5.1**), which has been reported to refer to the degree of polarizability changing and graphitization. The  $I_D/I_G$  values of carbon synthesized from benzene/DMF, benzonitrile/DMF, aniline/DMF, pyridine/DMF, 2-cyanopyridine/DMF, and 2-aminopyridine/DMF were 0.136, 0.037, 0.021, 0.162, 0.017, and 0.264 nm, respectively. The carbon from benzonitrile/DMF, aniline/DMF, and 2-cyanopyridine /DMF had a relative low  $I_D/I_G$ , which could refer to the weak delocalization of electron density of the electronic surface potential in  $sp^2$ -hybridized carbon. Based on the Tuinstra-Koenig relation [55], the crystallite size ( $L_a$ ) of the carbon products was calculated (**Table 5.1**). Meanwhile, all the carbon that was synthesized shows a strong intensity of 2D peak. Generally, to say, the  $I_{2D}/I_G$  is a second order of the index that can be resulted from the defect of carbon [12, 24, 29]. As the results are shown in **Table 5.1**, all the carbon products were multilayer graphene with a relative great framework [12, 21, 51].

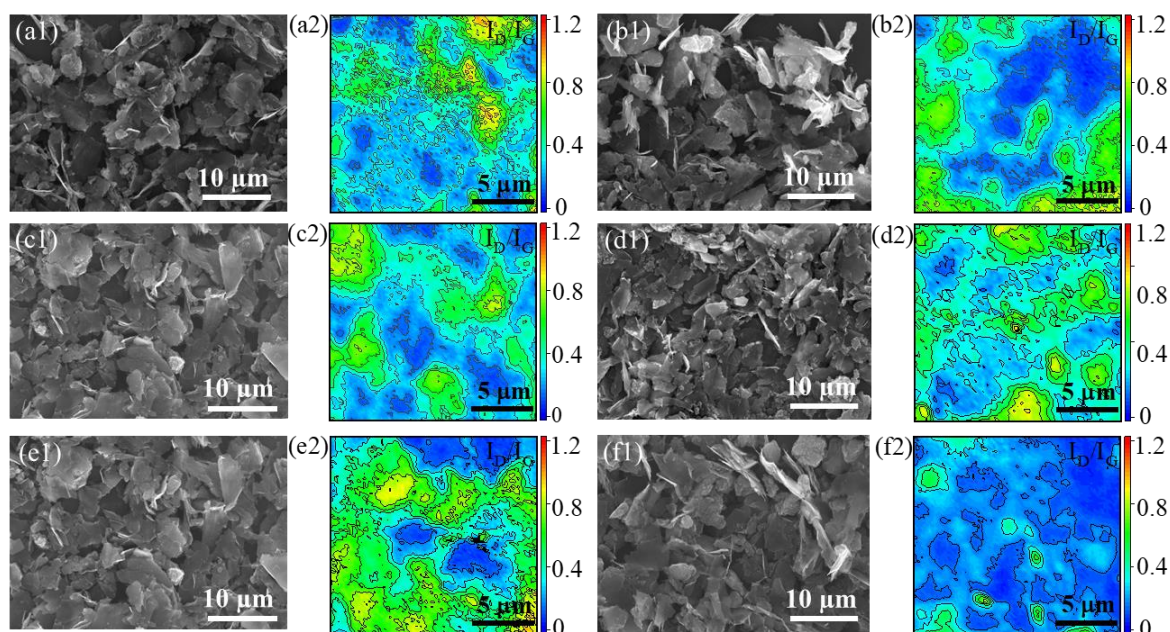




**Figure 5.5** Characterization of products synthesized by the criss-cross system from benzene/DMF, benzonitrile/DMF, aniline/DMF, pyridine/DMF, 2-cyanopyridine/DMF, and 2-aminopyridine/DMF including (a) X-ray diffraction (XRD) patterns; (b) Raman spectra; (c) XPS spectra; (d) high-resolution XPS N 1s spectra with deconvolution and peak assignments ( $N_{OX}$ : oxidized N,  $N_G$ : graphitic N,  $N_{PRO}$ : pyrrolic N and  $N_{PYI}$ : pyridinic N).

The morphology and uniformity of NG products synthesized from the criss-cross system were further investigated by the SEM and mapping of Raman, as shown in **Figure 5.6**, respectively. It was found that all NG products exhibited sheet-like layered structures, similar to the multi-layer graphite synthesized from the microwave-assisted solvothermal method and so on [56]. The average size of carbon products synthesized in this research was at the level of several hundred nanometers to a few micrometers. The Raman mapping results indicated

that all the carbon products exhibited  $I_D/I_G$  values lower than 0.5, referring to fewer defects and excellent uniformity.



**Fig. 5.6** SEM images and Raman mappings ( $16\ \mu\text{m}\times 16\ \mu\text{m}$  of measurement area with  $0.2\ \mu\text{m}$  of the scan step, a total of 6561 measuring points of one sample) of  $I_D/I_G$  of products synthesized by the criss-cross system: (a) benzene/DMF; (b) benzonitrile/DMF; (c) aniline/DMF; (d) pyridine/DMF; (e) 2-cyanopyridine/DMF; and (f) 2-aminopyridine/DMF.

Furthermore, the chemical composition and bonding configuration of nitrogen of the obtained NG were investigated by the XPS, as shown in **Table 5.1**. The nitrogen contents of the product obtained from benzene/DMF, benzonitrile/DMF, aniline/DMF, pyridine/DMF, 2-cyanopyridine/DMF, and 2-aminopyridine/DMF were 12.12, 11.87, 9.08, 18.79, 16.72 and 16.61 at. %, respectively. The relatively high nitrogen-containing carbon products could be synthesized by the glow plasma that is generated from the criss-cross system. The XPS survey spectra revealed the presence of carbon (C 1s), oxygen (O 1s), and nitrogen (N 1s) signals without any other impurities (**Figure 5.5c**). High-resolution N 1s, along with the deconvoluted peaks of the obtained product, are shown in **Figure 5.5d**. The deconvoluted peaks in the N1

s spectra could be identified to be pyridinic N ( $398.0 \pm 0.5$  eV), pyrrolic N ( $399.1 \pm 0.5$  eV), graphitic or quaternary N ( $400.1 \pm 0.6$  eV), and oxidized N ( $402.0 \pm 0.5$  eV). The peak of graphitic-N was observed to be a major peak in all products at an average percentage of 50.3 %.

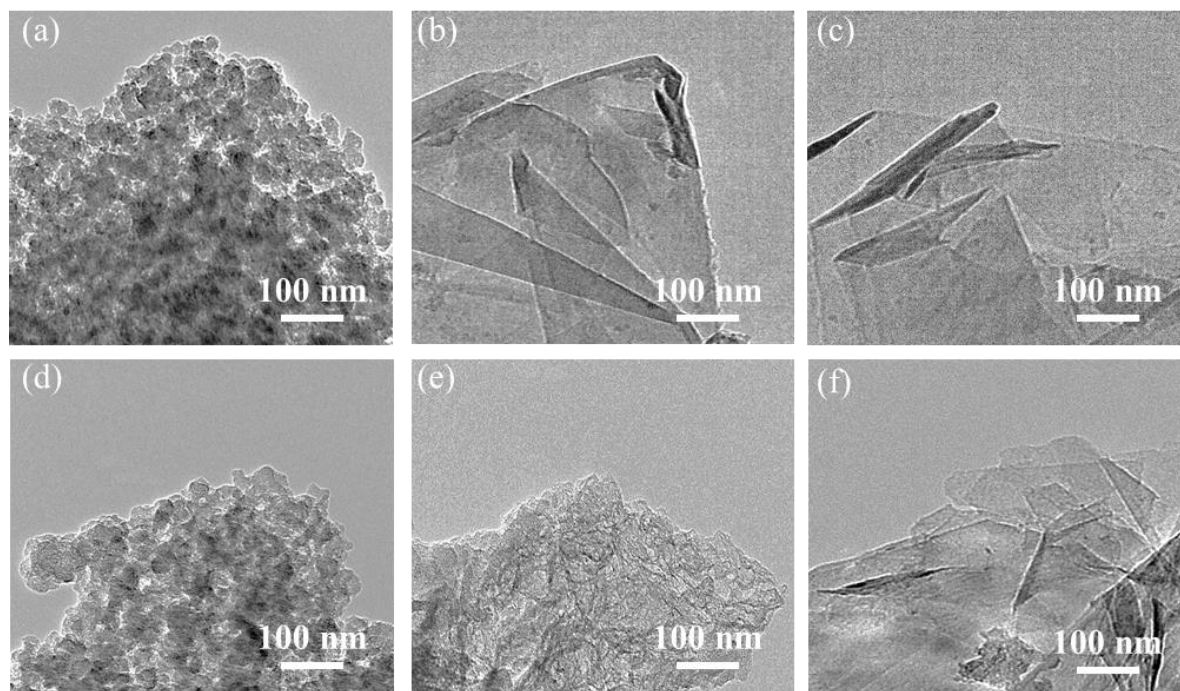
**Table 5.1** The calculated lattice spacing at (002) carbon planes ( $d_{002}$ ) from XRD patterns; intensity ratio of D and G bands ( $I_D/I_G$ ), the intensity ratio of 2D and G bands ( $I_{2D}/I_G$ ), and crystallite size ( $L_a$ ) from Raman spectroscopy; element compositions and the percentage of the deconvoluted peaks in high-resolution N1 s from XPS measurement of the obtained carbons from various systems via SP.

	XRD	Raman			XPS						
	$d_{002}$	$I_D/I_G$	$I_{2D}/I_G$	$L_a$ (nm)	Composition (at. %)			N 1s (%) *			
					C	O	N	$N_{PYI}$	$N_{PRO}$	$N_G$	$N_{OX}$
benzene/DMF	0.366	0.136	0.182	141.11	73.68	14.21	12.12	12.6	28.2	49.7	9.5
benzotrile/DMF	0.370	0.037	0.314	468.32	73.82	14.31	11.87	13.8	25.4	50.1	10.7
aniline/ DMF	0.370	0.021	0.269	906.82	74.84	16.08	9.08	21.0	27.2	43.2	8.7
pyridine/ DMF	0.374	0.162	0.159	118.42	70.61	10.6	18.79	18.2	10.8	56.9	14.1
2-cyanopyridine/ DMF	0.368	0.017	0.284	1104.23	72.96	10.32	16.72	5.7	28.3	55.4	10.6
2-aminopyridine/ DMF	0.360	0.264	0.398	72.86	72.28	11.1	16.61	13.6	32.3	46.4	7.7

(Note: \*Doping concentration = atomic ratio $\times$ 100,  $N_{PYI}$ ,  $N_{PRO}$ ,  $N_G$ , and  $N_{OX}$  refer to pyridinic N, pyrrolic N, graphitic N, and oxidized N, respectively)

Fine morphology of the NG products was also obtained by typical TEM images, as shown in **Figure 5.7**. In general, it has been reported that the NG exhibited a thin planar structure with a moderate number of wrinkles [57-59]. In this work, the obtained NG products from the discharge of benzonitrile/DMF, aniline/DMF, and 2-aminopyridine/DMF (**Figure 5.7b, c, f**)

were found to contain wrinkles slightly. According to the previous reports, generally, the carbon atom has four valence electrons which can form a planar hexagonal structure with  $sp^2$  hybridization. However, the presence of a nitrogen atom with five valence electrons in the carbon framework can cause a repulsive interaction, leading to the out-of-plane relaxation of carbon atoms in graphene and deteriorating the planar structure [21, 60]. In this work, the obtained products contained quite a large amount of graphitic nitrogen configuration, which has similar characteristics to carbon atoms (three hybridized  $sp^2$  orbitals). Therefore, it could retain the planar structure of graphene, which might lead to reducing the appearance of wrinkles. The NG products from the discharge in benzene/DMF and pyridine/DMF (**Figure 5.7a, d**) revealed randomly aggregated irregularly thicker sheet structures. As mentioned before, both precursors have similar molecular structures and IE. Accordingly, it tended to have the carbonation of molecules simultaneously occur with the polymerization process under the reaction field of the plasma. It can suggest that different precursors have a more significant influence on the surface morphology, microstructure, and thickness of the final product.



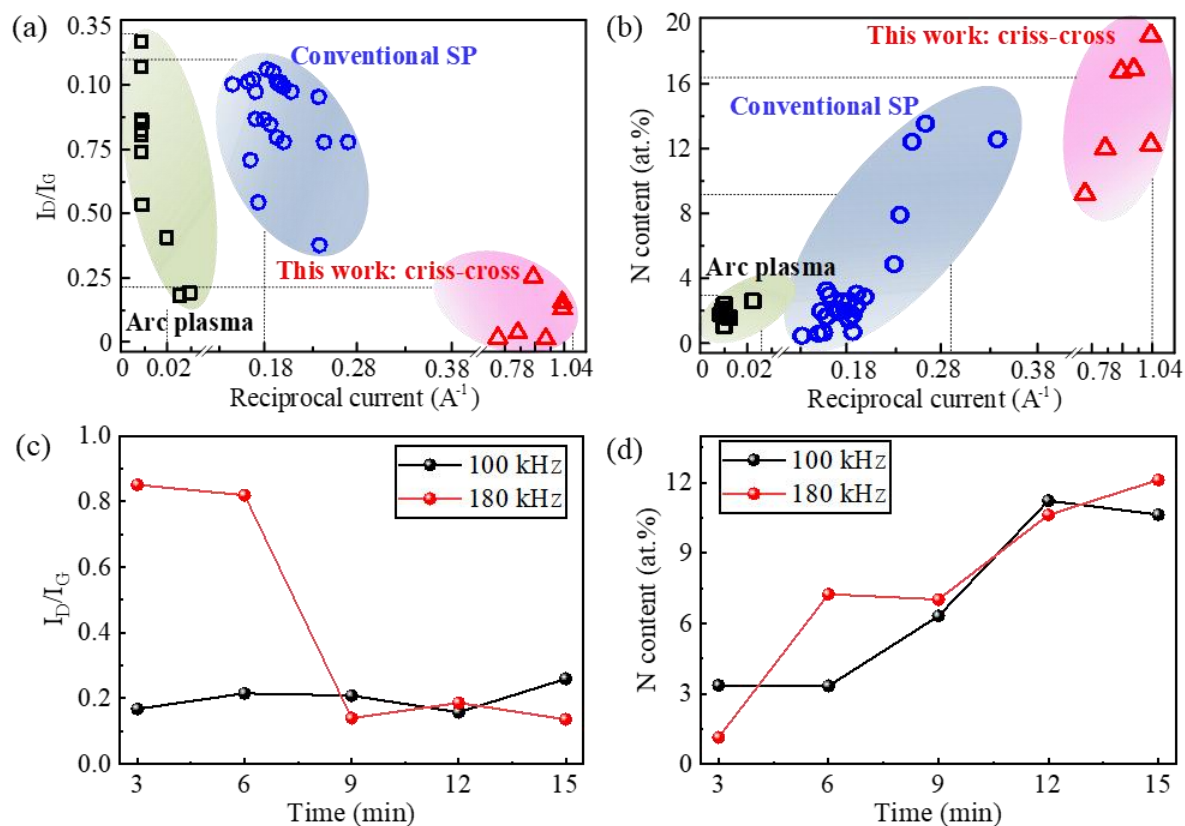
**Figure 5.7** TEM images of NG products synthesized by the criss-cross system from different precursors: (a) benzene/DMF; (b) benzonitrile/DMF; (c) aniline/DMF; (d) pyridine/DMF; (e) 2-cyanopyridine/DMF, and (f) 2-aminopyridine/DMF.

To further understand the relationship between NG and plasma characteristics, the plot between  $I_D/I_G$  and the inverse of the plasma current was conducted, as shown in **Figure 5.8a**. Current is a characteristic parameter of the reaction rate in liquid-phase plasma. Typical solution plasma could reduce the current, compared to arc plasma, resulting in a lowering  $I_D/I_G$  ratio (The detailed information of raw data is provided in the supporting data **Table S1** and **S2**). However, the criss-cross system proposed in this study can achieve stable glow discharges at the milliamp level. Due to current levels, electrons in  $\pi$ -conjugated bonding orbitals were excited to  $\pi$ -conjugated antibonding orbitals, and the ring structure of precursors could be mainly preserved. In this work, plasma with a lower current can contribute to the polymerization reaction and act as the key to achieving an excellent carbon framework. **Figure 5.8b** shows the relationship between doping concentration and the inverse of the

current. Compared to arc and the typical solution plasma, the appearance of a single dielectric barrier of a criss-cross system suppressed the ion acceleration and inhibited the rise of plasma bulk temperature. As a result, the light element, like nitrogen, was preserved from evaporation during the discharge, which significantly improved heteroatom doping. Moreover, different discharge conditions (*i.e.*, discharge times and frequencies) were further investigated to indicate their influences on the altering of  $I_D/I_G$  and nitrogen contents of the products. The results are shown in **Figures 5.8c** and **d**. It could suggest that the discharge time showed no significant effect on  $I_D/I_G$  after the 100-kHz discharge (**Figure 5.8c**). However, for the 180-kHz discharge, the  $I_D/I_G$  decreased as prolonging the discharge time. In addition, it was found that the N content gradually increased as increasing the discharge time. There was no strong correlation between the discharge frequency and the nitrogen content in the obtained products. It can suggest that structural property is mainly dependent on the operating frequency, referring to the input energy [25]. Meanwhile, the heteroatom doping content was influenced by the reaction time, which can imply that the doping content was affected by the number of precursors that reacted.






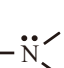
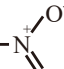
The nitrogen doping in the g-NG was found to be significantly high amount, *i.e.*, up to 18.79 at. %, relatively low  $I_D/I_G$  ranging from 0.017 to 0.264, and large  $L_a$ , compared to that obtained from other methods, as shown in **Figure 5.9a** and **Fig. S8**, respectively. The low values of  $I_D/I_G$  indicated that the bonding configurations of the obtained g-NG had slightly changed in the polarizability of vibrational modes, referring to achieving a good planar structure or carbon framework. Generally, when nitrogen atoms are incorporated by other methods in the carbon framework, a significant change in polarizability can be observed [8, 61]. The bonding configuration and sheet size significantly affect the polarizability of the

surface electronic potential of the material. The possible effect of  $I_D$ ,  $I_G$ , and  $I_D/I_G$  from the above factors are shown in supporting information in **Table 5.2** in detail.



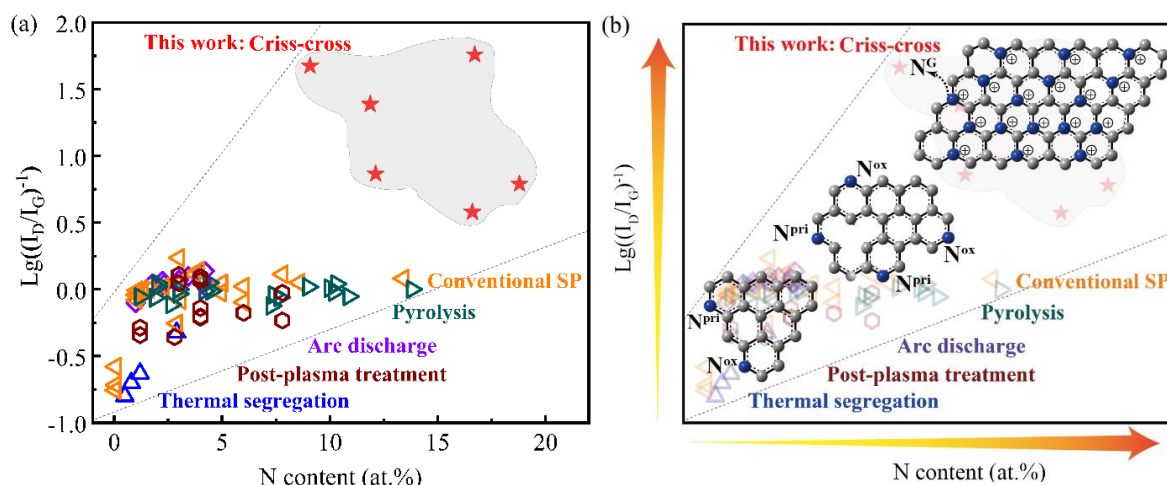
**Figure 5.8** Correlation of in-liquid plasma parameters and carbon products properties: (a)  $I_D/I_G$  vs. reciprocal current and (b) N content vs. reciprocal current for conventional arc plasma, typical solution plasma, and the criss-cross solution plasma, proposed in this work; (c), (d) changing of  $I_D/I_G$  and N content by discharge time and discharge frequency in the same organic precursor (*i.e.*, benzene/DMF).

**Table 5.2** The possible nitrogen bonding configuration and their effect of  $I_D$ ,  $I_G$  and  $I_D/I_G$ .

C/N/Shape	Assignment	Bonding denoted	Bonding descriptor	$sp^2/sp^3$	$I_D$	$I_G$	$I_D/I_G$
C	Graphite	Graphitic carbon	$C=C$	$sp^2 C$	$\rightarrow$	$\rightarrow$	$\rightarrow$
		Carbon bonded to N in graphitic, pyridinic, pyrrolic	$C_{sp^2}-N$	$sp^2 C$	$\uparrow$	$\downarrow$	$\uparrow$
		Quaternary N in aromatics	$C_{sp^3}-N$	$sp^3 C$	$\uparrow$	$\downarrow$	$\uparrow$
		Carbon bonded with Hydroxyl	$C-OH$	$sp^3 C$	$\uparrow$	$\downarrow$	$\uparrow$
		Carbon bonded with Carboxyl	$C=O$	$sp^2 C$	$\uparrow$	$\downarrow$	$\uparrow$
N	Chemical bond state	Graphite N		Basal $sp^2 N$	$\downarrow$	$\rightarrow$	$\downarrow$
		Quaternary N		Basal $sp^3 N$	$\uparrow$	$\downarrow$	$\uparrow$
		Pyridinic N		Edge $sp^2 N$	$\uparrow$	$\downarrow$	$\uparrow$
		Pyrrolic N		Edge $sp^2 N$	$\uparrow$	$\downarrow$	$\uparrow$
		Pyridinic oxidized N		Edge $sp^2 N$	$\uparrow$	$\downarrow$	$\uparrow$
		Amino		Edge $sp^3 N$	$\uparrow$	$\downarrow$	$\uparrow$
		Nitrile	$-C\equiv\ddot{N}$	Edge $sp N$	$\uparrow$	$\downarrow$	$\uparrow$
Shape	Plane size	Nitro		Edge $sp^3 N$	$\uparrow$	$\downarrow$	$\uparrow$
		Large	Small ratio of edge/Plane		$\downarrow$	$\rightarrow$	$\downarrow$
		Small	Large ratio of edge/plane		$\uparrow$	$\rightarrow$	$\uparrow$



The ability to change polarizability follows the order: function group > pyridinic oxidized nitrogen > pyridinic nitrogen > pyrrolic nitrogen > graphitic nitrogen. Functional groups normally can withdraw or donate electrons to the  $\pi$ -conjugated bonding orbitals [61]. The large functional group shows the highest effect on the polarizability of the material. For example, oxygen has a high electron affinity; therefore, the pyridinic oxidized nitrogen strongly influences the polarizability compared to the pyridinic nitrogen. It is also worth noting that the lone pair electrons of pyrrolic nitrogen are in unhybridized  $p$  orbitals to conjugate with the carbon, resulting in  $\pi$ -conjugated bonding orbitals. But the lone pair electrons of pyridinic nitrogen are in  $sp^2$  hybridized orbitals, which are not involved in the  $\pi$ -conjugated bonding orbitals. Thus, the ability to change the polarizability of pyrrolic nitrogen is weaker than pyridinic nitrogen. Meanwhile, graphitic nitrogen can act like a carbon atom with four valence electrons, and the lone pair electrons also conjugate with  $\pi$  bonding orbitals. Therefore, graphitic nitrogen shows the weakest changing polarizability [62]. Accordingly, it is referred that the high graphitic carbon framework with high nitrogen doping level could be synthesized by the criss-cross system, which is solution plasma with low energy. To simply illustrate, all methods, which are mainly used to synthesize NG for energy applications reported in previous research, are shown in **Figure 5.9b**. The solution plasma with a criss-cross system can succeed in obtaining the graphene with a larger planar structure and higher doping content compared to other methods. As the obtained evidence, the obtained product in this work had a high potential for further development and utilization in energy applications.



**Figure 5.9** (a)  $I_D/I_G$  to nitrogen content comparison of the characteristics of carbons (total 78 references) synthesized in this study and those obtained by various other technologies, which include thermal segregation, arc discharge, conventional solution plasma, pyrolysis, and post plasma treatment and (b) schematic diagram of the change in size and doping components of the carbon products.

#### 5.4. Conclusions

In this Chapter, the modified solution plasma with the criss-cross electrode configuration was proposed based on the correlations obtained from Chapter 2 through Chapter 4, which utilized the concept of dielectric barrier discharge, was proposed for the first time to synthesize carbon materials with high nitrogen-containing. The obtained plasma with high stability of glow discharge could constantly keep the lower current state and achieve the OES of CN radical domination. The raw materials with aromatic ring structure could facilitate the polymerization of ring N containing intermediates via electron transfer reaction. Owing to the suppression of excessive energy in the reaction field, the proposed system significantly improved the doping amount of graphitic N into the in-plane carbon lattice. According to the obtained evidence, this study could provide the final answer to regulate the plasma-chemical

reactions, which can be applied to the synthesis of high-quality carbon materials with high nitrogen-containing through the solution plasma.

## References

1. Inagaki, M.; Kim, Y.A.; Endo, M. Graphene: Preparation and structural perfection. *J. Mater. Chem.* **2011**, *21*, 3280-3294.
2. Chen, Y.; Xie, B.; Ren, Y.; Yu, M.; Qu, Y.; Xie, T.; Zhang, Y.; Wu, Y. Designed nitrogen doping of few-layer graphene functionalized by selective oxygenic groups. *Nanoscale Research Letters* **2014**, *9*, 646.
3. Wang, H.; Maiyalagan, T.; Wang, X. Review on recent progress in nitrogen-doped graphene: Synthesis, characterization, and its potential applications. *ACS Catalysis* **2012**, *2*, 781-794.
4. Hadadian, M.; Correa-Baena, J.P.; Goharshadi, E.K.; Ummadisingu, A.; Seo, J.Y.; Luo, J.; Gholipour, S.; Zakeeruddin, S.M.; Saliba, M.; Abate, A., *et al.* Enhancing efficiency of perovskite solar cells via n-doped graphene: Crystal modification and surface passivation. *Adv Mater* **2016**, *28*, 8681-8686.
5. Mehetre, S.S.; Maktedar, S.S.; Singh, M. Understanding the mechanism of surface modification through enhanced thermal and electrochemical stabilities of n-doped graphene oxide. *Applied Surface Science* **2016**, *366*, 514-522.
6. Tian, K.; Wang, J.; Cao, L.; Yang, W.; Guo, W.; Liu, S.; Li, W.; Wang, F.; Li, X.; Xu, Z., *et al.* Single-site pyrrolic-nitrogen-doped sp(2)-hybridized carbon materials and their pseudocapacitance. *Nat Commun* **2020**, *11*, 3884.
7. Li, J.; Li, X.; Zhao, P.; Lei, D.Y.; Li, W.; Bai, J.; Ren, Z.; Xu, X. Searching for magnetism in pyrrolic n-doped graphene synthesized via hydrothermal reaction. *Carbon* **2015**, *84*, 460-468.
8. Liu, J.; Li, Q.; Zou, Y.; Qian, Q.; Jin, Y.; Li, G.; Jiang, K.; Fan, S. The dependence of graphene raman d-band on carrier density. *Nano Lett* **2013**, *13*, 6170-6175.
9. Lee, H.; Paeng, K.; Kim, I.S. A review of doping modulation in graphene. *Synthetic Metals* **2018**,

244, 36-47.

10. Guo, B.; Fang, L.; Zhang, B.; Gong, J.R. Graphene doping: A review. *Insciences Journal* **2011**, 80-89.
11. Salinas-Torres, D.; Navlani-García, M.; Mori, K.; Kuwahara, Y.; Yamashita, H. Nitrogen-doped carbon materials as a promising platform toward the efficient catalysis for hydrogen generation. *Applied Catalysis A: General* **2019**, 571, 25-41.
12. Hyun, K.; Saito, N. The solution plasma process for heteroatom-carbon nanosheets: The role of precursors. *Sci Rep* **2017**, 7, 3825.
13. Li, O.L.; Shi, Z.; Lee, H.; Ishizaki, T. Enhanced electrocatalytic stability of platinum nanoparticles supported on sulfur-doped carbon using in-situ solution plasma. *Sci Rep* **2019**, 9, 12704.
14. Kang, J.; Kim, Y.; Kim, H.M.; Hu, X.; Saito, N.; Choi, J.H.; Lee, M.H. In-situ one-step synthesis of carbon-encapsulated naked magnetic metal nanoparticles conducted without additional reductants and agents. *Sci Rep* **2016**, 6, 38652.
15. Garland, N.A.; Boyle, G.J.; Cocks, D.G.; White, R.D. Approximating the nonlinear density dependence of electron transport coefficients and scattering rates across the gas-liquid interface. *Plasma Sources Science and Technology* **2018**, 27, 024002.
16. Hsieh, K.C.; Wandell, R.J.; Bresch, S.; Locke, B.R. Analysis of hydroxyl radical formation in a gas-liquid electrical discharge plasma reactor utilizing liquid and gaseous radical scavengers. *Plasma Processes and Polymers* **2017**, 14.
17. Estifae, P.; Su, X.; Yannam, S.K.; Rogers, S.; Thagard, S.M. Mechanism of e. Coli inactivation by direct-in-liquid electrical discharge plasma in low conductivity solutions. *Sci Rep* **2019**, 9, 2326.
18. Panov, V.A.; Vasilyak, L.M.; Vetchinin, S.P.; Pecherkin, V.Y.; Son, E.E. Pulsed electrical discharge in conductive solution. *Journal of Physics D: Applied Physics* **2016**, 49.
19. Kang, J.; Li, O.L.; Saito, N. A simple synthesis method for nano-metal catalyst supported on mesoporous carbon: The solution plasma process. *Nanoscale* **2013**, 5, 6874-6882.

20. Pootawang, P.; Saito, N.; Lee, S.Y. Discharge time dependence of a solution plasma process for colloidal copper nanoparticle synthesis and particle characteristics. *Nanotechnology* **2013**, *24*, 055604.
21. Chae, S.; Panomsuwan, G.; Bratescu, M.A.; Teshima, K.; Saito, N. P-type doping of graphene with cationic nitrogen. *ACS Applied Nano Materials* **2019**, *2*, 1350-1355.
22. Phan, P.Q.; Chae, S.; Pornaroontham, P.; Muta, Y.; Kim, K.; Wang, X.; Saito, N. In situ synthesis of copper nanoparticles encapsulated by nitrogen-doped graphene at room temperature via solution plasma. *RSC Advances* **2020**, *10*, 36627-36635.
23. Bratescu, M.A.; Kim, K.; Saito, N. Quantitative spectrochemical analysis of solution plasma in aromatic molecules. *Plasma Processes and Polymers* **2019**, *16*.
24. Panomsuwan, G.; Saito, N.; Ishizaki, T. Nitrogen-doped carbon nanoparticles derived from acrylonitrile plasma for electrochemical oxygen reduction. *Phys Chem Chem Phys* **2015**, *17*, 6227-6232.
25. Kang, J.; Li, O.L.; Saito, N. Synthesis of structure-controlled carbon nano spheres by solution plasma process. *Carbon* **2013**, *60*, 292-298.
26. Kim, D.W.; Li, O.L.; Saito, N. Enhancement of orr catalytic activity by multiple heteroatom-doped carbon materials. *Phys Chem Chem Phys* **2015**, *17*, 407-413.
27. Hyun, K.; Ueno, T.; Panomsuwan, G.; Li, O.L.; Saito, N. Heterocarbon nanosheets incorporating iron phthalocyanine for oxygen reduction reaction in both alkaline and acidic media. *Phys Chem Chem Phys* **2016**, *18*, 10856-10863.
28. Morishita, T.; Ueno, T.; Panomsuwan, G.; Hieda, J.; Yoshida, A.; Bratescu, M.A.; Saito, N. Fastest formation routes of nanocarbons in solution plasma processes. *Sci Rep* **2016**, *6*, 36880.
29. Kim, D.-w.; Li, O.L.; Pootawang, P.; Saito, N. Solution plasma synthesis process of tungsten carbide on n-doped carbon nanocomposite with enhanced catalytic orr activity and durability. *RSC Advances* **2014**, *4*.
30. Hyun, K.; Ueno, T.; Saito, N. Synthesis of nitrogen-containing carbon by solution plasma in aniline with high-repetition frequency discharges. *Japanese Journal of Applied Physics* **2016**, *55*.

31. Lee, S.; Saito, N. Enhancement of nitrogen self-doped nanocarbons electrocatalyst via tune-up solution plasma synthesis. *RSC Advances* **2018**, *8*, 35503-35511.
32. Chae, S.; Bratescu, M.A.; Saito, N. Synthesis of few-layer graphene by peeling graphite flakes via electron exchange in solution plasma. *The Journal of Physical Chemistry C* **2017**, *121*, 23793-23802.
33. Lee, H.; Bratescu, M.A.; Ueno, T.; Saito, N. Solution plasma exfoliation of graphene flakes from graphite electrodes. *RSC Adv.* **2014**, *4*, 51758-51765.
34. Kim, K.; Hashimi, K.; Bratescu, M.A.; Saito, N. The initial reactions from pyridine to hetero-carbon nanomaterials through solution plasma. *Nanoscience and Nanotechnology Letters* **2018**, *10*, 814-819.
35. Heo, Y.K.; Lee, S.H.; Bratescu, M.A.; Kim, S.M.; Lee, G.J.; Saito, N. Generation of non-equilibrium condition in solution plasma discharge using low-pass filter circuit. *Plasma Processes and Polymers* **2016**, *14*.
36. Lee, S.; Heo, Y.; Bratescu, M.A.; Ueno, T.; Saito, N. Solution plasma synthesis of a boron-carbon-nitrogen catalyst with a controllable bond structure. *Phys Chem Chem Phys* **2017**, *19*, 15264-15272.
37. Li, O.L.; Chiba, S.; Wada, Y.; Panomsuwan, G.; Ishizaki, T. Synthesis of graphitic-n and amino-n in nitrogen-doped carbon via a solution plasma process and exploration of their synergic effect for advanced oxygen reduction reaction. *Journal of Materials Chemistry A* **2017**, *5*, 2073-2082.
38. Zhou, R.; Zhou, R.; Alam, D.; Zhang, T.; Li, W.; Xia, Y.; Mai-Prochnow, A.; An, H.; Lovell, E.C.; Masood, H., *et al.* Plasmacatalytic bubbles using ceo<sub>2</sub> for organic pollutant degradation. *Chemical Engineering Journal* **2021**, *403*.
39. Pekárek, S. Experimental study of surface dielectric barrier discharge in air and its ozone production. *Journal of Physics D: Applied Physics* **2012**, *45*.
40. Bednar, N.; Matović, J.; Stojanović, G. Properties of surface dielectric barrier discharge plasma generator for fabrication of nanomaterials. *Journal of Electrostatics* **2013**, *71*, 1068-1075.
41. Baroch, P.; Saito, N.; Takai, O. Special type of plasma dielectric barrier discharge reactor for

- direct ozonization of water and degradation of organic pollution. *Journal of Physics D: Applied Physics* **2008**, *41*.
42. Kovačević, V.V.; Dojčinović, B.P.; Jović, M.; Roglić, G.M.; Obradović, B.M.; Kuraica, M.M. Measurement of reactive species generated by dielectric barrier discharge in direct contact with water in different atmospheres. *Journal of Physics D: Applied Physics* **2017**, *50*.
43. Liu, W.; Ma, C.; Zhao, S.; Chen, X.; Wang, T.; Zhao, L.; Li, Z.; Niu, J.; Zhu, L.; Chai, M. Exploration to generate atmospheric pressure glow discharge plasma in air. *Plasma Science and Technology* **2018**, *20*.
44. Liu, W.; Niu, J.; Zhao, S.; Chai, M. Study on atmospheric pressure glow discharge based on ac-dc coupled electric field. *Journal of Applied Physics* **2018**, *123*.
45. Liu, W.-Z.; Zhao, S.; Chai, M.-L.; Niu, J.-Q. A method of using a carbon fiber spiral-contact electrode to achieve atmospheric pressure glow discharge in air. *Chinese Physics Letters* **2017**, *34*.
46. Ma, C.; Wang, L.; Nikiforov, A.; Onyshchenko, Y.; Cools, P.; Ostrikov, K.; De Geyter, N.; Morent, R. Atmospheric-pressure plasma assisted engineering of polymer surfaces: From high hydrophobicity to superhydrophilicity. *Applied Surface Science* **2020**.
47. Ouyang, J.-T.; Duan, X.-X.; Xu, S.-W.; He, F. The key factor for uniform and patterned glow dielectric barrier discharge. *Chinese Physics Letters* **2012**, *29*.
48. Massines, F.; Gherardi, N.; Naudé, N.; Ségur, P. Recent advances in the understanding of homogeneous dielectric barrier discharges. *The European Physical Journal Applied Physics* **2009**, *47*.
49. Akishev, Y.; Karalnik, V.; Medvedev, M.; Petryakov, A.; Shao, T.; Zhang, C.; Huang, B. About the possible source of seed electrons initiating the very first breakdown in a dbd operating with the air at atmospheric pressure. *Plasma Sources Science and Technology* **2021**, *30*.
50. Xue, Y.; Wu, B.; Jiang, L.; Guo, Y.; Huang, L.; Chen, J.; Tan, J.; Geng, D.; Luo, B.; Hu, W., *et al.* Low temperature growth of highly nitrogen-doped single crystal graphene arrays by chemical vapor deposition. *J Am Chem Soc* **2012**, *134*, 11060-11063.

51. Saito, N.; Bratescu, M.A.; Hashimi, K. Solution plasma: A new reaction field for nanomaterials synthesis. *Japanese Journal of Applied Physics* **2018**, *57*.
52. Hornbeck, J.A. Microsecond transient currents in the pulsed townsend discharge. *Physical Review* **1951**, *83*, 374-379.
53. Kim, H.-m.; Saito, N.; Kim, D.-w. Solution plasma-assisted green synthesis of mno<sub>2</sub> adsorbent and removal of cationic pollutant. *Journal of Chemistry* **2019**, *2019*, 1-7.
54. Lee, A.Y.; Yang, K.; Anh, N.D.; Park, C.; Lee, S.M.; Lee, T.G.; Jeong, M.S. Raman study of d\* band in graphene oxide and its correlation with reduction. *Applied Surface Science* **2021**, *536*.
55. Leon, V.; Quintana, M.; Herrero, M.A.; Fierro, J.L.; de la Hoz, A.; Prato, M.; Vazquez, E. Few-layer graphenes from ball-milling of graphite with melamine. *Chem Commun (Camb)* **2011**, *47*, 10936-10938.
56. Khai, T.V.; Kwak, D.S.; Kwon, Y.J.; Cho, H.Y.; Huan, T.N.; Chung, H.; Ham, H.; Lee, C.; Dan, N.V.; Tung, N.T., *et al.* Direct production of highly conductive graphene with a low oxygen content by a microwave-assisted solvothermal method. *Chemical Engineering Journal* **2013**, *232*, 346-355.
57. Fajardo-Diaz, J.L.; Lopez-Urias, F.; Munoz-Sandoval, E. Wrinkled nitrogen-doped carbon belts. *Sci Rep* **2018**, *8*, 3546.
58. Ning, G.; Xu, C.; Zhu, X.; Zhang, R.; Qian, W.; Wei, F.; Fan, Z.; Gao, J. Mgo-catalyzed growth of n-doped wrinkled carbon nanotubes. *Carbon* **2013**, *56*, 38-44.
59. Wu, Y.; Yu, D.; Feng, Y.; Han, L.; Liu, X.; Zhao, X.; Liu, X. Facilely synthesized n-doped graphene sheets and its ferromagnetic origin. *Chinese Chemical Letters* **2021**, *32*, 3841-3846.
60. Chae, S.; Phan, P.Q.; Panomsuwan, G.; Bratescu, M.A.; Hashimoto, T.; Teshima, K.; Saito, N. Single-walled carbon nanotubes wrapped by cationic nitrogen-doped carbon for electrocatalytic applications. *ACS Applied Nano Materials* **2020**, *3*, 10183-10189.
61. Li, O.L.; Prabakar, K.; Kaneko, A.; Park, H.; Ishizaki, T. Exploration of lewis basicity and oxygen reduction reaction activity in plasma-tailored nitrogen-doped carbon electrocatalysts. *Catalysis Today* **2019**, *337*, 102-109.



62. Liu, W.-W.; Chai, S.-P.; Mohamed, A.R.; Hashim, U. Synthesis and characterization of graphene and carbon nanotubes: A review on the past and recent developments. *Journal of Industrial and Engineering Chemistry* **2014**, *20*, 1171-1185.

# ***Chapter 6***

## ***Summary***

## *Chapter 6 - Summary*

In this thesis, the correlation between the process parameters of solution plasma and the structural parameters of final products, nitrogen-doped carbons, was explored using a multivariate analysis, aiming to improve the amount of nitrogen dopant and maintain the planar structure of carbon for energy application. Fifty-three organic solutions were selected as raw materials and categorized based on their reactivity. The solution plasma was conducted by the conventional electrode configuration, pin-to-pin. The process parameters included the active radicals, intermediates, and potentials, characterized by OES, GC/MS, and electrostatic probes, respectively. The obtained process parameters were analyzed to find the correlation with the structural parameters of nitrogen-doped carbons, characterized by XRD, Raman, and Elemental Analyzer. Then, the obtained correlation was further used to design the new electrode configuration of solution plasma. Finally, using the newly proposed solution plasma process, carbon products with nitrogen content up to 18.79 atom % were significantly higher compared to other conventional methods for synthesizing nitrogen-doped carbons for energy application. This thesis is organized into six chapters, as shown below, and a schematic diagram summarizing the studies in this thesis is shown in **Figure 6.1**.

In Chapter 1, the low nitrogen content of doped carbons synthesized by the conventional process is pointed out, which leads to the motivation of the research in this thesis, providing solution plasma process with a low temperature of reaction field to increase the nitrogen content of the carbon materials. Furthermore, the fundamental mechanism of carbon material formation in the solution plasma process from the viewpoint of the chemical reaction is introduced. In addition, the diagnostic methodology of the solution plasma process and carbon material characterization methods are described. Finally, the objective of exploring the correlation between critical process and structural parameters in the

synthesis of high nitrogen-containing carbons using solution plasma by multivariate analysis was proposed.

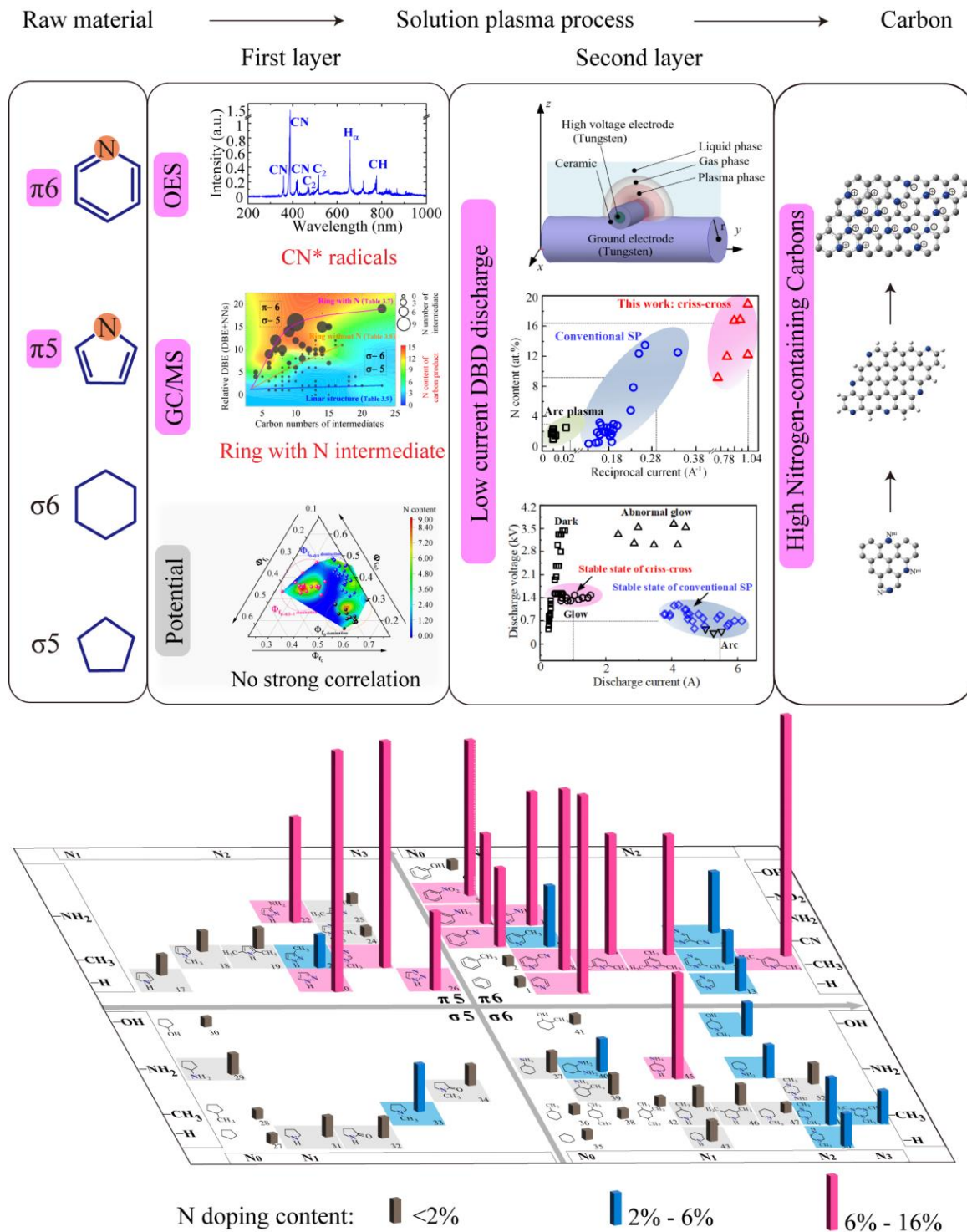
In Chapter 2, the correlation of raw materials, active chemical species in solution plasma, and nitrogen-containing carbon products were successfully discovered. The nitrogen-containing  $\pi$ -bonded organic molecules, including five- and six-member ring molecules, produced mainly  $CN^*$  radical species, which further produced high nitrogen-containing carbons.

In Chapter 3, the correlation of raw materials, intermediate species in solution plasma, and nitrogen-containing carbon products were successfully acquired. The nitrogen-containing  $\pi$ -bonded organic molecules, including five- and six-member ring molecules, produced  $\pi$ -bonded ring intermediates with a nitrogen atom in the aromatic framework, which can further produce high nitrogen-containing carbons.

In Chapter 4, the correlation between raw molecules and potential in solution plasma was successfully discovered. However, the correlation with further nitrogen-containing carbon products was not clearly found. It can mean that the potential did not play an important role in the structural parameters of final products.

In Chapter 5, the obtained correlation between the process parameters of solution plasma and the structural parameters of final products suggested that aromatic ring structural molecules should be used as a raw material. Moreover, it could also be used to suggest a new design of the solution plasma process, i.e., a criss-cross system, which can inhibit the energy mutations and further contribute to the nitrogen joint into the carbon framework by graphitic bonding configuration. Finally, the graphene products with up to 18 atom% of nitrogen-containing were successfully prepared.

Finally, the overall schematic diagram of the exploration result of this research was proposed. This pioneering systematic methodology is expected to guide the research on carbon synthesis by plasma technology for a wide range of applications, providing process design for chemists, materials scientists, and engineers who are dedicated to the research of carbon-based materials.



**Figure 6.1.** Schematic diagram of the exploration result of critical process about the solution plasma and structural parameters of the synthesized high nitrogen-containing carbons by multivariate analysis of the reaction field including OES, GC/MS, the potential of the first layer, and new proposed discharge geometry of the second layer.

---

# *Achievement*

## **List of publication**

### **[ Scientific papers related to doctoral thesis] (2 published and 1 submission)**

1. Jiangqi Niu, Chayanaphat Chokradjaroen and Nagahiro Saito, “Graphitic n-doped graphene via solution plasma with a single dielectric barrier”, *Carbon*, 2022, 199, 347–356.
2. Jiangqi Niu, Chayanaphat Chokradjaroen, Yasuyuki Sawada, Xiaoyang Wang and Nagahiro Saito, “Plasma–solution junction for the formation of carbon material”, *Coatings*, 2022, 12, 1607.
3. Jiangqi Niu, Chayanaphat Chokradjaroen and Nagahiro Saito, “Compositional dependence of radical domination in solution plasma forming carbon”, Under the submission to *Nature Communications*, 2022.

### **[Scientific papers not related to doctoral thesis] (1 published)**

1. Chayanaphat Chokradjaroen, Jiangqi Niu, J, Gasidit Panomsuwan and Nagahiro Saito, “Insight on solution plasma in aqueous solution and their application in modification of chitin and chitosan”, *Int. J. Mol. Sci.*, 2021, 22, 4308.

### **[Review paper] (1 published)**

1. Chayanaphat Chokradjaroen, Xiaoyang Wang, Jiangqi Niu, Tongxiang Fan and Nagahiro Saito, “Fundamentals of solution plasma for advanced materials synthesis”, *Materials Today Advances*, 2022, 14.

### **[Book] (1 accepted)**

1. Jiangqi Niu, Chayanaphat Chokradjaroen, Nagahiro Saito, “Solution plasma chemistry – Chapter 1 What are Solution Plasmas?”, Book, Under review from SPRINGER NATURE, 2022.

---

## List of presentation

### International Conference

1. Jiangqi Niu, Rinyarat Naraprawatphong, Chayanaphat Chokradjaroen, Xiaoyang Wang, Sangwoo Chae, and Nagahiro Saito, “Glow Plasma in Organic Solution by Criss-cross System”, INTERFINISH2020, September 7-9, 2020, online.
2. Jiangqi Niu, Chayanaphat Chokradjaroen and Nagahiro Saito, “Correlation of Excited Chemical Species by Solution Plasma in Cyclic Organic Compounds and the synthesized Carbon-based structure”, Plasma Processing and Technology International Conference 2022(Plasma Tech 2022), April 27-29, 2022, online.
3. Jiangqi Niu, Chayanaphat Chokradjaroen and Nagahiro Saito, “Electrical Properties of Plasma Formation in Organic Solution and the Structure of the Resulting Carbon Material”, 75th Annual Gaseous Electronics Conference 2022, Sendai International Center, Sendai, Japan, October 03-07, 2022

### Domestic conferences

1. Niu Jiangqi, Chokradjaroen Chayanaphat, 澤田 康之, 齋藤 永宏, “有機溶媒中で形成したプラズマの電気的特性と生成する炭素材料の構造”, 表面技術協会 第 145 回講演大会, 2022 年 3 月, オンライン.

## List of awards

1. Jiangqi Niu, Rinyarat Naraprawatphong, Chayanaphat Chokradjaroen, Xiaoyang Wang, Sangwoo Chae and Nagahiro Saito, Student Awards of INTERFINISH2020, online, September 7-9, 2020. Glow Plasma in Organic Solution by Criss-cross System.